NUMERICAL MODELLING OF A WAVE ENERGY CONVERTER BASED ON THE WAVE CLIMATE AROUND THE SAINT MARTIN′S ISLAND OF BANGLADESH

By
MOHUA DAS
Student ID: 1018122001

A thesis
Submitted to the
Department of Naval Architecture and Marine Engineering,
Bangladesh University of Engineering and Technology,
In partial fulfillment of the requirements
For the degree of
MASTER OF SCIENCE
In
Naval Architecture and Marine Engineering

May 2022

DEPARTMENT OF NAVAL ARCHITECTURE AND MARINE ENGINEERING

BANGLADESH UNIVERSITY OF ENGINEERING AND TECHNOLOGY

DHAKA – 1000, BANGLADESH

CERTIFICATE OF APPROVAL

The thesis titled **"NUMERICAL MODELLING OF A WAVE ENERGY CONVERTER BASED ON THE WAVE CLIMATE AROUND THE SAINT MARTIN'S ISLAND OF BANGLADESH"** submitted by Mohua Das, Student No. 1018122001, Session: October – 2018, has been accepted as satisfactory in partial fulfillment of the requirement for the degree of Master of Science in Naval Architecture and Marine Engineering on May 28, 2022.

BOARD OF EXAMINERS

Dr. Goutam Kumar Saha Professor Department of NAME, BUET, Dhaka	Chairman (Supervisor)
Dr. Md. Shahidul Islam Professor and Head Department of NAME, BUET, Dhaka	Member
Dr. Md. Mashud Karim Professor Department of NAME, BUET, Dhaka	Member
Dr. Md. Shahjada Tarafder Professor Department of NAME, BUET, Dhaka	Member
Dr. Md. Sadiqul Baree Professor Department of NAME, BSMRMU, Dhaka	Member (External)

CANDIDATE′S DECLARATION

It is hereby declared that this thesis or any part of it has not been submitted elsewhere for the award of any degree or diploma.

Mohua Das

Student ID: 1018122001

Dedicated

To

My Parents

ABSTRACT

Saint Martin′s Island is the only coral island and one of the well-known tourist spots in Bangladesh. Because of its geographic location, electricity cannot be supplied from the mainland through the electricity grid. Diesel generators and solar power are the only means of electricity generation presently available there. Surrounded by the sea, Saint Martin′s Island has the ideal conditions for wave energy extraction. The purpose of the study is to assess and optimize the performance of a heaving-point-absorber-wave-energy-converter in light of the existing wave climate around the island. The power generation performance of a cylindrical buoy shape has been tested for a variety of diameters and drafts. The mass properties of the selected design have been determined using simple structural analysis, and the hydrodynamic coefficients have been calculated through modelling and simulation in frequency-domain. Using the hydrodynamic coefficients data obtained from frequency-domain analysis, the response as well as power output of the system have been estimated using time-domain analysis with linear power take-off system. Comparing the power performance of different draft-diameter combinations of cylindrical buoy, the best design with maximum power output per unit buoy weight have been selected. Moreover, two other buoy shapes are tested, the values of surface area and volume obtained from optimal cylindrical configurations are used to generate new buoy profiles. Finally, comparing the results of power performance simulations, a discussion on the behaviors of different buoy shapes in different months have been presented and most suitable buoy shape for the intended energy deployment site have been proposed. Moreover, the key areas that requires further investigation have been identified and discussed.

ACKNOWLEDGEMENT

By the grace of the Almighty God, the thesis titled "Numerical Modelling of a Wave Energy Converter based on the Wave Climate around the Saint Martin′s Island of Bangladesh" has been done and the report has been completed. I would like to convey my earnest gratitude to several extra-ordinary people without whom this study would have not been possible.

I would like to express sincere respect and heart-felt gratitude to my thesis supervisor Dr. Goutam Kumar Saha, Professor, Department of Naval Architecture and Marine Engineering (NAME), Bangladesh University of Engineering and Technology (BUET), for his whole-hearted supervision. His clear guidance, timely instructions, invaluable advice, and encouragements throughout the progress of the thesis and report writing have made this thesis possible.

I would like to convey my sincere gratitude to Dr. Mohammad Rafiqul Islam, Vice-Chancellor, Islamic University of Technology (IUT), for his continuous interest, encouragement, whole-hearted support, constructive criticism, and assessment of the study. It was a great privilege to work under his guidance and I am very thankful for the valuable time he gave me despite his very busy schedule.

I would also like to acknowledge the kind assistance, prudent suggestions, sheer encouragements, valuable time, and whole-hearted support of Dr. Mohammed Abdul Hannan, Assistant Professor, Newcastle University, UK (Singapore Unit), to carry out the research work. I am really indebted to him for the important resources he kindly provided.

I would like to convey my heartfelt thanks to Dr. Md. Mashud Karim, Dr. Md. Shahjada Tarafder, Dr. Md. Shahidul Islam, and external member Dr. Md. Sadiqul Baree for their constructive remarks and kind evaluations of this study.

I would like to express thanks and appreciations to all of my well-wishers who inspired me to continue this work. I want to convey my appreciations to all of those who have supported him in any respect during the study.

I greatly acknowledge the support of the Department of Naval Architecture and Marine Engineering (NAME), Bangladesh University of Engineering and Technology (BUET) for carrying out the research work.

TABLE OF CONTENTS

LIST OF TABLES

LIST OF FIGURES

NOMENCLATURE & ABBREVIATIONS

H_{sig}	Significant wave height
T_e	Wave energy period
L	Wavelength
h	Water depth
g	Acceleration due to gravity
ρ	Density of seawater
P_W	Wave power density per meter of wave front
C_V	Coefficient of variation of wave energy
φ	Velocity potential function
η	Free surface elevation from mean water line
H	Wave height
a	Wave amplitude
c	Phase velocity of wave
ω	Angular velocity
F_{hs}	Hydrostatic force
F_e	Excitation force
F_r	Radiation force
$\hat{\varphi}$	Complex amplitude
β	Angle between the wave propagation direction and x-axis
$\hat{\varphi}_i$	Complex amplitude of incident-velocity potential
$\hat{\varphi}_r$	Complex amplitude of radiated-velocity potential
$\hat{\varphi}_s$	Complex amplitude of scattered-velocity potential
$\widehat{\xi_J}$	Complex amplitude of displacement in degree of freedom j
$\widehat{F_{hd}}$	Time-independent part of hydrodynamic force
$\widehat{F_{FK}}$	Frequency-dependent Froude-Krylov force

A	Added mass coefficient
B	Damping coefficient
k_m	Mooring spring stiffness
$\widehat{\boldsymbol{f}_e}$	Vector of complex amplitudes of excitation load for unit wave amplitude.
$u_{rel}(\omega)$	Relative velocity between the body and damper
$F_v(t)$	Viscous damping force
A_{ij}^{∞}	Added mass matrix at infinite frequency
K_{ij} (t)	Radiation impulse response function (RIRF)
f_{exc} (t)	Impulse response function (IRF)
D	Buoy diameter
T	Buoy draft
H_b	Buoy height
S	The length of the suspended mooring lines
X	Horizontal distance between the fairlead and the touchdown point of the mooring line on the seabed
v	Weight of the suspended chain
b	Catenary shape parameter
y	Vertical distance of the nodes of catenary line from the seabed

Abbreviations

JONSWAP	Joint North Sea Wave Observation Project
MVI	Monthly Variability Index
SVI	Seasonal Variability Index
WECs	Wave Energy Converters
WEC-Sim	Wave Energy Converter Simulation
BEMIO	Boundary Element Method Input Output
RM3	Reference Model 3

CHAPTER 1

INTRODUCTION

1.1 Background and Present State of the Problem

Ocean waves are one of the highly available renewable energy resources that contain 15 to 20 times more energy per square meter in comparison with wind or solar power (Islam et al., 2014). Waves are generated by energy transfer from the wind to the water. However, depending on the wind speed, fetch length, and wind duration, the wave characteristics can vary. The power requirements of any country in the world can be partially fulfilled by utilizing its wave energy resources as a large amount of energy can be extracted from waves. The device that extracts potential energies of waves and converts it to useful mechanical or electrical energy is termed as 'wave energy converters (WECs)'.

The concept of energy harnessing from ocean waves using WECs has been recognized for at least 200 years (Folley, 2016). The first patent of WECs was submitted in 1799, and currently, several hundreds of patents have been in existence to capture wave energy (Aderinto and Li, 2018). According to Charlier and Justus (1993), wave extraction systems utilize one of three basic ways to capture wave energy-

1. the vertical rise and fall of successive waves to develop wave- or air- pressure to operate turbine,
2. different motions of a floating body caused by waves and convert it through various means to electricity generation, and
3. concentrating the incoming waves through a converging channel to build up pressure and thus, run air turbine.

Based on the different ways in which the energy is exploited, currently, several wave energy conversion technologies are available; however, they aren't mature enough to be developed in industrial and commercial scale (Esteban et al., 2017). To ensure consistent operation of WECs in unpredictable, random sea states as well as in hostile salt environment is far more difficult than land-based renewable energy technologies. Besides, initial cost of construction of WECs is significantly higher. Although the opportunity of energy production from ocean waves is enticing, these constraints impose challenges to the optimum design and industrialization of WECs.

Therefore, the main concern related to energy harnessing from waves is to ensure balance between the amount of energy produced and the cost of energy conversion. Numerous theoretical, computational, and experimental studies were conducted in many countries to model Wave Energy Converters (WECs) behavior most cost-effectively. Different techniques are reported in the literature to optimize geometry and control systems for existing wave energy converters as well as new designs.

As mentioned earlier, one of the energy capture technologies from ocean waves is to utilize wave-caused motion of the floating bodies (i.e., translational motion: heave, surge, sway, and rotational motion: pitch, roll, yaw) to produce electricity. Within this category, the most efficient and robust one is the point absorbing wave energy converter. It mostly uses vertical translational motion for its actuation mechanisms. It is the most advantageous one as it is simple and light as well as can capture energy from all directions of ocean waves. In addition, it can absorb energy from the low oscillatory motions of waves. The general design of a point absorber WEC is depicted in Figure 1.1. As shown in Fig. 1.1, the simple point absorber consists of a floating buoy (also known as captor, which captures wave energy) and power take-off (PTO) system. PTO system can be defined as the mechanism that converts absorbed energy by primary converters into usable electricity. Each component of the system is equally crucial to consider during the design stage to maximize the power capture capacity of point absorber. Several research activities have been carried out to propose optimal shape, dimensions of the buoy as well as efficient PTO mechanism.

Pastor and Liu (2014) analyzed the effects of different design parameters such as shape, diameter, and draft of the buoy on the behavior of the heaving point absorber. To determine the power output of hemispherical as well as conical buoys, they performed numerical modelling, and simulation in both frequency- and time-domain. Comparing the hydrodynamic diffraction results, they concluded that the performance of conical buoy is slightly better than hemispherical buoy. In addition, they found that buoy draft had negligible impact on the power production at lower sea states; however, at higher sea states, smaller draft buoy slightly outperforms than the larger ones. Besides, changing buoy diameter showed significant impact on power production; with the increment of the buoy diameter, absorbed power by the buoy also increased.

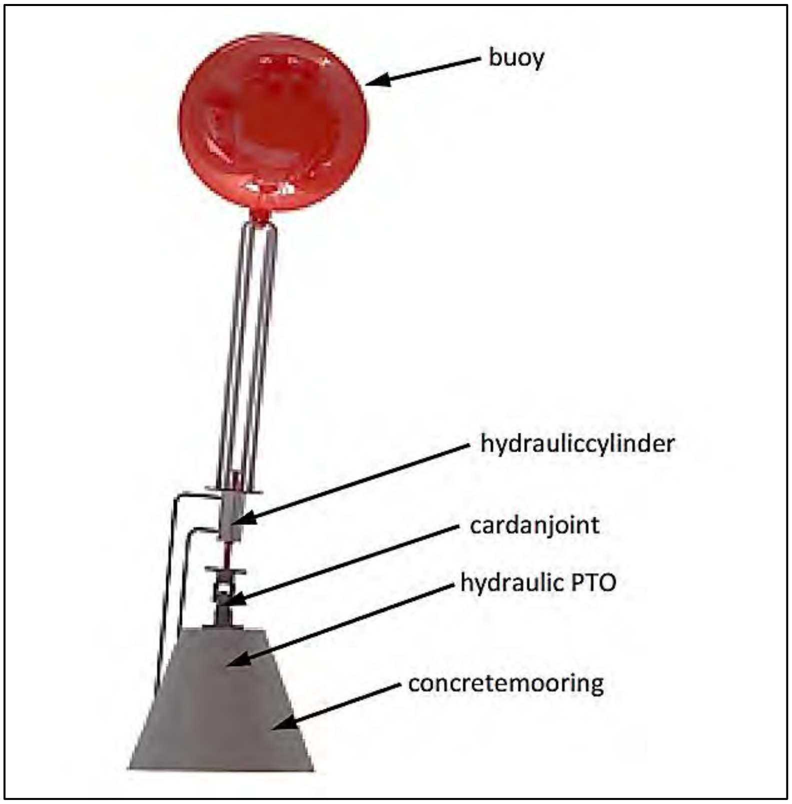

Figure 1.1 Point absorber WEC (source: Beirao and dos Santos Pereira Malça, 2014)

Shadman et al. (2017) outlined a methodology to optimize the geometry of a floating cylindrical buoy using statistical analysis method. To determine hydrodynamics of the system, they utilized frequency-domain boundary element method solver Ansys-AQWA. Design of Experiment (DOE) method was performed using Minitab software to determine the optimized geometry. Considering the predominant waves of the intended energy deployment site, they proposed optimized geometry of the buoy in terms of draft and diameter, which could absorb maximum energy over the most extensive range of frequencies.

Riley (2018) tested four different shapes (cylindrical, hemispherical, conical, pinched cone) of axisymmetrical buoys to determine the importance of buoy shape selection on power output. The response of each buoy was tested using 'AQWA Hydrodynamic Response Solver'. The results concluded that under regular wave conditions, compared to the cylindrical buoy, there was an increase in the peak power capture (in between 12% and 17%) when modified buoy shapes were used. However, the hypothesis wasn't supported when response analysis of the buoys was conducted using irregular waves.

Beirao and dos Santos Pereira Malça (2014) performed finite element analysis to analyze the structural behavior of different buoy shapes (spherical, cylindrical, and tulip) under different wave loading conditions. From their study, it was found that spherical buoys presented the lower values of stress concentration, induced the lowest displacements, and thus, displayed the best WEC structural behavior under the action of regular waves.

Many researchers, e.g., Ricci et al. (2008), Andrés et al. (2013), Li and Yu (2012), etc., have conducted time-domain modelling and analysis of the point absorbers including non-linear effects to produce more realistic behavior of WECs. Yu et al. (2014) conducted research on oscillating wave energy converters that mainly convert surge motion of the structure to usable electricity (Fig. 1.2). The simulations of the WECs were executed using 'wave energy converter simulator (WEC-Sim)′ - a time-domain numerical modelling tool. Different design parameters of the converter as well as different mooring configurations were considered for performing structural analysis and calculating power performance. They carried out more realistic assessment of optimum design by incorporating economic constraints and environmental issues.

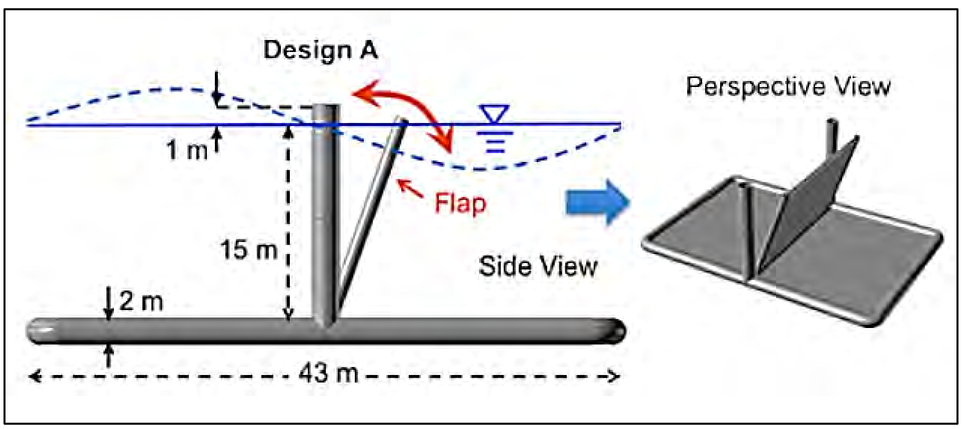

Figure 1.2 Oscillating Surge Wave Energy Converter (OSWEC) (source: Yu et al., 2014)

Besides, instead of manual parametric study, different evolutionary optimization algorithms such as swarm intelligence methods, genetic algorithms, etc., are reported in the literature to optimize WECs performance (Sergiienko et al., 2020, Blanco et al., 2021). Moreover, numerous research works have been performed to increase efficiency of other wave energy conversion technologies such as, electricity production using the vertical rise and fall of successive waves (e.g., oscillating water column), capturing waves in a reservoir to create pressure head (e.g., overtopping devices).

An extensive description of these conversion technologies can be found in 'Ocean wave energy: current status and future perspectives' by Cruz (2007).

To design a suitable WEC for any energy harnessing site, it is necessary to analyze the wave climate characteristics of that site accurately. As numerical modelling of WECs considering regular monochromatic waves can end up inaccurate predictions of WEC's power generation performance, thus, precise information regarding wave characteristics such as, wave heights, wave energy periods, wavelengths, and wave directions are essential in designing appropriate WEC.

As a result, several research activities have been performed in many countries of the world to assess wave power potential of different energy deployment site. Some of these studies have been conducted using different data sources. These sources include the European Centre for Medium-Range Weather Forecasts (ECMWF) Re-Analysis (ERA)-Interim wavefield data (1979–2014) (Espindola and Araújo, 2017; Kumar and Anoop, 2015; Wan et al., 2017), ERA-40 wave reanalysis data (1957–2002) (Zheng et al., 2014), Radar Altimeter Database System (Yaakob et al., 2016), AVISO multisatellite altimeter dataset (Wan et al., 2015), and hindcast data from the SIMAR-44 dataset (Iglesias and Carballo, 2010). Moreover, researchers, including Aboobacker et al. (2017), Bouhrim and El Marjani (2019), Hughes and Heap (2010), Zheng et al. (2013), Akpınar and Kömürcü (2013), Monteforte et al. (2015) have used different numerical models, such as the third-generation wave model WAVEWATCH III, third-generation wave prediction model WAM and Simulating Waves Nearshore (SWAN) model to simulate nearshore wave energy propagation. Furthermore, in situ measured wave data based on buoy measurements were used for energy assessment (Kumar et al., 2013).

From all of these findings, different locations have been categorized into wave energy-rich, sub-rich, available, and indigent areas based on the values of the wave power density. For example, if the wave power density is greater than 2 kW/m, then the wave power resources are considered available; if the wave power density is greater than 20 kW/m, then the wave power resources are considered rich (Wan et al., 2015; Zheng et al., 2012; Zheng et al., 2013; Zheng et al., 2014). Moreover, to select suitable energy conversion techniques from the existing ones and the design of new energy converters, some factors have been identified. These include the characteristics of wave climate, annual storage of wave energy, monthly and seasonal variations of wave power density, and coefficients of variation *(C_V)* of wave power data. For instance, Zheng et al. (2013) regarded significant wave height values greater than 0.5 m as exploitable based on the performance of several excellent wave power devices. Zheng et al. (2014) defined significant wave height values greater than 0.8 m as the effective significant wave height to assess the suitability of different regions for wave energy resource development. Furthermore, Wan et al. (2015) reported that the characteristics of wave climate with significant wave height ranging from 0.5 to 4.0 m and wave energy period ranging from 4–10 s are advantageous for energy conversion techniques. Moreover, Monteiro et al. (2017) reported that, for stable resources, the C_V of wave power data should be less than 0.8.

In Bangladesh, the contribution of existing renewable energy resources (i.e., biogas, hydropower, solar, and wind) is less than 2% of the total power generation (Islam and Khan, 2017). Government of Bangladesh has undertaken a 5-year plan to generate 5% to 10% total power from renewable energy sources (Islam and Khan, 2017). Thus, the proper utilization of wave power needs to conform to the plan of the Bangladesh government and help lessen the energy crisis. Furthermore, Bangladesh is blessed with the world′s longest natural sea beach and many islands surrounded by the Bay of Bengal. If the waves of the Bay of Bengal are properly utilized to produce electricity, then it can not only fulfill the total electricity demand to some extent but also enable access to electricity by the remote areas of the country. Thus far, only a few studies have been conducted to assess and extract the wave energy of the Bay of Bengal.

Islam et al. (2014) conducted a study of the waves generated in the Bay of Bengal at Cox′s Bazar, Chittagong, Bangladesh and proposed a new experimental design methodology of the wave energy conversion system. In their study, they calculated wave power density using NRT-merged data. Finally, they concluded that a large amount of power could be generated from April to October and a moderate amount for the rest of the year.

Rahman et al. (2018) developed a model of the coastal region near Cox′s Bazar, Chittagong, Bangladesh using the Delft3D simulation software. The output of their simulated model showed that a large amount of wave energy could be extracted from April to October.

Moreover, given the geographic locations of the islands of Bangladesh, supplying electricity from the primary electricity grid is expensive and difficult. Therefore, the generation of power using wave energy will help meet the power demand of the island communities. Of the islands in Bangladesh, Saint Martin′s Island is the most suitable one for energy extraction operations because of its favorable geographic location and moderate sea state value.

Hossain et al. (2019) carried out research to analyze the potential of wave energy extraction in different locations of Bangladesh. In their work, Pierson–Moskowitz spectrum was used to define the irregular sea states of the Bay of Bengal. Based on the research findings, they concluded that Cox′s Bazar, Saint Martin′s Island, and Sandwip wave power plants had great simulation results and thus, have a lot of possibilities to produce electricity.

Given the feasibility of wave energy exploitation projects, research to identify abundant wave energy resources and stable wave power regions around the Saint Martin′s Island needs to be conducted. Moreover, actual energy spectrum should be generated to predict accurate electricity production from the waves.

The first analysis of wave energy resources around Saint Martin′s Island was conducted by Das et al. (2018). They investigated available wave energy per meter wavefront in one location (longitude, 92.317°; latitude, 20.6°) near Saint Martin′s Island in Bangladesh from April 2016 to July 2016. In their study, they mainly concentrated on only one location at shallow water depth. However, the available wave power during peak season for tourists (October–February), variations of wave characteristics and wave power with the increase in water depths, selection of energy-rich regions, and assessment of stability for the safe operation of wave energy converters (WECs) have not been assessed in their study.

Afterwards, Das et al. (2021) thoroughly analyzed the characteristics of wave climate at varying water depths around the Saint Martin′s Island through flow and wave simulation modeling of the year 2016. They reported that the wave characteristics around the island fulfill the criterion of exploitable wave energy. Also, the resources are sufficiently stable and the potential of wave energy resources around the island is promising. Thus, modeling and optimization of a suitable energy conversion device for energy harnessing around Saint Martin′s Island is still an open area of research and thereby yields the scope of the proposed thesis.

1.2 Motivation

Research on wave energy exploitation has been motivated by abundant as well as stable wave energy resources around the Saint Martin′s Island of Bangladesh. The design of a suitable and cost-effective WEC would not only contribute to meeting local energy demand but also help to meet the target of the Bangladesh government to generate more than 4,100 megawatts of electricity from renewable energy sources by 2030.

1.3 Objective of the Research

This research aims to design a suitable energy conversion device based on the existing wave climate around Saint Martin′s Island so that efficient energy conversion from all existing sea states is possible. The primary objective of the present research can be subdivided into specific tasks. This study-

i. selects a suitable wave energy conversion technology in light of the existing wave climate around the Saint Martin′s Island of Bangladesh.

ii. predicts response of the selected Wave Energy Conversion (WEC) system. Time-domain numerical modeling and simulation will be employed to evaluate such responses for the intended energy harnessing site.

iii. proposes a suitable mooring system for ensuring the effective and unrestrained operation of the selected device in both normal and extreme wave conditions.

iv. examines the effect of different design parameters, e.g., geometrical shape, submerged volume, power take-off (PTO) coefficients, etc., on the proposed device′s power performance. These observed effects will then be employed for selecting the optimum design parameters to ensure maximum energy capture from all existing sea conditions of the energy extraction site.

1.4 Methodology

The stepwise methodology has been illustrated in Figure 1.1.

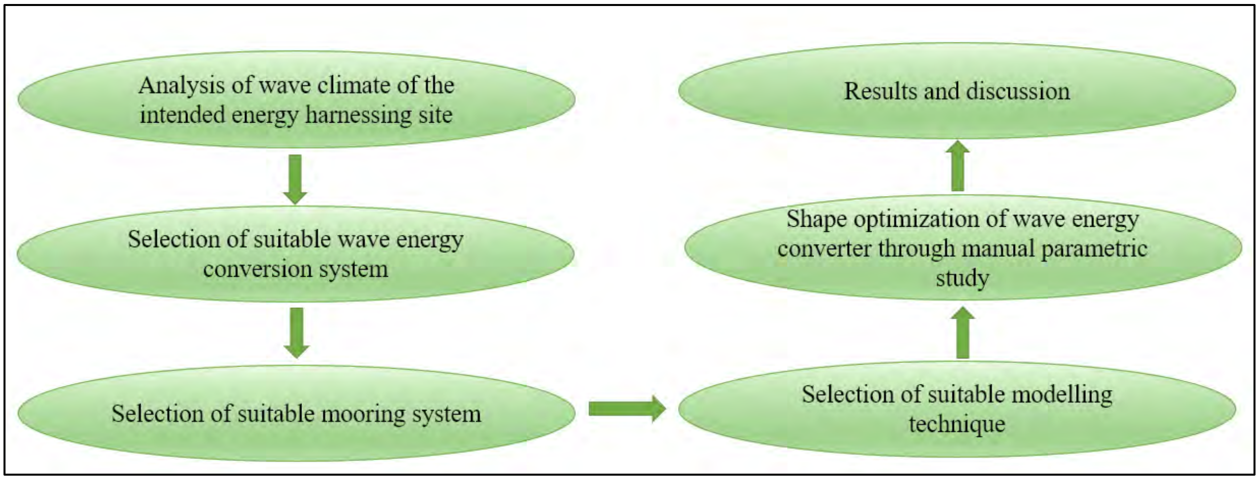

Figure 1.1 A flowchart of methodology

These steps are illustrated in detail in the following chapters.

1.5 Organization of the Thesis Report

The rest of the thesis paper is organized as follows.

Chapter 2 represents a detail analysis of the wave climate of the intended energy harnessing site around the Saint Martin's Island using 4-years simulation results obtained from flow and wave simulation modelling through Delft3D.

Chapter 3 presents brief discussion on existing wave energy conversion devices and their suitability in different water depths. In Chapter 3, we select the best design considering wave climate and water depth of our location of interest.

In Chapter 4, we review different mooring configuration and choose suitable mooring system to ensure efficient operation of the device under normal sea as well as extreme sea conditions.

Chapter 5 provides brief descriptions of the currently available modelling techniques to obtain response as well as power output of the wave energy converters. In Chapter 5, considering available resources, we select a suitable modelling technique to determine the power performance of our selected energy conversion system.

Chapter 6 delineates the procedure follows to optimize the geometry of the selected energy conversion system.

Chapter 7 discusses the results obtained through the numerical modelling and simulation.

Chapter 8 provides conclusions and suggestions for future work.

CHAPTER 2

WAVE CHARACTERISTICS ANALYSIS

To precisely describe the wave climate of a given location, three main wave parameters are required- significant wave height (H_s), wave energy period (T_e), and wavelength (L). Besides, to accurately evaluate the effects of different directions of wave propagations on the performance of WECs, information of mean wave direction (θ) is also needed. In this study, characteristics of wave climate in a nearshore area close to the Saint Martin′s Island have been analyzed based on the results of four years of simulations. Specifications of the target area are as follows-

- Geographic coordinates: (Longitude- 92.317^{0}N, Latitude- 20.566^{0}E)
- Water depth: 7.1 m
- Distance from the island: (< 1 km)

The simulations have been conducted using the verified coupled flow–wave numerical model from January 1, 2014, to December 31, 2017. A 1-hour interval is set to store the computed quantities of the observed locations. Descriptions of the variables (i.e., significant wave height, wave energy period, wavelength, and mean wave direction) obtained from simulation results are given in the following subsections.

2.1 Analysis of the Significant Wave Height Characteristics

Considering the safe and sound operation of WECs, waves with heights between 0.5 m and 4.0 m are considered useful for the extraction of wave energy flux (Wan et al., 2015). Figure 2.1 illustrates the wave height histogram for the location of interest close to the Saint Martin′s Island plotted based on 34,460 significant wave height data recorded from simulated coupled flow–wave models for the aforementioned time period i.e., January 1, 2014, to December 31, 2017. The frequency of a specific range of waves is denoted by the area under the bar. The maximum number of waves of 13,695 (i.e., ~39.75% of all occurrences) with significant wave height within the range of 1.0–1.5 m is recorded. Only 24 waves (0.07%) within the height range of 3.0 to 3.5 m are recorded. The frequency of significant wave height having a value greater than or equal to 0.5 m is estimated to be 92.25%.

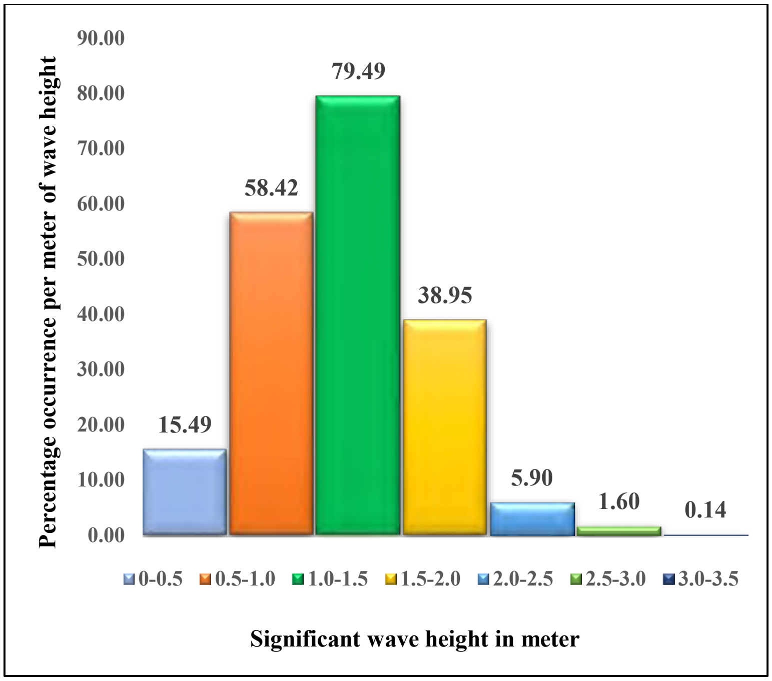

Figure 2.1 Wave height histogram

2.2 Analysis of the Characteristics of Wave Energy Period

From the simulation output, 34,460 data of peak wave period at 1-h intervals for the year 2016 are stored of the same location. Wave energy period has been calculated considering 90% of the peak wave period because of the selection of the JONSWAP-type (Joint North Sea Wave Observation Project) spectrum from the spectral space input parameters (Cornett, 2008). Notably, in coupled wave-flow modelling, three different spectra, i.e., JONSWAP, Pierson-Moskowitz (PM), and Gaussian-shape frequency spectrum, were available in Delft3D wave model. Trials had been made by changing input spectrum type, and the best results were obtained for the JONSWAP spectrum.

Wan et al. (2015) reported that wave energy periods within the range of 4 to 10 s are convenient for the energy extraction. Thus, in this study, we attempt to determine the percentage of wave energy periods with a value greater than or equal to 4 s. Therefore, the histogram of the wave energy periods has been generated based on the calculated wave period data. Figure 2.2 illustrates the histogram of the wave energy periods. As shown in the figure, the maximum number of waves (i.e., 36.76% of all occurrences) with the value of wave energy period within the range of 4.0–5.0 s has been recorded. Besides, the percentage of occurrences of wave energy periods greater than or equal to 4 s are estimated to be 80.7%.

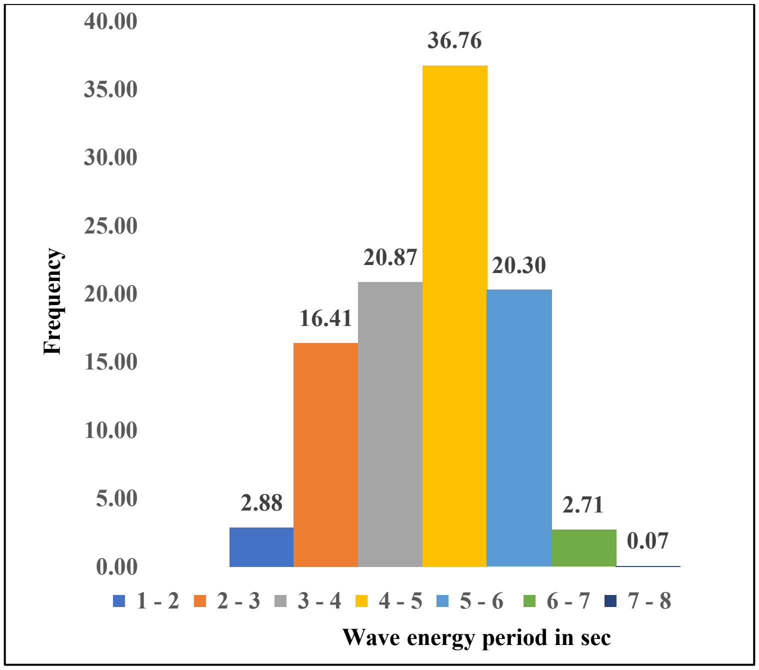

Figure 2.2 Histogram of wave energy period

2.3 Analysis of Wavelength Characteristics

The wavelength data of the observed location obtained from the simulation of the coupled flow–wave models are presented in Fig. 2.3. The highest hourly average value of wavelength at the observed location is recorded in June (40 m).

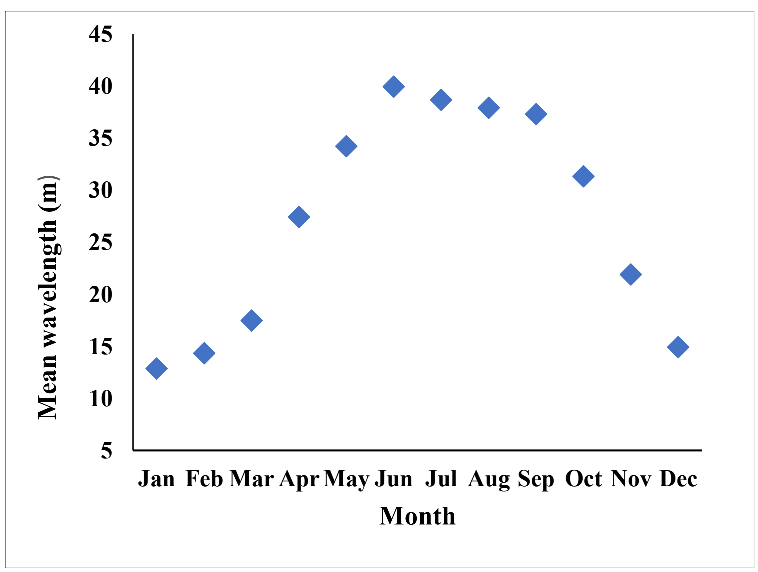

Figure 2.3 Average value of wavelengths of different months

2.4 Directional Distribution of Waves

The values of the wave direction in the intended energy deployment site are extracted from the results of coupled flow–wave simulations. As shown in Figure 2.4, the maximum number of waves (~45%) are predominantly observed between the WSW and WNW directions (247.5° to 292.5°), and the maximum value of significant wave height is 3.0 m. Moreover, 35% of the waves are observed between the SSE and SSW directions. Notably, in Figure 2.4, North (N) = 0^o, East (E) = 90^o, South (S) = 180^o, and West (W) = 270^o.

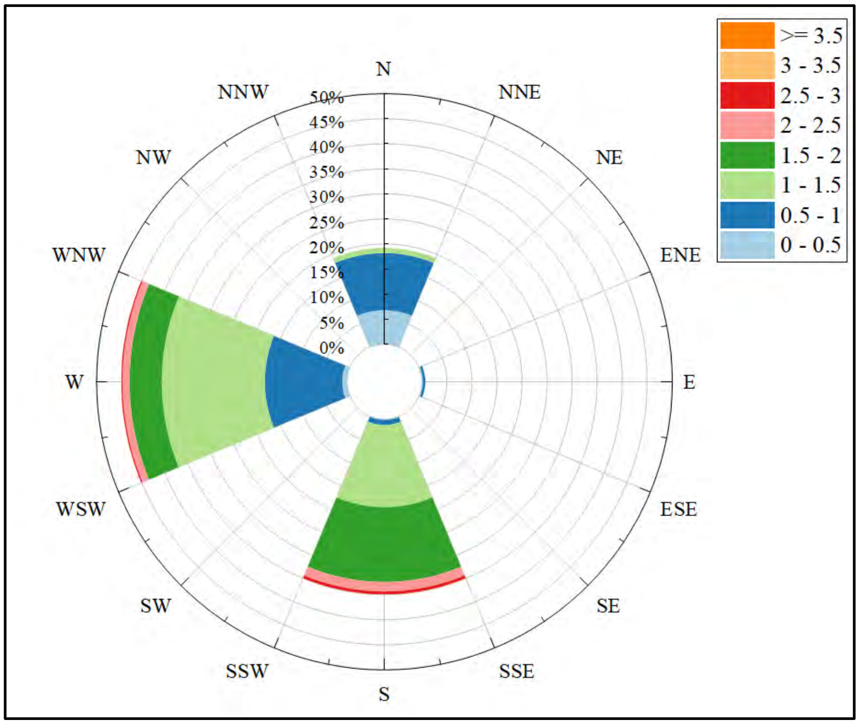

Figure 2.4 Wave rose diagram

2.5 Assessment of the Wave Power Density

From the results of coupled flow–wave simulations, the values of the wave parameters (i.e., significant wave height, wave energy period, wavelength, and wave direction) are obtained at a specified time interval (1 h). As the model does not provide the values of the wave power density directly, using the parameters stated previously, the wave power densities per meter wave front have been calculated using the following formula (Wan et al., 2015; Wan et al., 2018):

$$P_W = \bar{E} c_g$$
$$= \bar{E} \left[\frac{gT_e}{2\pi} tanh(kh)\right] P_*$$

where, $\bar{E}$ = wave energy density (J/m^2) = $\frac{\rho g H_{sig}^2}{8}$ (for regular waves)

= $\frac{\rho g H_{sig}^2}{16}$ (for random waves)

and $P_* = \frac{1}{2} \times \left(1 + \frac{2kh}{sinh(2kh)}\right)$

$$\therefore P_W = \frac{\rho g H_{sig}^2}{16} \times \frac{gT_e}{2\pi} tanh(kh) \times \frac{1}{2} \times \left(1 + \frac{2kh}{sinh(2kh)}\right)\left(\frac{kW}{m}\right) \quad (2.1)$$

where $k = \frac{2\pi}{L}$ is wave number (m^{-1}),

L is the wavelength,

H_{sig} is the significant wave height,

T_e is the wave energy period,

h is the water depth (m),

g is the acceleration due to gravity (m/s2), and

ρ is the density of seawater(kg/m3).

Figure 2.5 (a) presents the hourly mean wave power density. Additionally, Figure 2.5 (b) illustrates separately mean wave power density of different years. As shown in Figures, 2.5 (a) and 2.5 (b), moderate wave power densities are observed in the summer (i.e., March to June) and rainy monsoon (i.e., June to November) periods. In winter (i.e., December to February), the wave power densities are noticeably smaller. In these four years, the minimum value of wave power density per meter wavefront (P_W) is obtained in February 2017, which is 0.62 KW/m. Moreover, the maximum value of P_W is 10.40 KW/m, recorded in both July 2014 and June 2015. Notably, wave energy is considered available when $P_W \geq 2$ KW/m and considered rich when $P_W \geq 20$ KW/m (Zheng et al., 2013). Thus, the wave energy densities in the selected location fulfill the minimum criterion of exploitable wave energy ($P_W \geq 2$ kW/m). However, compared with global wave energy resources, the region of interest is not energy-rich. Nevertheless, the design of suitable and cost-effective WECs would enable the implementation of the extraction process, which is the main target of this research work.

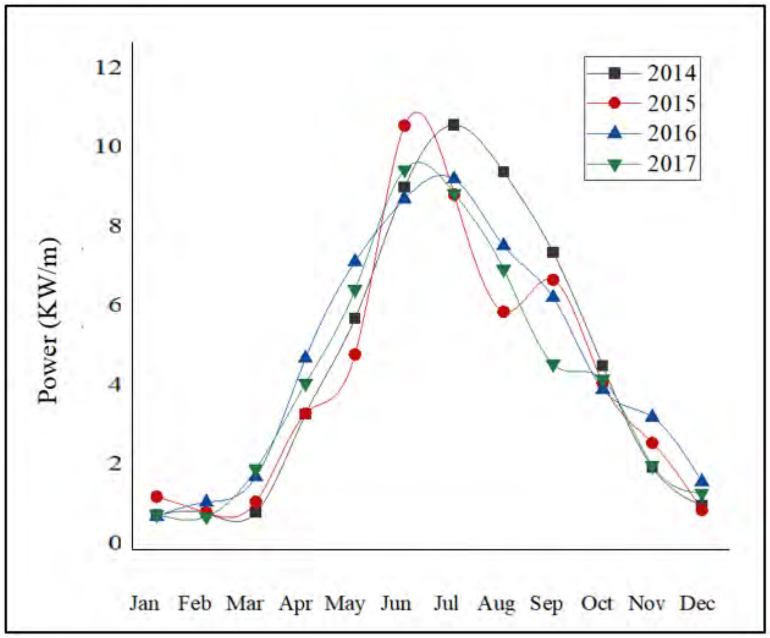

Figure 2.5(a) Variation of wave power densities of different years

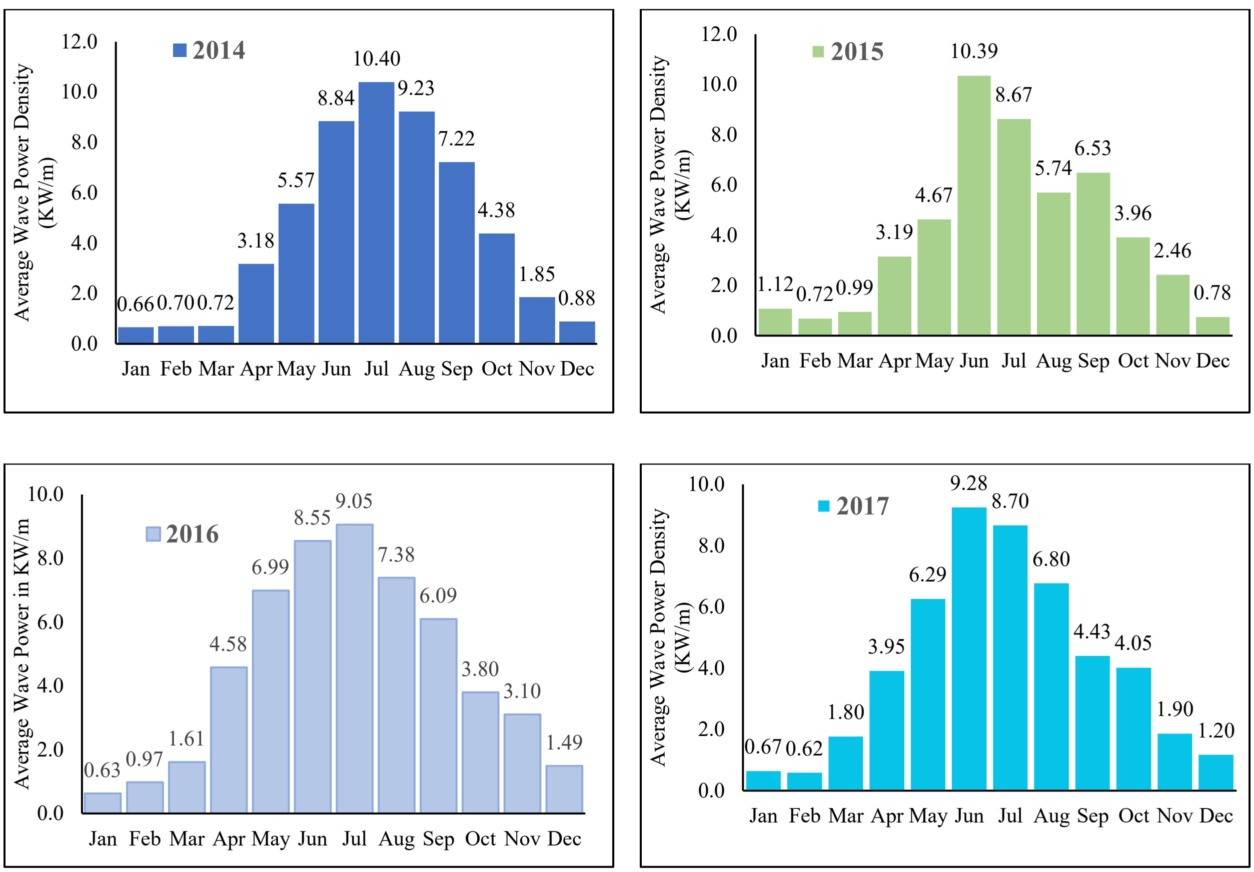

Figure 2.6(b) Average wave power density of different months of different years

2.6 Variability of Wave Power Density

To assess the suitability of wave energy conversion systems, the temporal variability of the wave power data of the study regions needs to be determined. Several indices, such as coefficient of variation (C_V) of wave energy and monthly and seasonal variabilities of wave power, are used to evaluate the variability of the wave power and assess the stability of wave energy resources. Monteiro et al. (2017) reported that, for stable resources, the C_V value should be less than 0.8 (i.e., smaller values signify more stable wave energy resources). Moreover, moderately unstable wave power resources have C_V values within 0.8–0.9. Furthermore, $C_V > 0.9$ indicates that the resources are unstable. The following formula estimates the C_V value of wave power (Wan et al., 2015):

$$C_V = \frac{\sqrt{\frac{\sum_{i=1}^{n}(P_i - P_{avg})^2}{n}}}{P_{avg}} \tag{2.2}$$

Table 2.1 presents the C_V values for different months. As shown in the Table 2.1, the wave energy resources satisfy the stability criterion (i.e., C_V <0.8) for the months April to November (except October 2017).

Table 2.1 Variations of C_V of the different months

Cv				
	2014	2015	2016	2017
Jan	0.62	0.89	**1.02**	0.67
Feb	0.86	0.74	0.61	**1.10**
Mar	0.75	0.87	0.54	**0.92**
Apr	0.42	0.47	0.48	0.53
May	0.23	0.39	0.85	0.27
Jun	0.61	0.64	0.46	0.58
Jul	0.47	0.42	0.45	0.51
Aug	0.41	0.37	0.43	0.28
Sep	0.34	0.47	0.44	0.32
Oct	0.59	0.58	0.28	0.89
Nov	0.77	0.53	0.62	0.57
Dec	0.64	0.90	**0.95**	0.80

The monthly variability index (MVI) and seasonal variability index (SVI) can be defined as follows (Wan et al., 2015; Bouhrim and El Marjani, 2019):

$$MVI = \frac{P_{Mmax} - P_{Mmin}}{P_{year}} \tag{2.3}$$

$$SVI = \frac{P_{Smax} - P_{Smin}}{P_{year}} \tag{2.4}$$

where P_{Mmax} and P_{Mmin} denote the values of the mean wave power density of the most and least energetic months, respectively. Similarly, P_{Smax} and P_{Smin} denote the maximum and minimum values of the seasonal mean wave energy density, respectively, and P_{year} denotes the annual mean wave power.

The values of the monthly and seasonal variability indices are presented in Table 2.2. The values of the MV index indicate that the range of variation of the mean wave power densities for different months is close to twice that of the corresponding annual mean wave power densities. Therefore, the monthly variation of wave power is significant and indicates the moderately fluctuating values of the wave power density in the observed location. Moreover, the SV index values are significantly lower than the MV index values. Small values of SVI indicate an insignificant seasonal variation of wave power densities in relation to the annual mean wave power density.

Table 2.2 Monthly and seasonal variability indices of wave power

Year	**MVI**	**SVI**
2014	2.18	1.05
2015	2.36	1.21
2016	1.86	1.11
2017	2.09	1.18

2.7 Characterization of Wave Climate and Development of Wave Energy Spectrum

Using the value of wave power density, the percentage contribution of different sea states (defined by significant wave height and wave energy period) to the total wave power density are also determined. These will provide a reference for the design and evaluation of the performance of different WECs. According to Table 2.3, sea states with the range of significant wave heights between 1.0 m and 2.5 m and wave energy periods with the interval of 4.0 to 6.0 sec have the most significant contribution (~78%) to the total wave power density. Moreover, significant wave heights greater than 3.0 m and less than 1.0 m do not contribute much to the total wave power density. Notably, there is a dominance of significant wave height and peak wave period within the range of 1.0-1.5 m and 4.0-5.0 sec, respectively, contributing ~25% of total power.

Afterward, an average wave energy spectrum is developed based on the relevant wave climate data, which will be used as an input parameter during the performance evaluation of WEC. The wave energy spectrum is illustrated in Figure 2.6. The area under the bar denotes the total energy density obtained from the specified frequency range from the year 2014 to 2017. According to Figure 2.6, the peak frequency of the energy spectrum is found to be 0.213 Hz (4.7 sec). A large amount of energy is obtained from the frequency between 0.163 Hz to 0.262 Hz (3.82 sec to 6.13 sec).

Table 2.3 Characterization of wave energy resources in terms of significant wave height and wave energy period

H_{sig} (m)								
3.0-3.5							0.57	
2.5-3.0						1.74	2.81	
2.0-2.5					<1	8.41	1.33	<1
1.5-2.0				<1	13.16	20.77	4.5	<1
1.0-1.5				3.73	24.9	9.8	<1	<1
0.5-1.0		<1	1.47	4.16	1.45	<1	<1	<1
0-0.5		<1	<1	<1				
	0-1.0	1.0-2.0	2.0-3.0	3.0-4.0	4.0-5.0	5.0-6.0	6.0-7.0	7.0-8.0
				T_e (sec)				

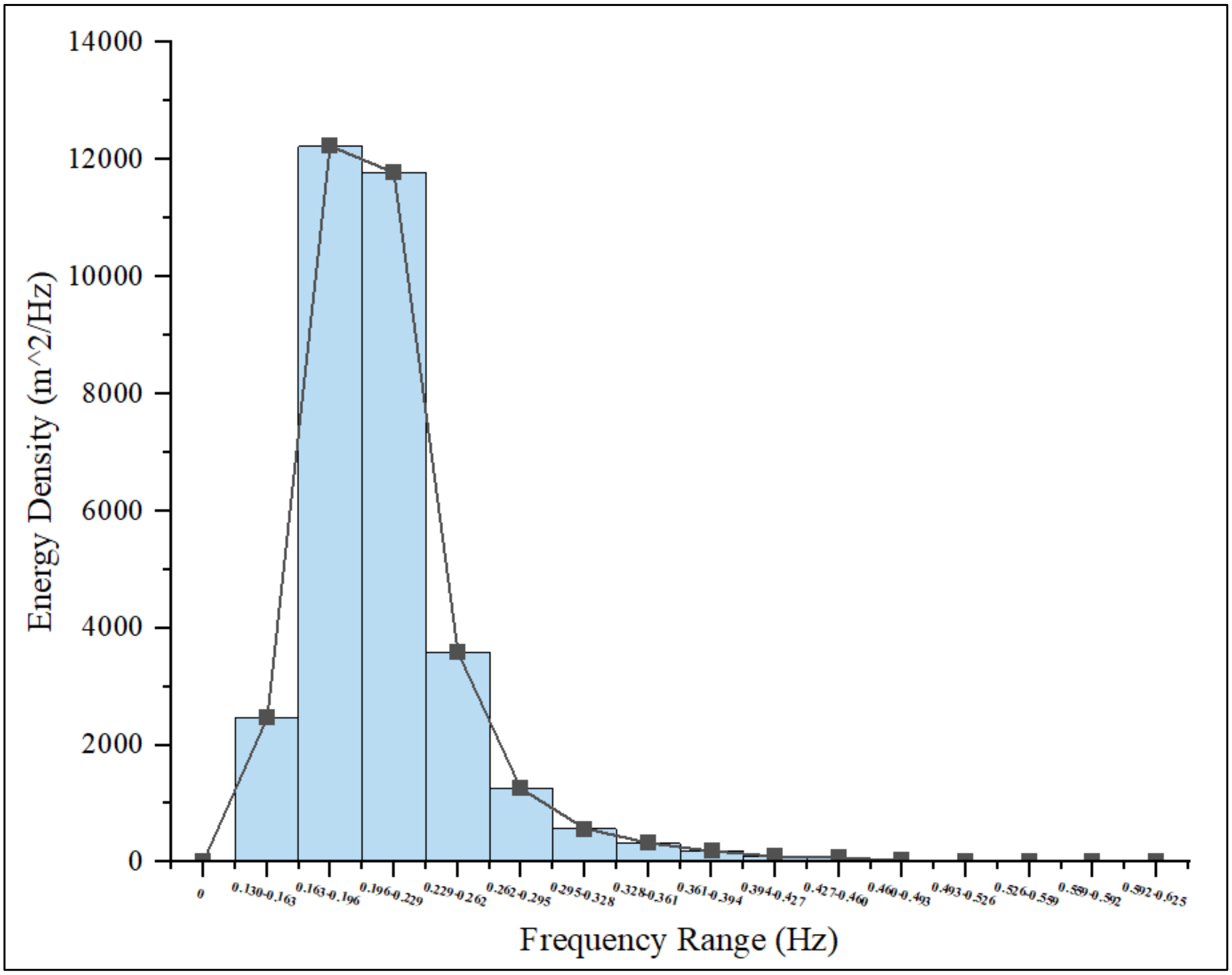

Figure 2.6 Wave energy spectrum

CHAPTER 3

SELECTION OF SUITABLE WAVE ENERGY CONVERSION TECHNIQUE

Ocean waves have enormous potential to supply a substantial amount of clean energy. Thus, proper utilization of wave energy resources to produce electricity contributes to meeting increasing energy demand and controlling global warming by reducing CO_2 emissions. Numerous research studies have been conducted in many countries to harness energy from ocean waves and convert it into electricity. Thus, a wide range of wave energy conversion technologies has emerged with unique challenges in capturing energy from irregular waves. The wave energy conversion technologies can be classified into several categories. The most used categories are based on their working principle, the geometry of the device, and primary location of installation. A brief review of different wave energy conversion technologies is given below-

3.1 Classification According to the Location of the Device:

Shoreline Devices

These devices are installed in shallow water depths and connected to the shore or manmade constructions (e.g., breakwater). Being near to the coast, these are easy to install and maintain and don′t require a long submarine power cable to connect the WEC to the grid. As these are fixed to the sea bottom, mooring system isn′t needed. However, wave power density is less in shallow water compared to the deep sea; thus the power production capacity of these devices is also low.

Nearshore Devices

These devices are installed in moderate water depths (10 to 25 m, or less than one-quarter of the wavelength) and approximately 0.5 km to 2 km out to the sea. These are usually bottom-mounted structures; thus, mooring isn′t required. These devices can harvest most of the energy the waves possess.

Offshore Devices

These devices are installed several kilometers far from the shore in deep water (water depth >40 m). These are generally floating or submerged devices moored to the sea floor. Considering the vast wave energy potential in deep seas, these devices can exploit an abundant amount of energy if properly designed. However, these are difficult to install and maintain. Besides, ensuring the survivability of these devices in extreme sea conditions is a significant design challenge. Also, maintenance of the long submarine cable connecting WEC to the power grid is complex.

3.2 Classification According to the Geometry of the Device:

Point Absorber

Point absorber is an axisymmetrical oscillatory device that is either floating or mounted on the seabed. Point absorbers′ principal dimensions are relatively small compared to the ocean wavelength. The most distinguishing feature of the point-absorber-wave-energy-converter is it can absorb energy from all incident wave directions. Thus, direction characteristics of waves are not considered as a design parameter for optimizing the performance of these types of devices. Moreover, point absorbers can harness energy from waves with small amplitude and short periods and can be installed at different water depths. Although the energy absorption rate of point absorbers is comparatively low, its performance is satisfactory if the size of the device is taken into consideration. There are numerous prototypes available for point absorber devices, one of which is shown in Figure 3.2.

Terminators

Terminator is a long, floating WEC whose principal axis is perpendicular to the direction of wave propagation. Therefore, its main axis is parallel to the wave crests, and thus, it terminates the wave. Unlike point absorbers, the horizontal size of the terminations is comparable to or larger than the incident wavelengths (line absorbers) and absorbs energy in only one direction. These devices are typically installed in onshore or nearshore locations. These mainly have two components- one is stationary, moored to the seafloor or shore, and another is a moving component that moves up and down in response to the waves. However, floating versions of terminations are also developed for offshore applications. One typical terminator is Oyster, shown in Figure 3.3.

Attenuators

An attenuator is a horizontally large, multiple segments, floating WEC whose principal axis is parallel to the direction of wave propagation. Unlike terminators, attenuators have lower areas perpendicular to the waves, thus experiencing lower forces. The device is moored to the seabed in such a way that it can self-align itself to the incoming waves. The power take-off system of the device extracts power from the wave-induced motion of the hinged joints and transfers electricity to the grid. The Pelamis WEC shown in Figure 3.4 is an example of an attenuator WEC.

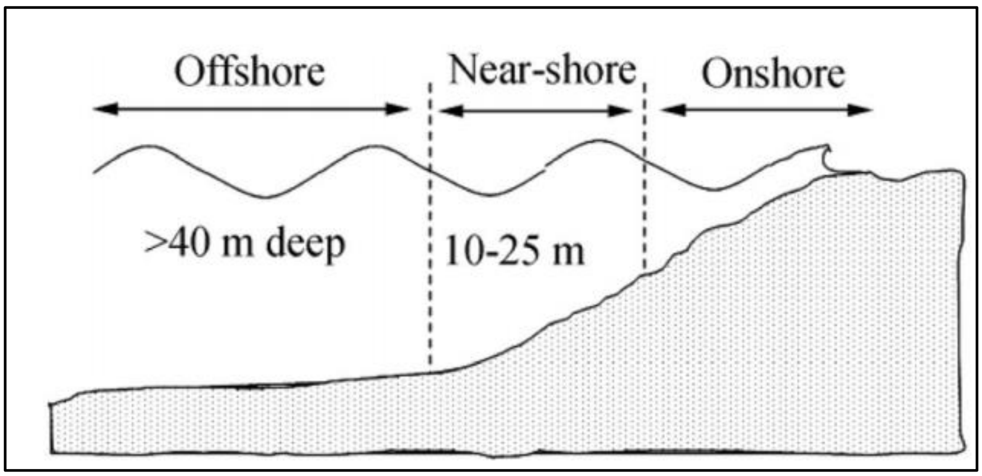

Figure 3.1 Locations of WECs (Source: Bouhrim, 2018)

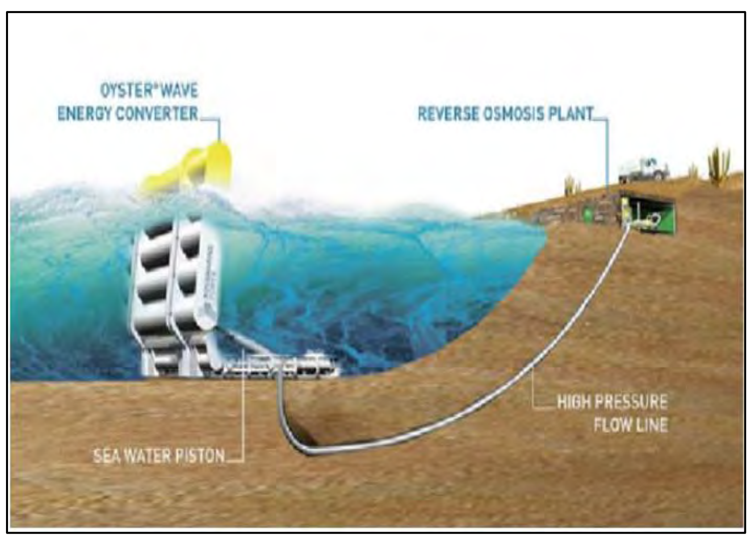

Figure 3.2 Floating point absorber
(Source: Amiri et. al, 2015)

Figure 3.3 Oyster
(Source: Xie and Zou, 2013)

Figure 3.4 Pelamis (Source: Xie and Zou, 2013)

3.3 Classification According to the Working Principle of the Device:

Oscillating Water Column (OWC)

OWC is an indirect wave energy conversion system that converts wave energy to air pressure. It consists of a partially submerged chamber filled with seawater and air. Through an underwater opening to the sea, waves cause the rise and fall of the water column within the chamber like a piston that compress or extend the air to actuate an air-driven turbine and generate electricity. The chamber may be situated on the coastline (onshore) or a floating platform (offshore). A shoreline-based OWC (LIMPET) is shown in the following figure.

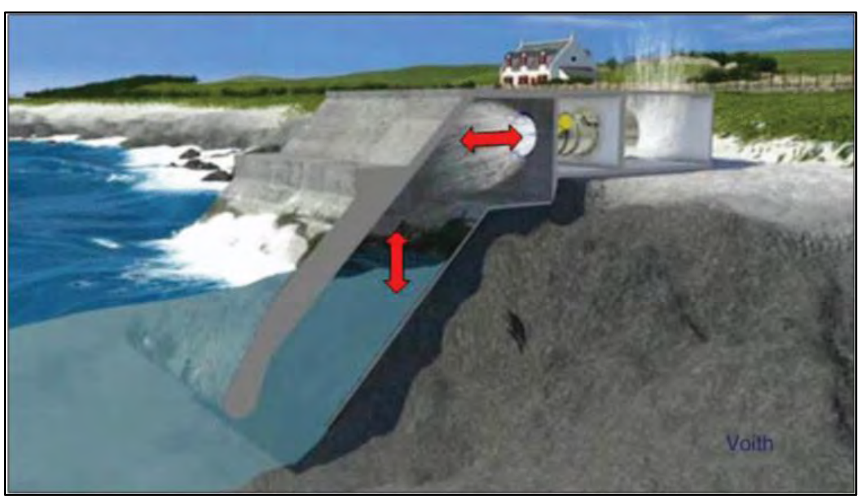

Figure 3.5 Oscillating water column (Source: Czech and Bauer, 2012)

Overtopping Device (OTD)

These devices rely on the physical capture of the incident waves and filling a reservoir a few meters above the average surrounding ocean. The high-pressure water is then released back to the ocean due to gravity through low-head turbines, and the energy of the trapped water is extracted. Overtopping devices can be fixed or floating platforms moored to the seabed.

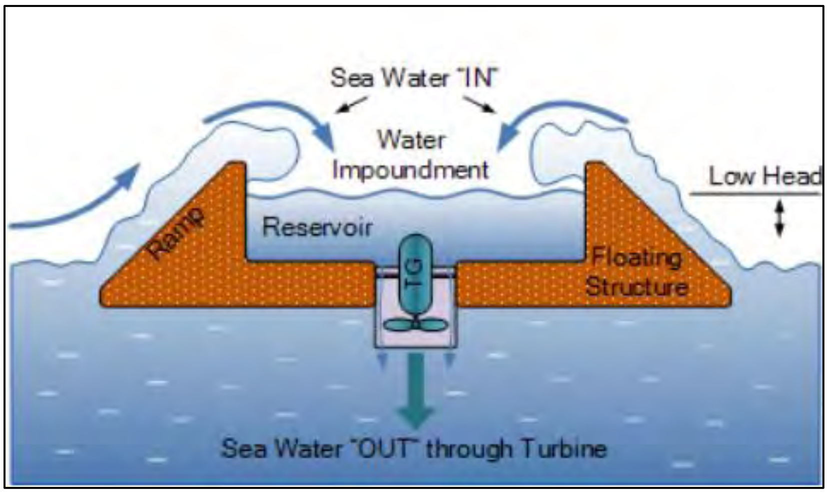

Figure 3.6 Overtopping device (Source: Alternating energy tutorials)

As illustrated in Figure 3.6, the wave overtopping device uses a ramp design on the device to receive the incoming waves at their maximum heights. Instead of using wave kinetic energy like other WECs, these devices take advantage of their potential energy by lifting the water onto a higher level.

Wave Activated Bodies (WAB)

These devices are also known as oscillating body systems. Energy extraction from the ocean waves is done by utilizing the wave-activated oscillatory motions of body parts of a device relative to each other or of one body part relative to a fixed reference. The principal motion of the floating bodies can be primarily described as heave, pitch, and roll. Example: point absorbers, attenuators, terminators.

Apart from the aforementioned categories of WECs, these can also be classified according to the types of power take-off (PTO) systems used. The three most common types of PTO systems used in WECs are air turbines, linear generators, and hydraulic systems.

Figure 2.7 illustrates classification of WEC based on location and operating principles.

3.4 Selection of a suitable WEC for shape optimization

In this study, we have considered a location within 1 km from the shoreline for wave energy exploitation. The average water depth in our intended energy deployment site is 7.1 m. Moreover, according to the wave characteristics data presented in Chapter 2, the values of significant wave heights and energy periods are not very high in our location of interest compared to the global wave energy resources. Liu et al. (2012) showed that point-absorber-wave-energy-converter among different wave energy conversion technologies is the most simple but robust one to convert the low-speed oscillating motion of ocean waves. Besides, as mentioned earlier, they are suitable to be installed in various depths of water. Thus, in this research work, a single-body point-absorber-wave-energy-converter has been chosen to harness energy around Saint Martin′s Island.

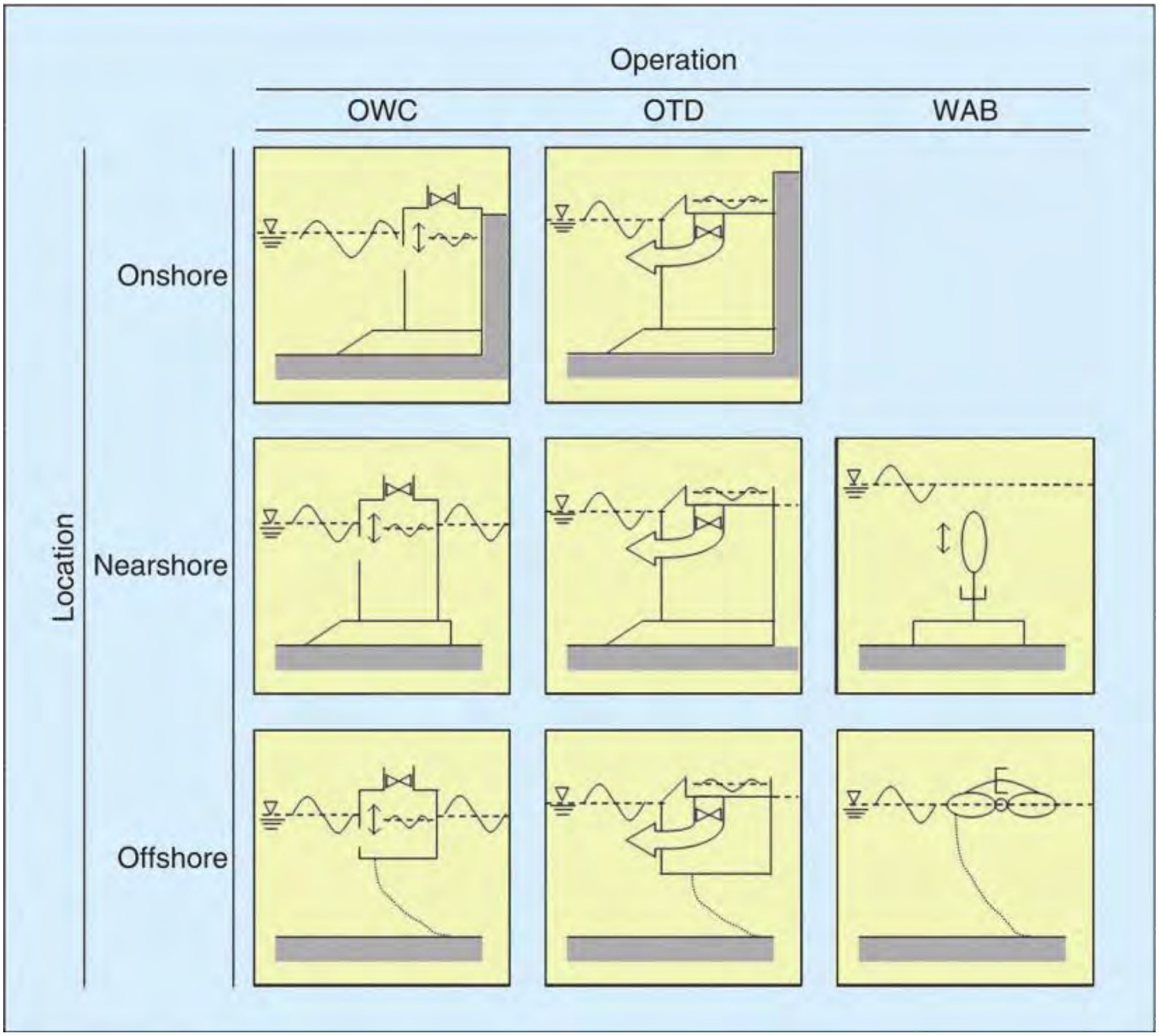

Figure 3.7 Classification according to location and operating principle (Source: Czech and Bauer, 2012)

CHAPTER 4

MOORING CONFIGURATION SELECTION

4.1 Selection of Suitable Mooring System

The primary purpose of the mooring system is to keep device on station in normal loading as well as extreme sea conditions. Currently, a variety of mooring configurations are available for the station keeping of the floating vessels. A brief review of possible mooring configurations is given below-

1. **Catenary mooring system:** It is the most common type of mooring system for shallow water mooring. The mooring lines, commonly known as catenaries, are hanging horizontally to the seabed; thus, there is only horizontal force acting on the anchor point. The restoring force acting on the floating body is mainly due to the weight of the catenaries that helps return the body to the equilibrium position.

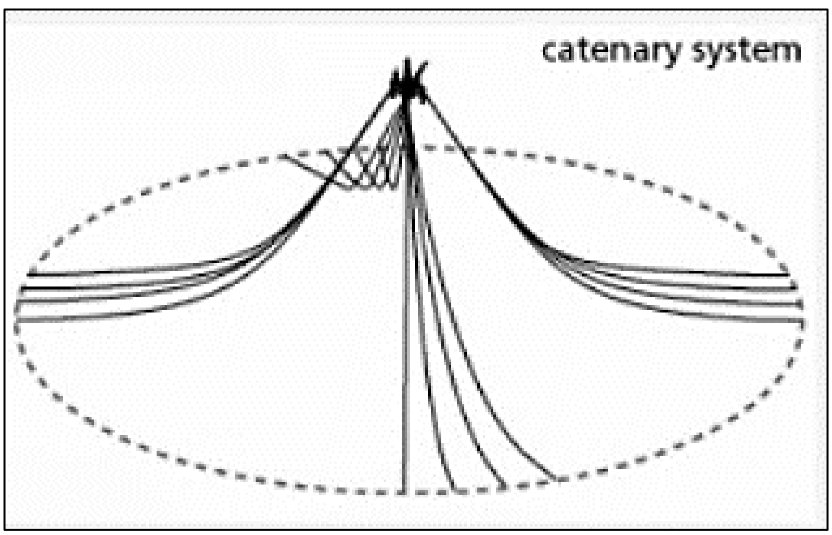

Figure 4.1 Catenary mooring system (Source: ABC moorings)

2. **Taut leg mooring system:** The pre-tensioned mooring line arrived at an angle (varies between 30^0 to 40^0) to the seabed. There will be vertical as well as horizontal forces acting on the acting point. The restoring force acting on the floating body is due to the elasticity of the mooring line.

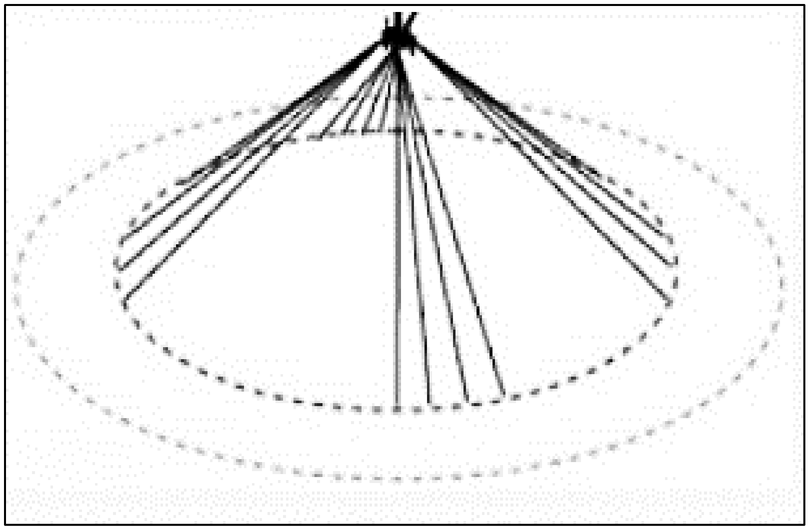

Figure 4.2 Taut mooring system (Source: ABC moorings)

1. **Catenary Anchor Leg Mooring (CALM):** It is an example of a single point mooring system. This system consists of an additional buoy which is secured by catenary mooring lines, and floating structure is moored to the catenary moored buoy.

2. **Single Anchor Leg Mooring (SALM):** In this system, floating structure is moored to a single anchored taut moored buoy.

3. **Fixed tower mooring:** A rigid tower fixed to the seabed is used as a permanent mooring point of the floater.

4. **Dynamic positioning system:** There are two types of dynamic positioning systems. One is active mooring system, in which mooring lines are spread around the floating structure. One central computer controls the tension and slackness of the lines to keep the floater in position. Another one is the positioning of the floater by using propellers or thrusters, which are controlled by a central computer.

As our intended energy harnessing site is in intermediate water depth region, thus catenary mooring system is chosen for fastening the heaving-point-absorber-wave-energy-converter to the seabed.

4.2 Catenary Shape Design

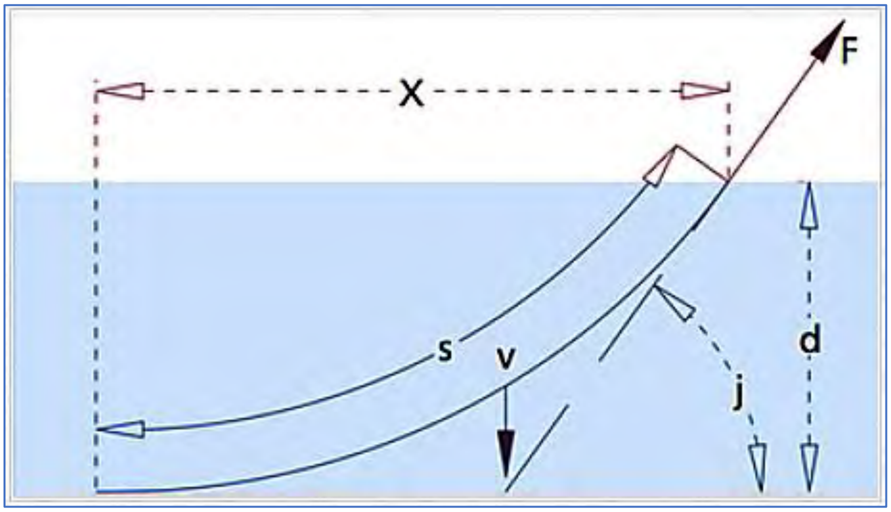

Figure 4.3 Catenary shape parameters (Source: ABC moorings)

The length of the suspended mooring lines (S), horizontal distance between the fairlead and the touchdown point of the mooring line on the seabed (X), weight of the suspended chain (v), catenary shape parameter (b), and vertical distance of the nodes of catenary line from the seabed (y) are calculated using the following equations-

$S = \sqrt{d\,(\frac{2F}{w} - d)}$	(4.1)
$X = (\frac{F}{w} - d)\ ln\,(\frac{S + \frac{F}{w}}{\frac{F}{w} - d})$	(4.2)
$v = w \times s$	(4.3)
$b = \frac{\rho g A}{T_0}$	(4.4)
$y = -\frac{1}{b} ln(cos(bx))$	(4.5)

Here, w = unit weight of the mooring line in water = ρA,

A = cross-sectional area of the thread,

T_0 = normalized horizontal tension component = $\frac{Fx}{\sqrt{S^2+X^2}}$

CHAPTER 5

SELECTION OF SUITABLE MODELLING TECHNIQUE

5.1 Brief Description of Available Numerical Modelling Techniques of WECs

Currently, there are several modelling techniques available to obtain the response of different WECs and predict their potential power capture capability. These include-

i. Frequency-domain models
ii. Time-domain models
iii. Spectral-domain models
iv. Nonlinear potential flow models
v. Computational fluid dynamics models

Besides, to predict the interaction and power production of WEC array, as well as to assess environmental impacts of large-scale wave energy extraction, different modelling techniques of WEC array such as, semi-analytic array models, phase-resolving wave propagation array models, phase-averaging wave propagation array models have been developed.

The main purpose of this present study is to assess and optimize the performance of an isolated heaving-point-absorber-wave-energy-converter. Thus, a good first step is to predict the hydrodynamics of the selected WEC considering linear potential flow theory. At first, brief descriptions of the potential flow theory and linear potential flow WEC models (i.e., frequency-domain modelling of WECs, time-domain modelling of WECs, spectral-domain modelling of WECs) have been given in the following subsections. Afterward, considering the availability of computational resources, a suitable modelling technique will be selected for this study.

5.1.1 Potential flow theory

Potential flow theory assumes that the flow is inviscid, incompressible (density, ρ = constant), and irrotational. An inviscid flow is a flow where there will be no viscous shear stresses to deform fluid elements or rotate fluid particles. The only stress acting on the fluid element is the normal stress due to pressure. Furthermore, in an irrotational flow, fluid particles don't rotate about their own center of gravity, although they can describe circular trajectories. Thus, if an inviscid flow is initially irrotational, it will remain irrotational at all subsequent times.

The fundamental hypothesis of potential flow theory is considered valid for high Reynold's no. flows, where viscous forces are negligible compared to the inertial forces, and thus, the flow can be considered as inviscid. For example, potential flow theory is applicable for analyzing the hydrodynamic interaction of WEC with waves where the amplitudes of waves as well as body motions are small. In contrast, the viscous effect should be taken into consideration when analyzing the interaction of WEC with extreme waves, and in that case, the potential flow theory becomes invalid.

5.1.2 Governing hydrodynamic equation and boundary conditions

Laplace Equation:

The fundamental equation for solving the potential flow is the Laplace equation. In Cartesian coordinate (x, y, z) system, Laplace equation is as follows-

$\nabla^2\varphi = \frac{\partial^2\varphi}{\partial x^2} + \frac{\partial^2\varphi}{\partial y^2} + \frac{\partial^2\varphi}{\partial z^2} = 0$ where, $\varphi =$ velocity potential function. (5.1)

Bottom boundary condition

The boundary condition at the ocean bottom states that there is no flow through the bottom i.e., vertical velocity component is zero at the bottom.

$w = \frac{\partial\varphi}{\partial z} = 0, on\ z = -h$ (Fig. 5.1) (5.2)

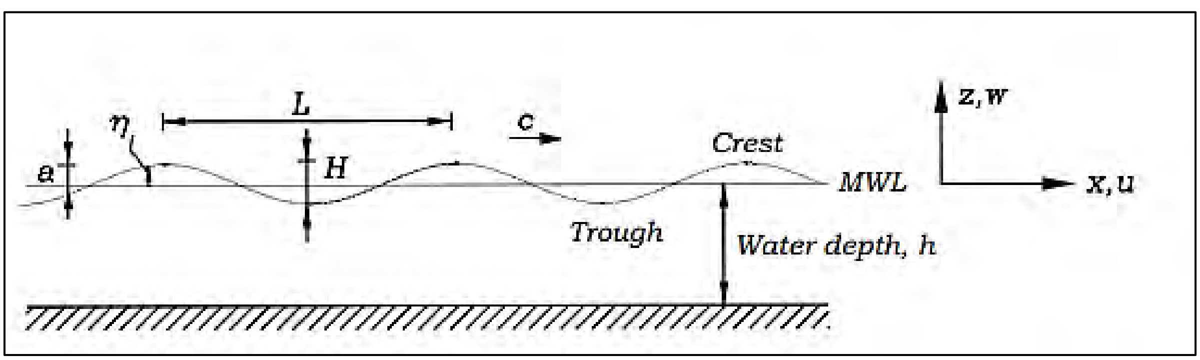

Figure 5.1 Wave parameters and symbols

In Fig. 5.1,

η = free surface elevation from mean water line,

H = wave height,

L = wavelength,

a = wave amplitude, and

$c = L/T$ = phase velocity of wave

Dynamic free surface boundary condition

The dynamic free surface boundary condition assumes that the pressure at the free surface is constant, which is equal to the atmospheric pressure, p_0. Wind induced pressure variations aren't taken into consideration. The condition seems valid as variations of pressure is of much larger scale than the wavelength. Applying the Bernoulli's equation on the free surface -

$$\frac{\partial \varphi}{\partial t} + \frac{1}{2}(\nabla\varphi)^2 + \frac{p_0}{\rho} + g\eta = C, on\ z = \eta\ (x, y, t) \tag{5.3}$$

Here, constant C is equal to atmospheric air pressure (p_0) divided by the water density (ρ). Therefore, dynamic free surface boundary condition can be rewritten as-

$$\frac{\partial \varphi}{\partial t} + \frac{1}{2}(\nabla\varphi)^2 + g\eta = 0, on\ z = \eta\ (x, y, t) \tag{5.4}$$

Kinematic free surface boundary condition

Kinematic free surface boundary condition specifies that a particle at the surface remains at the surface i.e., vertical velocity of the particle at the surface (w) is equal to the vertical velocity of the surface. Therefore, on $z = \eta\ (x, y, t)$,

$$w = \frac{d\eta}{dt} = \frac{\partial \eta}{\partial t} + \frac{\partial \eta}{\partial x}\frac{dx}{dt} + \frac{\partial \eta}{\partial y}\frac{dy}{dt} = \frac{\partial \eta}{\partial t} + u\frac{\partial \eta}{\partial x} + v\frac{\partial \eta}{\partial y} \text{ or} \tag{5.5}$$

$$\frac{\partial \varphi}{\partial z} = \frac{\partial \eta}{\partial t} + \frac{\partial \varphi}{\partial x}\frac{\partial \eta}{\partial x} + \frac{\partial \varphi}{\partial y}\frac{\partial \eta}{\partial y} \tag{5.6}$$

Body-surface boundary condition

The impermeable boundary condition on the body-fluid interface assumes that the component of the fluid velocity normal to the body surface (u_n) must be equal to the body velocity on the direction normal to its surface.

$$\frac{\partial \varphi}{\partial n} = u_n \tag{5.7}$$

Radiation boundary condition

This boundary condition imposes that the potential that satisfies the radiation condition must vanish in a certain way at a great distance from the oscillatory body.

$$\varphi \propto (kr)^{\frac{-1}{2}} e^{-ikr} \, as \, r \to \infty \tag{5.8}$$

Here, r is the radial distance from the body and k is the wave number, defined as-

$k = \frac{2\pi}{L}$,

which is related to the wave frequency by the dispersion relationship,

$\omega^2 = gk \, tanh(kh)$

Similarly, boundary condition for the scattered waves states that the scattered wave potential must vanish in a certain way at a great distance from the body.

The aforementioned boundary-value problem is difficult to solve analytically as-

- Both free surface boundary conditions (dynamic and kinematic) are non-linear partial differential equations.
- Free surface elevation from the mean line, η, is one of the unknows of the problem. However, there is no governing equation with η.

To solve this problem, linear theory is applied based on the following assumptions-

- Wave amplitude is very small compared to the wavelength ($\frac{H}{L} \ll 1$), and

- Wave amplitude is much smaller than the water depth ($\frac{H}{h} \ll 1$)

Also, in linear wave theory, boundary conditions are applied at undisturbed free surface ($z = 0$) instead of instantaneous position, η.

Using order of magnitude analysis, also called scale analysis, the obtained linearized forms of kinematic and dynamic free surface boundary conditions are as follows-

$$\frac{\partial\varphi}{\partial z} = \frac{\partial\eta}{\partial t}, \text{ on } z = 0 \tag{5.9}$$

$$\frac{\partial\varphi}{\partial t} + g\eta = 0, \text{on } z = 0 \tag{5.10}$$

Differentiating equation (8) with respect to ‘t’ we get-

$$\frac{\partial^2\varphi}{\partial t^2} + g\frac{\partial\eta}{\partial t} = 0$$

$$\Rightarrow \frac{\partial\eta}{\partial t} = -\frac{1}{g}\frac{\partial^2\varphi}{\partial t^2}$$

$$\therefore \text{Equation (7)} \Rightarrow \frac{\partial^2\varphi}{\partial t^2} + g\frac{\partial\eta}{\partial t} = 0, \text{on } z = 0 \tag{5.11}$$

Summary of linearized problem

Governing equation: $\frac{\partial^2\varphi}{\partial x^2} + \frac{\partial^2\varphi}{\partial y^2} + \frac{\partial^2\varphi}{\partial z^2} = 0$

Boundary conditions:

- $\frac{\partial\varphi}{\partial z} = 0, \text{on } z = -h$
- $\frac{\partial^2\varphi}{\partial t^2} + g\frac{\partial\eta}{\partial t} = 0, \text{on } z = 0$
- $\frac{\partial\varphi}{\partial n} = u_n$
- $\varphi \propto (kr)^{\frac{-1}{2}} e^{-ikr} \text{ as } r \to \infty$

5.1.3 Equation of motion

The fundamental equation of motion for a WEC is obtained by using the Newton's second law of motion which is stated as-

$$\sum F = ma \tag{5.12}$$

The total forces acting on the WEC can be represented as follows-

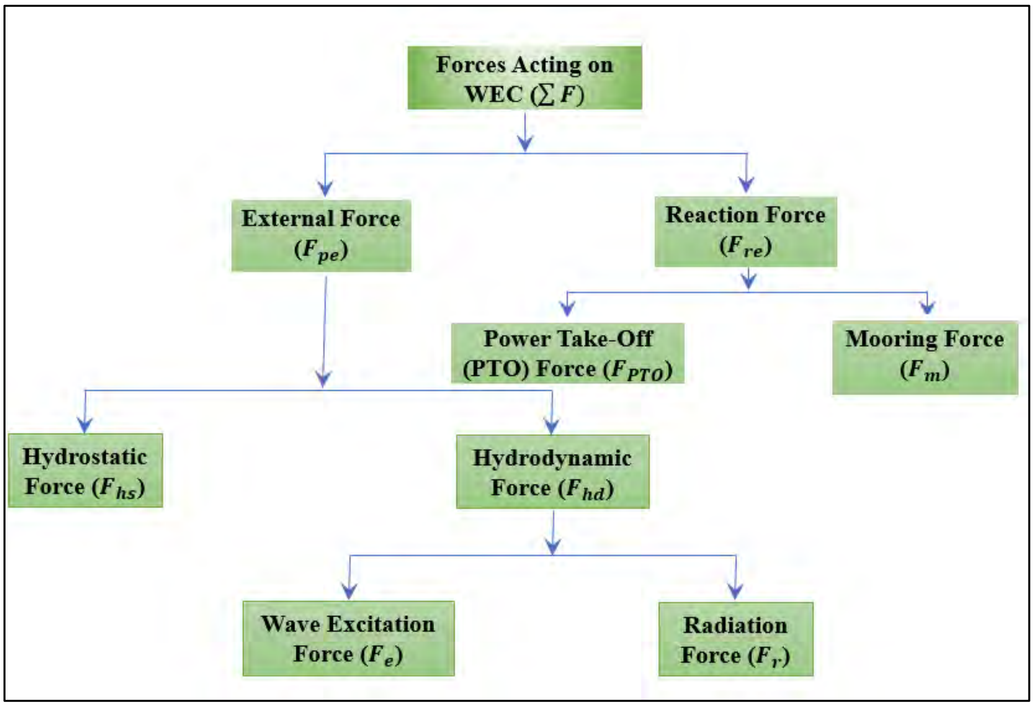

Figure 5.2 Types of forces acting on the wave energy converter

Forces arising from the variation of hydrostatic pressure distribution due to the body motions are referred to hydrostatic forces (F_{hs}) (the effects of buoyancy and gravity are included in this division). Excitation force (F_e) is caused by the action of incident waves on the motionless body. Radiation force (F_r) arises due to the oscillatory movement of the body in the absence of incident wave field. It consists of added mass force (force proportional to body acceleration) and wave damping force (force proportional to body velocity). Apart from these external forces, WECs also experiences wave drift force, current force, drag force (form drag and skin friction). However, for preliminary analysis, only the most important external forces are considered in the equation of motion. Equation (5.12) can be written as-

$$ma = F_{hs} + F_e + F_r + F_{PTO} + F_m \tag{5.13}$$

5.1.4 Linear potential flow WEC models

Frequency-domain models

In frequency-domain modelling technique, linear wave theory is used to model the hydrodynamic interaction of WEC and ocean waves. Also, reaction forces caused by PTO equipment and mooring systems are represented by linear equations. The response of WEC is calculated as a function of wave frequency. All body motions and motion of water waves are considered harmonic with the same frequency. The velocity potential which satisfies Laplace equation within the fluid domain is defined as-

$$\varphi\,(x, y, z, t) = Re\,\{\hat{\varphi}(x, y, z)e^{i\omega t}\} \tag{5.14}$$

In equation (5.14), ω is the wave frequency, $e^{i\omega t}$ represents sinusoidal time dependent term with unit amplitude and $\hat{\varphi}(x, y, z)$ represents the frequency dependent term or complex amplitude. In frequency-domain, the linear potential flow boundary value problem discussed in section (5.1.3) takes the following form-

Governing equation	$\frac{\partial^2\hat{\varphi}}{\partial x^2} + \frac{\partial^2\hat{\varphi}}{\partial y^2} + \frac{\partial^2\hat{\varphi}}{\partial z^2} = 0$
Bottom b.c.	$\frac{\partial\hat{\varphi}}{\partial z} = 0, on\ z = -h$
Free surface b.c.	$\frac{\partial^2\hat{\varphi}}{\partial t^2} + g\frac{\partial\eta}{\partial t} = 0, on\ z = 0$
Body surface b.c.	$\frac{\partial\hat{\varphi}}{\partial n} = \hat{u}_n$
Far-field b.c.	$\hat{\varphi}_r \propto (kr)^{\frac{-1}{2}}\, e^{-ikr}$ as $r \to \infty$, and $\hat{\varphi}_s \propto (kr)^{\frac{-1}{2}}\, e^{-ikr}$ as $r \to \infty$

where $\hat{\varphi}$, $\hat{\varphi}_r$, $\hat{u}_n$ represent complex amplitude of total velocity potential, radiation potential, and fluid velocity normal to the body surface.

The time independent velocity potential function $\hat{\varphi}(x, y, z)$ can be decomposed into contributions from the incident wave field in the absence of the body $(\hat{\varphi}_i)$, radiated waves due to the six basic modes of body motion in calm water $(\hat{\varphi}_r)$, and diffracted or scattered waves due to the interaction between incident wave and motionless body $(\hat{\varphi}_s)$.

The incident-velocity potential $(\hat{\varphi}_i)$ satisfies Laplace equation within the fluid domain, linear free surface boundary condition and bottom boundary condition. In finite water depth, h, it can be calculated using the following equation-

$$\hat{\varphi}_i = \frac{iga}{\omega}\frac{cosh[k\ (z+h)]}{cosh\ kh}\ e^{-ik(x\cos\beta\ +\ ysin\beta)} \tag{5.15}$$

where, β is the angle between the wave propagation direction and x-axis (Fig. 5.3) and,

$\frac{cosh[k\ (z+h)]}{cosh\ kh}$ is the decay function, which indicates the decay in the dynamic pressure with the distance below the mean waterline. If $h \to \infty$, $\frac{cosh[k\ (z+h)]}{cosh\ kh} = \frac{e^{k(z+h)} + e^{-k(z+h)}}{e^{kh} + e^{-kh}} \to 1.$

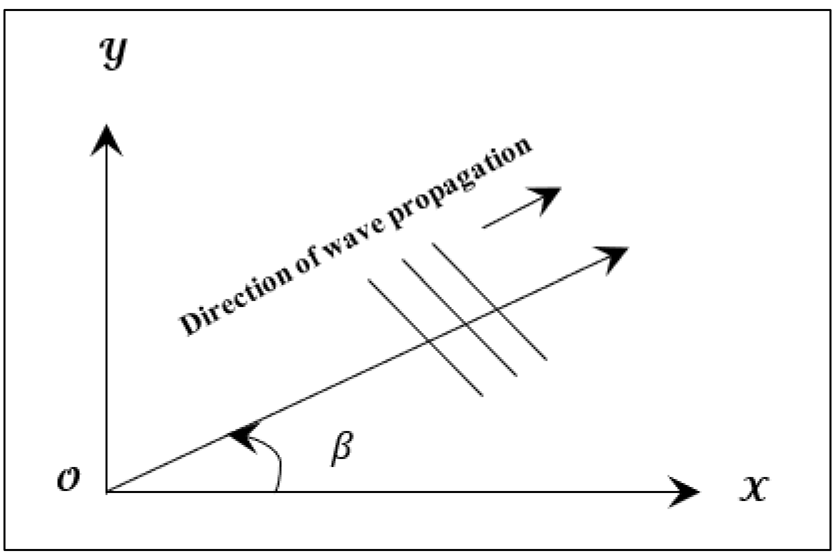

Figure 5.3 Direction definition

The scattered potential $(\hat{\varphi}_s)$ satisfies Laplace equation within the fluid domain, linear free surface boundary condition, bottom boundary condition, body surface boundary condition considering the body is stationary, and far-field boundary condition. The body surface boundary condition considering motionless body states that the normal velocity due to incident wave is equal and opposite to the normal velocity due to the scattered wave at the body surface.

$$\frac{\partial \widehat{\varphi_i}}{\partial n} = -\frac{\partial \widehat{\varphi_s}}{\partial n} \tag{5.16}$$

Finally, the potential due to radiated waves ($\hat{\varphi}_r$) satisfies Laplace equation within the fluid domain, linear free surface boundary condition, bottom boundary condition, body surface boundary condition, and far-field boundary condition. The radiation potential due to the oscillatory motion of the body in calm water can be decomposed into six components, one for each degree of freedom (Figure 5.4). Let $\hat{n}_j$ represents the complex amplitude of vertical velocity component in jth degree of freedom. The body surface boundary condition for radiation potential can be written as-

$$\frac{\partial \widehat{\varphi_r}}{\partial n} = i\omega \hat{n}_j \tag{5.17}$$

Thus, radiation potential can be expressed as-

$$\hat{\varphi}_r = i\omega \sum_{j=1}^{N} \hat{\xi}_j \, \varphi_j, N = \text{no. of degrees of freedom} = 6 \tag{5.18}$$

where, $\hat{\xi}_j$ represents complex amplitude in degree of freedom j.

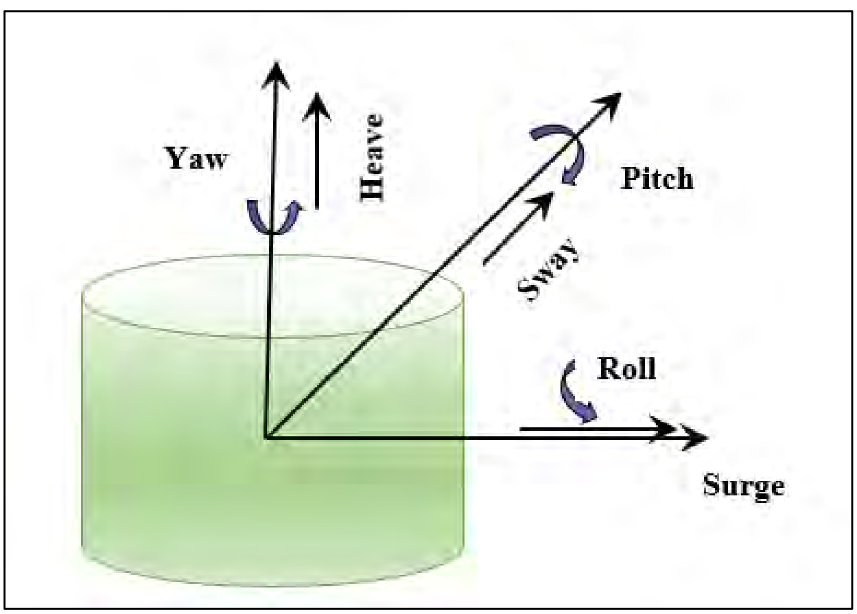

Figure 5.4 Six modes of oscillation of a floating body

Equation of motion in frequency-domain: For single degree of freedom ($N = 1$), the equation of motion is expressed as-

$$-\omega^2 m\hat{\xi}\ (\omega) = \widehat{F_{hs}}\ (\omega) + \widehat{F_e}\ (\omega) + \widehat{F_r}\ (\omega) + \widehat{F_{PTO}}\ (\omega) + \widehat{F_m}\ (\omega) \tag{5.19}$$

where, the hat symbol,`^′ represents complex amplitudes of body displacement and forces.

Calculation of hydrodynamic forces:

When the wave velocity potentials are known, the dynamic part of the fluid pressure is calculated using the linearized Bernoulli's equation, i.e.,

$$p = \rho \frac{\partial \varphi}{\partial t} \tag{5.20}$$

By integrating dynamic fluid pressure over the wetted surface of the body, the hydrodynamic force on a floating body is calculated. The time-independent part of hydrodynamic force can be written as-

$$\widehat{F_{hd}} = \int_S \hat{p}\ n\, dS = \int_S \rho \frac{\partial \hat{\varphi}}{\partial t}\, n\, dS$$, where n = unit vector normal to the body surface

$$\therefore\ \widehat{F_{hd}} = \int_S \rho \frac{\partial}{\partial t}(\widehat{\varphi_\iota} + \widehat{\varphi_S} + \widehat{\varphi_r})\, n\, dS \tag{5.21}$$

As mentioned earlier,

$$\varphi\ (x, y, z, t) = Re\ \{\hat{\varphi}(x, y, z)e^{i\omega t}\} \Longrightarrow \therefore\ \frac{\partial \varphi}{\partial t} = i\omega\varphi\ (x, y, z, t) = Re\ \{\hat{\varphi}(x, y, z)e^{i\omega t}\}$$

Equation (5.21) ⟹

$$\widehat{F_{hd}} = i\omega\rho \int_S \widehat{\varphi_\iota}\, n\, dS + i\omega\rho \int_S \widehat{\varphi_S}\, n\, dS + i\omega\rho \int_S \widehat{\varphi_r}\, n\, dS$$

$$\widehat{F_{hd}} = i\omega\rho \int_S \widehat{\varphi_\iota}\, n\, dS + i\omega\rho \int_S \widehat{\varphi_S}\, n\, dS + i\omega\rho \int_S (i\omega \textstyle\sum_{j=1}^{N} \widehat{\xi_J}\ \varphi_j) n\, dS$$

$$\widehat{F_{hd}} = i\omega\rho \int_S \widehat{\varphi_\iota}\, n\, dS + i\omega\rho \int_S \widehat{\varphi_S}\, n\, dS - \omega^2\rho \int_S (\textstyle\sum_{j=1}^{N} \widehat{\xi_J}\ \varphi_j) n\, dS \tag{5.22}$$

First two terms on the R.H.S of the equation (5.22) represents wave excitation force ($\widehat{F_e}$) and third term represents wave radiation force ($\widehat{F_r}$).

Wave excitation force: In small amplitude waves, wave excitation force is divided into two components- first order incident wave force, also known as Froude-Krylov force and the scatter or diffraction force.

$$\therefore\ \widehat{F_e} = \widehat{F_{FK}} + \widehat{F_s} \tag{5.22}$$

where, Froude-Krylov force due to incident wave is-

$$\widehat{F_{FK}} = i\omega\rho \int_S \widehat{\varphi_\iota}\, n\, dS\,, \tag{5.23}$$

and diffracting force due to diffraction is-

$$\widehat{F_s} = i\omega\rho \int_S \widehat{\varphi_s}\, n\, dS \tag{5.24}$$

If the characteristic dimension of the motionless body is very small compared to the wavelength, the disturbance in the incident wave field due to the presence of the body is very small and can be neglected. Thus, for small bodies, diffracting force can be neglected in excitation force calculation.

Wave radiation force: Radiation force ($\widehat{\mathrm{F_r}}$) can be expressed as-

$$\widehat{F_r} = i\omega\rho \int_S \widehat{\varphi_r}\, n\, dS$$

$\widehat{\varphi_r}$ can be expressed in real and imaginary parts.

$$\Rightarrow \widehat{F_r} = i\omega\rho \int_S [Re(\widehat{\varphi_r}) + i\, Im(\widehat{\varphi_r})]\, n\, dS$$

$$= i\omega\rho \int_S [Re(\widehat{\varphi_r})]\, n\, dS - \omega\rho \int_S [Im(\widehat{\varphi_r})]\, n\, dS$$

$$= i\omega B + \omega^2 A$$

where, A = added mass coefficient = $-\frac{\rho}{\omega}\int_S [Im(\widehat{\varphi_r})]\, n\, dS$, and

B = damping coefficient = $\rho \int_S [Re(\widehat{\varphi_r})]\, n\, dS$

As $\hat{\varphi}_r = i\omega \sum_{j=1}^{N} \widehat{\xi_J}\ \varphi_j$, for single degree of freedom system it can be written as $\hat{\varphi}_r = i\omega\hat{\xi}\phi$.

Thus, $\widehat{F_r} = i\omega B\hat{\xi} + \omega^2 A\hat{\xi}$. (5.25)

Here,

displacement, $\xi(t) = Re\left[\hat{\xi}(\omega)e^{i\omega t}\right]$, $velocity, \dot{\xi(t)} = Re\left[i\omega\hat{\xi}(\omega)e^{i\omega t}\right]$, and

accleration, $\ddot{\xi}(t) = Re[\omega^2\hat{\xi}(\omega)e^{i\omega t}]$

In frequency domain, velocity = $i\omega\hat{\xi}(\omega)$, and acceleration = $\omega^2\hat{\xi}(\omega)$

Therefore, in equation (5.25), the first term in the R.H.S represent damping or dissipative force as it is proportional to the velocity and the second term represents inertia force as it is proportional to the acceleration.

Calculation of hydrostatic force: The buoyancy force that acts on the body due to its additional immersion in water can be calculated using the following formula-

$$\widehat{F_{hs}} = -k\hat{\xi} \tag{5.26}$$

$k =$ hydrostatic coefficient, also known as hydrostatic spring stiffness $= \rho g S$
where, S = cross-sectional area at undisturbed sea level.

Reaction forces (PTO and Mooring): The PTO system applied in the majority of wave extraction devices shows complex non-linear behavior. However, in the frequency-domain linear representation of PTO force is done by replacing it with a linear damper or a linear spring-damper system. For a linear spring-damper system, the complex amplitude of PTO force will consist of two components- one is proportional to velocity (PTO damping force), and another one is proportional to displacement (restoring force) (Figure 5.5).

$$\widehat{F_{PTO}} = -i\omega B_{PTO}\hat{\xi} - K_{PTO}\hat{\xi} \tag{5.27}$$

here, B_{PTO} = PTO damping coefficient, and K_{PTO} = PTO spring stiffness.

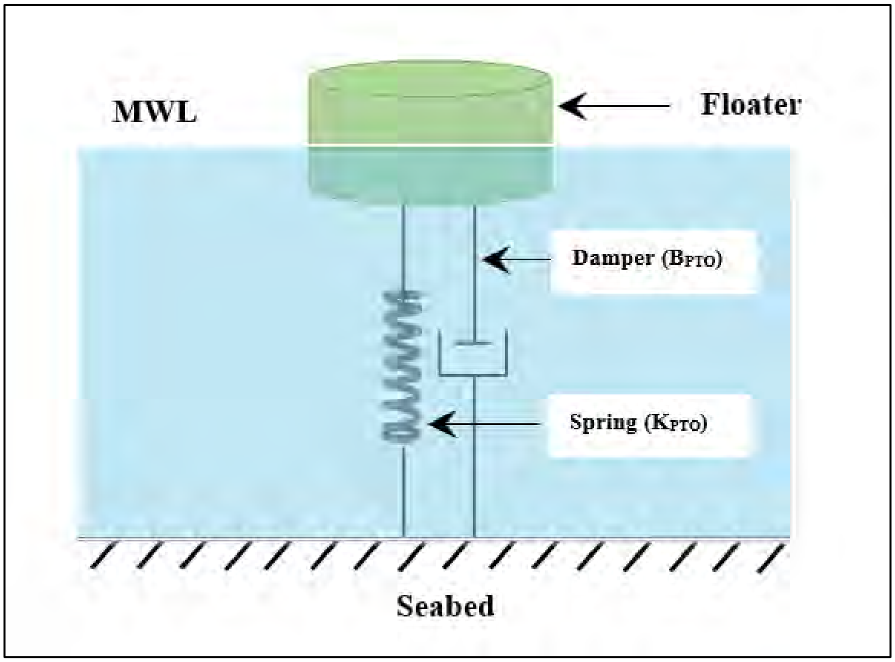

Figure 5.5 Representation of PTO using linear spring-damper system

Similarly, complex amplitude of linear mooring force can be represented as-

$$\widehat{F_m} = -k_m\hat{\xi} \tag{5.28}$$

here, k_m = mooring spring stiffness.

Substituting the expression of different forces in equation (5.19), the equation of motion becomes-

$$-\omega^2 m\hat{\xi}\ (\omega) = -k\hat{\xi} + \widehat{F_e}\ (\omega) + i\omega B\hat{\xi} + \omega^2 A\hat{\xi} + -i\omega B_{PTO}\hat{\xi} - K_{PTO}\hat{\xi} + -k_m\hat{\xi}$$

$$\Rightarrow [-\omega^2(m + A) + k + K_{PTO} + k_m + i\omega\ (B + B_{PTO})]\hat{\xi} = \widehat{F_e}$$

$$\Rightarrow \hat{\xi} = \frac{\widehat{F_e}}{[-\omega^2(m + A) + k + K_{PTO} + k_m + i\omega\ (B + B_{PTO})]} \tag{5.29}$$

This is the formula of calculating complex amplitude $\hat{\xi}$ considering single degree of freedom of the body.

For multiple degree of freedom system, it can be represented as follows-

$$\hat{\xi} = \frac{\widehat{\boldsymbol{f}_e}\, A_w}{[-\omega^2(\boldsymbol{m} + \boldsymbol{A}) + \boldsymbol{k} + \boldsymbol{K}_{PTO} + \boldsymbol{k}_m + i\omega\ (\boldsymbol{B} + \boldsymbol{B}_{PTO})]} \tag{5.30}$$

here, bold font denotes vector or matrix. A_w = wave amplitude, $\widehat{\boldsymbol{f}_e}$ = vector of complex amplitudes of excitation load for unit wave amplitude.

After obtaining the value of $\hat{\xi}$, assuming sinusoidal waves, the mean power absorption of a WEC over a wave period can be obtained using the following formula-

$$P_m = u_{rel}(\omega)\,\widehat{F_{PTO}} \tag{5.31}$$

Here, $u_{rel}(\omega)$ = relative velocity between the body and damper.

Although frequency-domain analysis gives insightful look for predicting preliminary response of WECs, it has many limitations-

i. The assumption of linearity becomes invalid for extreme sea conditions, where viscous effects become prominent.
ii. It can't predict WECs response accurately around resonance (amplitude becomes too high and linear theory isn't applicable).
iii. The assumption of monochromatic wave doesn't represent real sea states.
iv. Linear representation PTO force isn't sufficiently realistic.

Time-domain models

One of the major limitations of frequency-domain modelling is to represent reaction forces (i.e., PTO and mooring forces) by linear equations in the mathematical model. In reality, WEC control strategies are very complex and highly non-linear process. In addition, mooring forces as well as viscous damping forces are non-linear in nature. To introduce these non-linearities in the mathematical modelling of energy extraction mechanism and to predict more realistic behavior of the WECs under irregular waves, time-domain analysis is used.

Equation of motion in time-domain: In time-domain, the equation of motion of a floating body about its center of gravity can be expressed as-

$$m_{ij}\ddot{x}_j(t) = F_{exc}(t) + F_{rad}(t) + F_{hs}(t) + F_{PTO}(t) + F_m(t) + F_v(t) \tag{5.32}$$

where, $\ddot{x}_j$ = device acceleration, $F_{exc}(t)$ = wave excitation force, $F_{hs}(t)$ = hydrostatic restoring force, $F_v(t)$ = viscous damping force.

In equation (5.32), $F_{exc}(t), F_{rad}(t)$, and $F_b(t)$ are estimated using the hydrodynamic coefficients obtained from linear potential flow models. The radiation term is calculated using the following equation-

$$F_{rad}(t) = -A_{ij}^{\infty}\ddot{x}_j(t) - \int_{-\infty}^{t} K_{ij}(t-\tau)\,\dot{x}_j(\tau)\,d\tau \tag{5.33}$$

where, A_{ij}^{∞} is the added mass matrix at infinite frequency, which can be determined as-

$$A_{ij}^{\infty} = lim_{\omega\to\infty}A_{ij}(\omega) \tag{5.34}$$

In equation (5.34), $A_{ij}(\omega)$ obtained from the frequency-domain boundary element method (BEM) solver.

K_{ij} *(t)* is the radiation impulse response function (RIRF), also known as memory function. The convolution integral in Equation (5.33) represents the memory effect on the WEC dynamics. Radiated waves are generated due to the motions of the body. However, these waves propagate long after the motions have stopped. To include the effects of the forces due to the past motions of the body, radiated forces are modelled by the convolution of RIRF. After obtaining frequency-dependent radiation damping coefficient, $B_{ij}(\omega)$ and added mass coefficient, $A_{ij}(\omega)$, RIRF can be calculated using one of the following two equations-

$$K_{ij}(t) = \frac{2}{\pi}\int_0^{\infty} B_{ij}(\omega)\,cos\,\omega t\,d\,\omega \tag{5.35}$$

$$K_{ij}(t) = -\frac{2}{\pi}\int_0^{\infty} \omega\bar{A}_{ij}(\omega)\,sin\,\omega t\,d\,\omega,\ [\bar{A}_{ij}(\omega) = A_{ij}(\omega) - A_{ij}^{\infty}] \tag{5.36}$$

Equation (5.35) is normally used to calculate RIRF because it is less prone to numerical inaccuracies (Folley, 2016). For the solution convergence, $K_{ij}(t) \longrightarrow 0$, at $t \longrightarrow \infty$.

Notably, after computing $K_{ij}(t)$ using Equation (5.35), added mass coefficient at infinite frequency can also be calculated using the following equation-

$$A_{ij}^{\infty} = \frac{1}{N}\sum_{n=1}^{N}(A_{ij}(\omega_n) + \frac{1}{\omega_n}\int_0^{\infty} K_{ij}(t)\,sin\omega_n t\,dt \tag{5.37}$$

Substituting equation (5.33) in equation of motion, we get-

$$m_{ij}\ddot{x}_j\,(t) \;=\; F_{exc}(t) - A_{ij}^{\infty}\ddot{x}_j\,(t) - \int_{-\infty}^{t} K_{ij}\,(t-\tau)\dot{x}_j(\tau)\,d\tau + F_b(t) + F_{PTO}(t) + F_m(t) + F_v(t)$$

This equation is known as Cummins′ equation, which is an integro-differential equation of order two with convolution terms.

The hydrostatic forces in time-domain model can be expressed as a simple linear function of body displacement, $x_j(t)$ for small amplitudes of motion. For larger amplitudes, non-linear representation of hydrostatic forces is used. Besides, in most cases, numerical integration of the hydrostatic pressure over the wetted surface of the body for a range of displacements is performed.

The excitation force in time-domain can be calculated by using its frequency-dependent expressions, i.e., by taking convolution of the wave surface elevation and impulse response function.

$$F_{exc}(t) = \int_{-\infty}^{+\infty} \eta(\tau) f_{exc}\,(t-\tau)d\tau, \tag{5.38}$$

η = wave elevation, and

$$f_{exc}\,(t) \;=\; \text{impulse response function (IRF)} \;=\; \frac{1}{2\pi}\int_{-\infty}^{+\infty} F_{exc}\,(\omega,\theta)e^{i\omega t}d\omega$$

$F_{exc}\,(\omega)$ is the frequency-dependent excitation force component obtained from BEM solver and θ is the wave direction. This convolution integral form of excitation force is used to model user defined wave elevation case.

For regular waves, it is calculated using the following equation-

$$F_{exc}(t) = \Re\,[R_f(t)\,\frac{H}{2} F_{exc}(\omega,\theta)e^{i\omega t}] \tag{5.39}$$

here, H = wave height, and $R_f(t)$ = ramp function, which value depends on simulation time (t) and ramp time $(\mathrm{t_r})$.

$$R_f(t) \;=\; \begin{cases} \frac{1}{2}(1 + cos\,(\pi + \frac{\pi t}{t_r})) & \frac{t}{t_r} < 1 \\ 1 & \frac{t}{t_r} \geq 1 \end{cases}$$

For irregular waves with wave spectrum $S\,(\omega)$,

$$F_{exc}(t) = \Re[R_f(t) \sum_{j=1}^{N} F_{exc}(\omega_j, \theta)\, e^{i(\omega_j t + \emptyset_j)} \sqrt{2S(\omega_j) d\omega_j}] \quad (5.40)$$

where, $\emptyset$ is the randomized phase angle and N is the number of frequency bands selected to discretize the wave spectrum.

The convolution integral part of the Cummins′ equation can be evaluated by using one of the following three methods-

- direct solution of the convolution integral,
- state space (SS) representation,
- Prony′s method

Extensive descriptions of these methods can be found in the literature (Folley, 2016).

Once the convolution integral is transformed into a linear form, the Cummins′ equation is solved using different numerical schemes, e.g., backward Euler, Crank–Nicolson, fourth order Runge–Kutta, etc. Although time-domain models are good enough to produce accurate estimate of dynamic response and performance by including non-linear components, these models are highly computationally demanding than frequency-domain models. In addition, the accuracy of the results depends on the model formulation, ODE solver used, and simulation duration. This modelling technique isn′t suitable where many simulations are required.

Spectral-domain Models

In spectral-domain modelling technique, the equation of motion of a floating body is solved using probabilistic model of system dynamics. The general structure of a spectral-domain model is shown in the following figure.

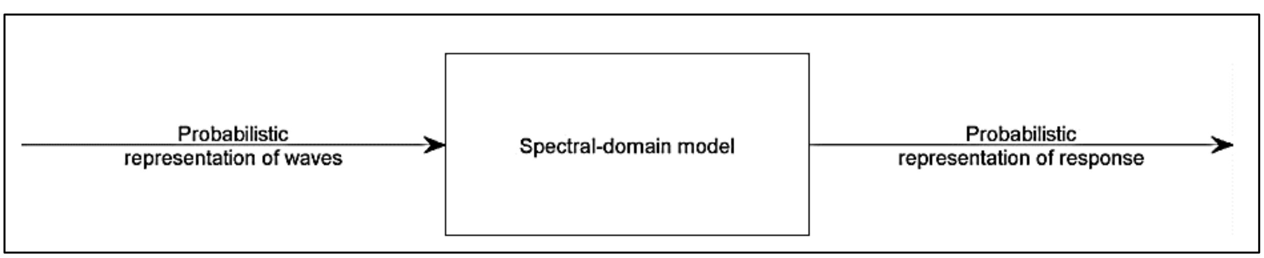

Figure 5.6 General structure of spectrum-domain model (Source: Folley, 2016)

As shown in the figure, in spectral-domain modelling of WECs, input is the probabilistic representation of waves and output is the probabilistic representation of the model response. The hydrodynamic forces in spectral-domain models are typically obtained using a linear potential flow solver. The non-linear forces can be represented as quasilinear coefficients. Current spectrum-domain models assume that the response of WEC is Gaussian. An extensive description of spectrum-domain modelling of WECs, solution techniques, practical examples, and limitations can be found in 'Numerical Modelling of Wave Energy Converters (Folley, 2016)'.

5.1.5 Selection of suitable modelling technique

In the present study, time-domain numerical modelling and simulation have been used to determine the system's power performance for different combinations of design parameters. WEC-Sim (Wave Energy Converter Simulator) - a time-domain modeling tool is used to predict the power generation performance of the system. At first, core hydrodynamic coefficients have been estimated using the frequency-domain boundary element method (BEM) solver with linear potential flow assumptions (Ansys-AQWA). Estimated hydrodynamic coefficients are used to determine the dynamic responses as well as the power output of the system.

The code structure of WEC-Sim is illustrated in the following figure-

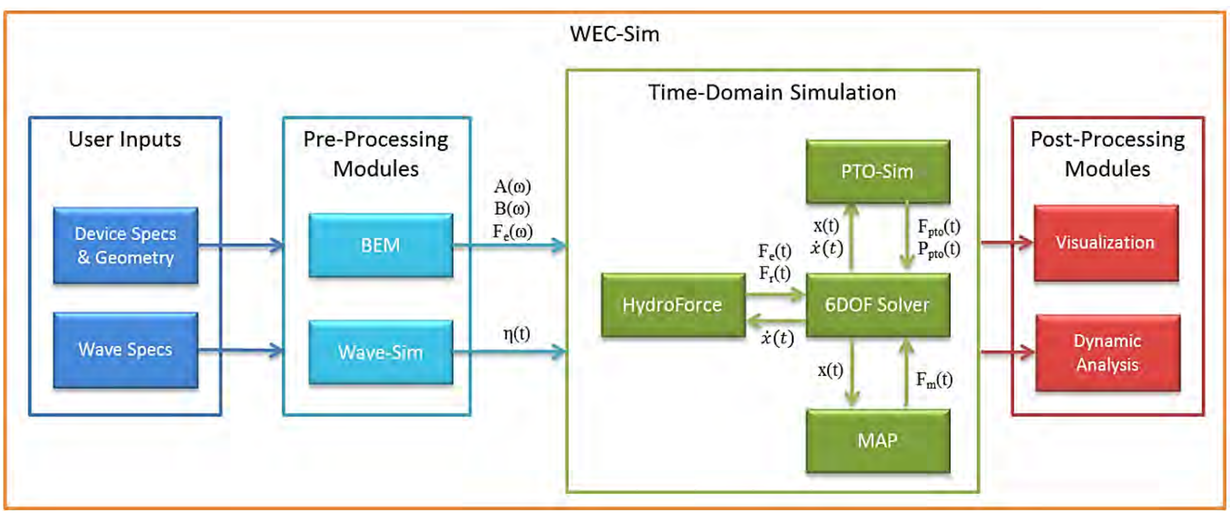

Figure 5.7 WEC-Sim code structure (Source: Yu et al., 2014)

As can be seen in Figure (5.7), there are three modules-

1) Pre-processing module,
2) Time-domain module, and
3) Post-processing module.

At first, simple structural analysis needs to be done to obtain the geometrical properties of the system, such as mass, moment of inertia, center of gravity, etc. Wave characteristics can be specified either as regular waves, i.e., specifying wave height and wave period or as wave spectrum. In the pre-processing module, WEC-Sim generates wave time-series data. A boundary element solver is used to generate frequency-dependent hydrodynamic coefficients. In the present study, Ansys-AQWA is the boundary element method solver. The basic equations used to perform hydrodynamic diffraction analysis are outlined in Section 5.1 (Frequency-domain modelling of WECs). In AQWA, a boundary integration approach is employed to solve the fluid velocity potential.

To perform time-domain analysis, a multi-body dynamics WEC model is created using Simulink. Time-domain modules simulate specific device components. System dynamic response is obtained by solving Cummins equation numerically using the 4th order Runge-Kutta algorithm.

Post-processing modules are responsible for result visualization and analysis.

5.1.6 Applicability of linear wave theory

In the intended energy deployment site (Longitude- 92.317^{0}N, Latitude- 20.566^{0}E), the average water depth (h) is 7.1 m. Besides, based on the results of 4-year numerical simulation, the average values of significant wave height (H_{sig}), wave energy period (T_e), and wavelength (L) were found 1.164 m, 4.14 s, and 27.5 m, respectively.

$$\therefore \frac{h}{L} = \frac{7.1}{27.5} = 0.26, \tag{5.41}$$

$$\frac{\mathrm{h}}{\mathrm{gT_e}^2} = \frac{7.1}{9.81 \times (4.14)^2} = 0.042, \text{and} \tag{5.42}$$

$$\frac{H_{sig}}{gT^2} = \frac{1.164}{9.81 \times (4.14)^2} = 0.007 \tag{5.43}$$

The ratio of $\frac{h}{L}$ indicates that the region is an intermediate water depth region ($\frac{1}{2} \leq \frac{h}{L} \leq \frac{1}{20}$). Thus, water depth will influence the amplitude and direction of waves. Besides, according to the following figure, the intersecting point ($\frac{h}{gT_e{}^2}, \frac{H_{sig}}{gT_e{}^2}$) is outside the area of applicability of linear wave theory.

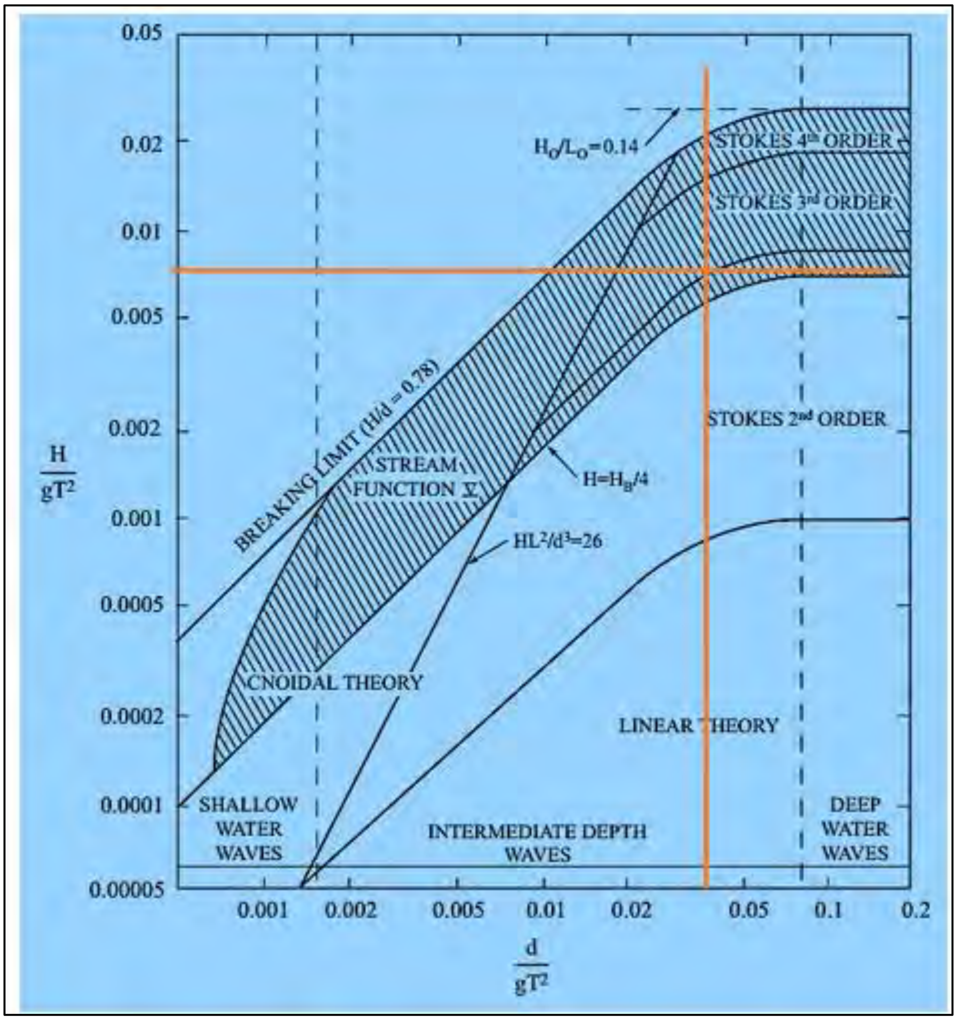

Figure 5.8 Area of applicability of wave theory

Therefore, non-linear wave theory will give more accurate physical description of waves for our location of interest. However, due to resource limitations, in this study, we have used linear potential flow solver to obtain the hydrodynamic coefficients of the wave forcing components. Thus, solution of governing equation based on the linearization of hydrodynamics will incorporate some errors in the results.

CHAPTER 6

OPTIMIZATION STRATEGY OF POINT ABSORBER WAVE ENERGY CONVERTER

Only the heaving motion of the point absorber has been considered in this study to simplify the optimization process. Three different buoy shapes (cylindrical, spherical, and hexagonal) are considered for shape optimization purpose. The optimal design will be selected through manual parametric study. Initially, different combinations of drafts and diameters of a cylindrical buoy will be selected for creating computer model representations of the system. The geometrical parameters of the heaving buoy, i.e., draft, diameter, etc., are chosen in such a way that the natural frequency of the buoy should coincide with the dominant wave frequency of the prevailing energy spectrum of that area to maximize motion amplitude, and thus power production. The power captured by the system for different combinations of parameters will be determined through time-domain numerical modeling and simulation. Comparing the results of different simulations, the optimum draft-diameter combination with maximum power output per unit buoy weight will be selected. Afterward, using the obtained optimal value of the volume of displacement, surface area of the cylindrical buoy, principal dimensions of spherical and hexagonal buoys will be determined, and the power output of these buoy shapes will be determined through numerical simulations. Finally, comparing the power absorption efficiency of the selected buoy shapes, optimized buoy shape will be chosen. The following flowchart illustrates the steps of the shape optimization process followed in this study.

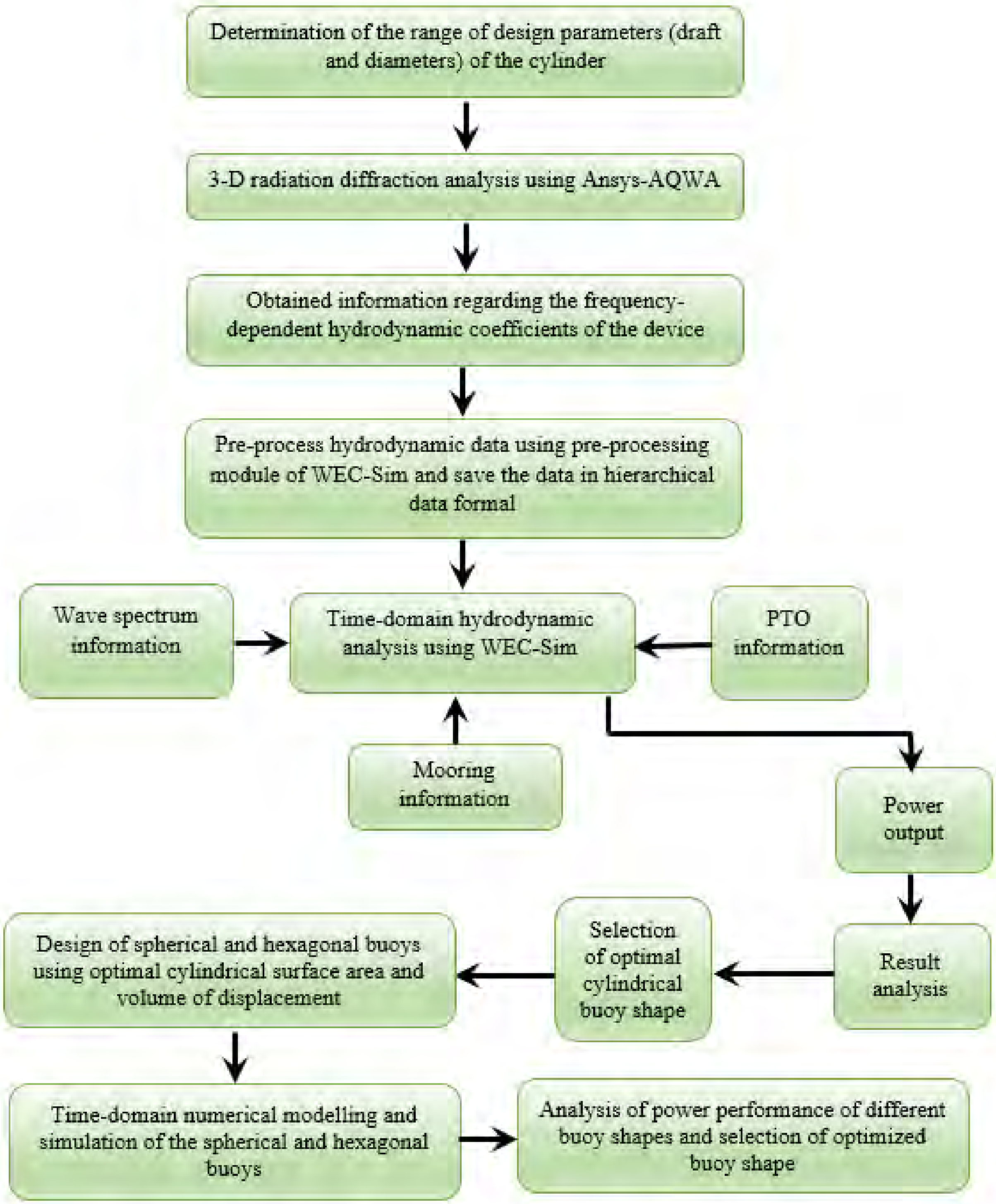

Figure 6.1 Flowchart of shape optimization process

These steps are illustrated in detail in the following subsections.

6.1 Selection of the range of buoy diameter and draft:

To select the range of buoy diameters and drafts, one important parameter is the range of prevailing wave energy periods of the intended energy deployment site. To obtain the range of feasible wave energy periods, the joint probability distribution diagram is generated based on the results of 4-year coupled wave-flow simulation, which is presented in the following table-

Table 6.1 Joint probability distribution of significant wave height and mean wave energy period

H_{sig}	Joint Probability Distribution (%)						
3.0-3.5						0.070	
2.5-3.0					0.328	0.470	
2.0-2.5				0.180	2.362	0.348	0.046
1.5-2.0			0.078	7.685	9.882	1.759	
1.0-1.5		0.020	6.344	25.701	7.650	0.052	0.006
0.5-1.0	0.122	11.492	14.049	3.195	0.023	0.012	0.015
0-0.5	2.771	4.910	0.139				
T_e	**1.0-2.0**	**2.0-3.0**	**3.0-4.0**	**4.0-5.0**	**5.0-6.0**	**6.0-7.0**	**7.0-8.0**

According to Table 6.1, the predominant energy period (T_e) is found in between 5.0 sec to 6.0 sec (percentage of occurrence = 36.8%). As energy period, T_e < 4.0 sec is practically infeasible for energy conversion, the range of feasible energy period is considered 4.0 sec to 7.0 sec for diameter and draft calculation.

Diameter range

Falnes (2003) mentioned that maximum energy absorption by a heaving axisymmetric buoy is equal to the wave energy transported by the incident wave front of width equal to the wavelength divided by 2π.

$$\therefore \text{ Capture width or absorbtion width, } L_{max} = \frac{L}{2\pi} \tag{6.1}$$

here, L = wavelength.

Moreover, Shadman et al. (2017) reported that non-dimensional relative capture width (C_{wr}) can be obtained by taking the ratio of capture width (C_{wr}) and device width (B), which must satisfy the following relationship for successful devices.

$$C_{wr} = \frac{L_{max}}{B} \geq 3 \tag{6.2}$$

For cylindrical buoy shape, the device width is the diameter of the cylinder (D).

$$\therefore \frac{L_{max}}{D} \geq 3$$

$$\Rightarrow \frac{L}{2\pi D} \geq 3$$

$$\Rightarrow L \geq 6\pi D$$

$$\Rightarrow D \leq \frac{L}{6\pi} \tag{6.3}$$

As the location in in intermediate water depth, the relationship between wave period and wavelength is as follows-

$$L = \frac{g}{2\pi} {T_e}^2 tanh(\frac{2\pi d}{L}) \tag{6.4}$$

For wave energy period $T_e = 4.0$ sec, $L = 23.826$ m (from equation 6.4), and using equation (6.3), corresponding buoy diameter is calculated as $D \leq 1.264$ m.

For wave energy period $T_e = 7.0$ sec, $L = 52.72$ m, and $D \leq 2.80$ m.

So, the range of diameter is selected 1.20 m to 2.80 m for optimization.

Draft range

After obtaining the upper limit and lower limit of buoy diameter, the following design parameter is the draft of the cylindrical buoy. As mentioned earlier, to maximize the system′s power generation performance, the natural frequency or natural period of the buoy must synchronize with the dominant wave frequency or wave period. Not only that, the buoy must capture wave energy efficiently for other wave periods too. Considering one degree of freedom of the system (only heave), the equation of buoy heave natural frequency is expressed as follows-

$$\omega_n = \sqrt{\frac{\rho g A_{WP}}{M_{33} + A_{33}}} \tag{6.5}$$

Here, A_{WP} = water plane area of the buoy = $\frac{1}{4}\pi D^2$,

M_{33} = mass of the buoy based on the submerged volume = $\rho \frac{1}{4}\pi D^2 T$,

T = Draft of the buoy,

A_{33} = Added mass coefficient. At preliminary stage of calculation, it can be calculated using the following formula (Shadman et al., 2017) -

$$A_{33} = 0.167\, \rho D^3 \tag{6.6}$$

Therefore, equation (6.5) becomes-

$$\omega_n = \sqrt{\frac{\rho g A_{WP}}{\rho \frac{1}{4}\pi D^2 T + 0.167\, \rho D^3}} \tag{6.7}$$

Using the range of buoy diameter (1.20 m to 2.80 m) and range of prevailing wave energy period (4.0 sec to 7.0 sec), equation (6.7) is solved for different combinations of wave energy period and buoy diameter, assuming that the buoy achieves resonance with the specified energy period (i.e., $\omega_n = \frac{2\pi}{T_e}$). Thus, a set of values of buoy draft is obtained by solving equation (6.7) which is presented in Table (6.2). The corresponding mass of each buoy is shown in Table (6.3).

As shown in Table 6.2, there are 119 draft-diameter combinations available for optimization purpose. Each combination satisfies the buoy resonance condition for a given wave energy period. However, there are too many draft-diameter combinations to simulate them all and compare. Thus, some additional considerations are taken into account to decrease the number of individual simulations.

Shadman et al. (2017) reported that the response of a point absorber in the resonance region is dominated by damping. The amplitude of motion and thus power absorption will be large if damping is small. In the low-frequency region (higher wave energy periods and longer wavelengths), the response is dominated by restoring. As the ratio of wavelength and buoy diameter (i.e., horizontal dimension) is high, it will follow the waves upwards and downwards. In the high-frequency region (smaller wave energy periods and small wavelengths), the response is dominated by mass. There will be several wave crests and troughs within the horizontal length of the buoy, and thus wave loss their influence on buoy behavior.

According to the aforementioned statements, undoubtedly, to design a heaving buoy that will capture wave energy from a wide range of energy periods efficiently, the resonance period of the buoy should be equal to the lower energy period. Thus, it will capture adequate energy from shorter wavelengths and follows the waves with longer wavelengths.

The percentage occurrence of wave energy period within the range of 4.0 s to 5.0 s is almost 36.8%, as presented in Table 6.1. Hence, the combinations within natural heave period 4.0 s to 5 s ($1.2 \leq D \leq 2.8$ and $2.0 \leq T_e \leq 3.2$) are selected in this study for analysis.

Table 6.2 Draft-diameter combinations of different buoys with different resonant period

***Te* (sec)**	**1.2**	**1.3**	**1.4**	**1.5**	**1.6**	**1.7**	**1.8**	**1.9**	**2.0**	**2.1**	**2.2**	**2.3**	**2.4**	**2.5**	**2.6**	**2.7**	**2.8**	**Dia (m)**
4.0	2.4	2.3	2.3	2.3	2.3	2.3	2.2	2.2	2.2	2.2	2.1	2.1	2.1	2.1	2.1	2.0	2.0	**Buoy draft in meter**
4.5	2.7	2.7	2.7	2.7	2.7	2.6	2.6	2.6	2.6	2.5	2.5	2.5	2.5	2.5	2.4	2.4	2.4	
5.0	3.2	3.2	3.2	3.2	3.2	3.1	3.1	3.1	3.1	3.0	3.0	3.0	3.0	3.0	2.9	2.9	2.9	
5.5	3.9	3.8	3.8	3.8	3.8	3.8	3.7	3.7	3.7	3.7	3.6	3.6	3.6	3.6	3.6	3.5	3.5	
6.0	4.6	4.6	4.6	4.5	4.5	4.5	4.5	4.5	4.4	4.4	4.4	4.4	4.4	4.3	4.3	4.3	4.3	
6.5	5.5	5.5	5.4	5.4	5.4	5.4	5.4	5.3	5.3	5.3	5.3	5.2	5.2	5.2	5.2	5.2	5.1	
7.0	6.5	6.5	6.4	6.4	6.4	6.4	6.3	6.3	6.3	6.3	6.3	6.2	6.2	6.2	6.2	6.2	6.1	

Table 6.3 Mass in tonnes of different cylindrical buoys

***Te* (sec)**	**1.2**	**1.3**	**1.4**	**1.5**	**1.6**	**1.7**	**1.8**	**1.9**	**2.0**	**2.1**	**2.2**	**2.3**	**2.4**	**2.5**	**2.6**	**2.7**	**2.8**	**Dia (m)**
4.0	2.7	3.2	3.7	4.2	4.7	5.2	5.8	6.4	7.1	7.7	8.4	9.1	9.8	10.5	11.2	12.0	12.7	**Mass in Tonnes**
4.5	3.2	3.7	4.2	4.8	5.5	6.1	6.8	7.5	8.3	9.0	9.8	10.7	11.5	12.4	13.3	14.2	15.1	
5.0	3.8	4.4	5.0	5.7	6.5	7.3	8.1	9.0	9.9	10.8	11.8	12.8	13.8	14.9	16.0	17.1	18.3	
5.5	4.5	5.2	6.0	6.9	7.8	8.7	9.7	10.8	11.9	13.0	14.2	15.4	16.7	18.0	19.4	20.8	22.2	
6.0	5.3	6.2	7.2	8.2	9.3	10.5	11.7	13.0	14.3	15.7	17.1	18.6	20.2	21.8	23.5	25.2	26.9	
6.5	6.4	7.4	8.6	9.8	11.1	12.5	14.0	15.5	17.1	18.8	20.5	22.3	24.2	26.2	28.2	30.3	32.4	
7.0	7.5	8.8	10.2	11.6	13.2	14.8	16.6	18.4	20.3	22.3	24.4	26.6	28.9	31.2	33.6	36.1	38.7	

6.2 Model Development and Analysis Set-up

After finalizing the cylindrical buoy's design parameters (draft, diameter) to optimize, the next step is to create a computer model representation of the buoy. To design a hollow cylindrical buoy, apart from diameter and draft, two other parameters are necessary – height and thickness of the cylinder. For all diameters, the height above the mean water surface is chosen as 0.50 m.

Detailed properties of the first buoy geometry are listed in Table 6.4. The representation of the geometry of the buoy is created using the 3D modelling software- Rhinoceros, which is illustrated in Figure 6.2.

Table 6.4 Mass properties of cylindrical buoy

Detail Properties of Cylindrical Buoy	
Diameter	1.200 m
Draft	2.360 m
Volume of displacement	2.669 m^3
Mass of displaced water	2735.831 kg
Height	2.860 m
Surface area of the underwater part	10.028 m^2
Surface area of the above water part	3.016 m^2

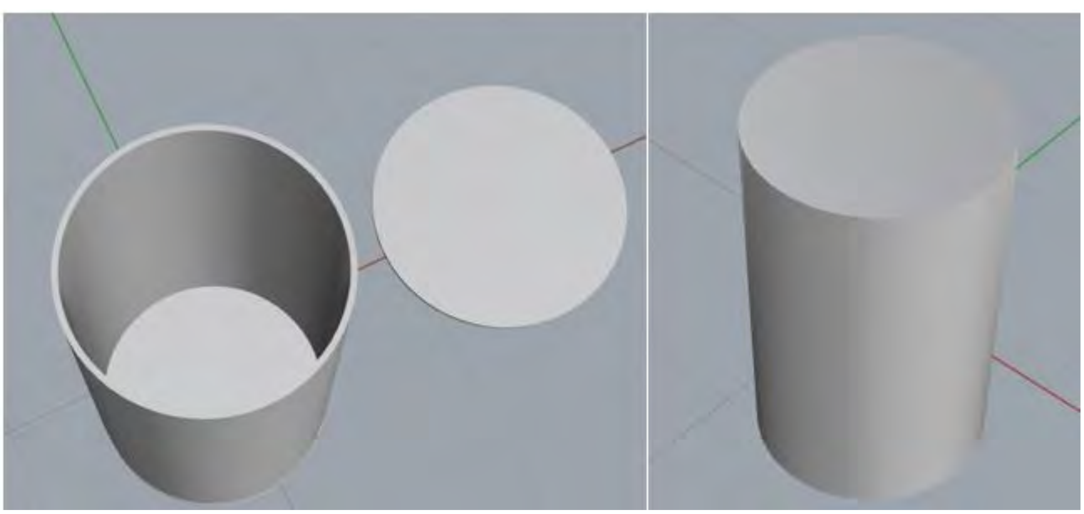

Figure 6.2 Model of cylindrical buoy

6.2.1 3-D diffraction and radiation analysis using Ansys-AQWA

To compute excitation force, added mass matrix, damping matrix, and hydrostatic coefficient of the body, the solid model is imported to the 'DesignModeler' software under Ansys Workbench. Here, the buoy is divided into two parts- the underwater part (which represents the wetted surface of the buoy) and the above water part (which represents the buoy surface above the mean water surface), as shown in Figure 6.3.

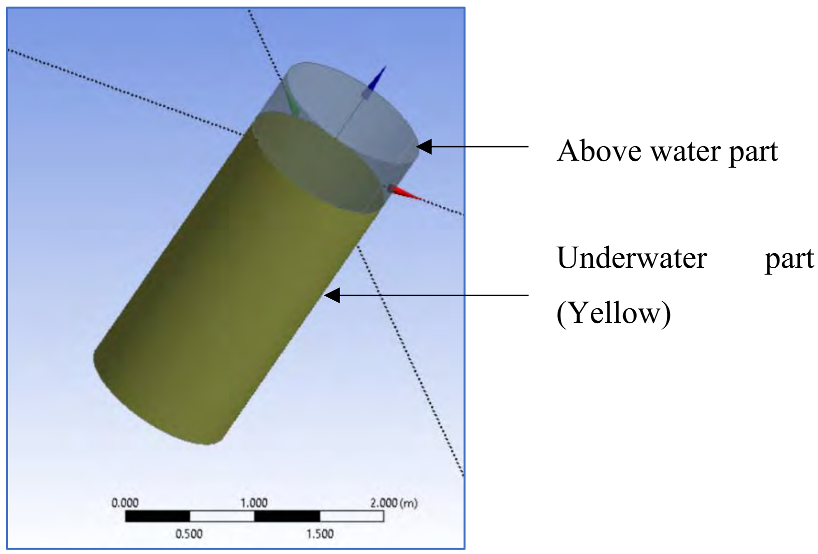

Figure 6.3 AQWA model

Afterward, the hydrodynamics analysis system is opened in AQWA workbench, and geometry is automatically attached by AQWA Editor. The density of water and water depth are considered 1025 kg/m^3 and 7.1 m, respectively. The size of the numerical water tank is set as 20.0 m in X-direction and 10.0 m in Y-direction. Mass properties of the buoy (total mass, X, Y, and Z positions of center of gravity, inertia values) are defined using the point mass approach. After specifying the properties of the body, the next step of diffraction radiation analysis is to generate mesh. To generate mesh, two parameters need to be defined. One is defeaturing tolerance, which controls how small details are treated by the mesh. If the detail is smaller than this tolerance, then a single element may span over it, otherwise, the mesh size will be reduced in this area to ensure that the feature is meshed. Another one is maximum element size, which controls the maximum size of the elements that will be generated. Relationship between defeaturing tolerance and maximum element size is as follows-

Defeaturing tolerance ≤ 0.6 x maximum element size

Although the smaller mesh size is recommended for better accuracy of the simulation results, considering the limitations of the AQWA solver (maximum no. of elements = 18,000), in this study, maximum element size and defeaturing tolerance are chosen as 0.05 m and 0.01 m, respectively. The surface is represented by sufficient numbers of quadrilateral panels (Figure 6.4).

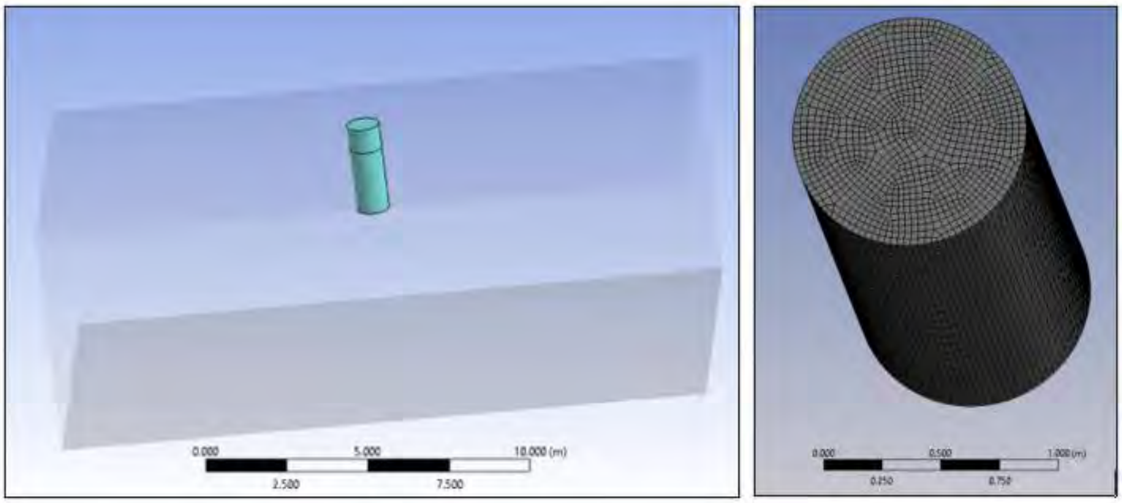

Figure 6.4 Numerical wave tank and 3D mesh geometry of the buoy

In the next step, the ocean environment parameters, such as no. of wave frequencies, wave directions are specified. To obtain more detailed results, frequency range is selected between 0.08333 Hz to 1 Hz with an interval frequency of 0.04167 Hz. As the device is symmetric about the Z-axis, wave direction is not an important criterion to be considered. However, adding multiple incident wave angles don′t increase simulation time. Thus, the results are obtained for direction range in between -180^0 to $+180^0$ with 45^0 intervals. Under the analysis settings option, element properties and ASCII hydrodynamic database options are enabled so that the output results, i.e., added mass matrix, damping matrix, RAO, Froude-Krylov forces, etc., are stored in separate files with extensions '.LIS′ and '.AH1′. Sample output files of the AQWA analysis are presented in Appendix A.

For any floating structure, it is important to check whether it is stable or not. To be stable, the center of gravity (G) of the structure must be below the metacentre (M), thus restoring moment will be positive, and it will tend to return to its initial position. Metacentre is the point at which verticals through the centres of buoyancy (B, B_1) at two consecutive angles of heel intersect (Figure 6.5).

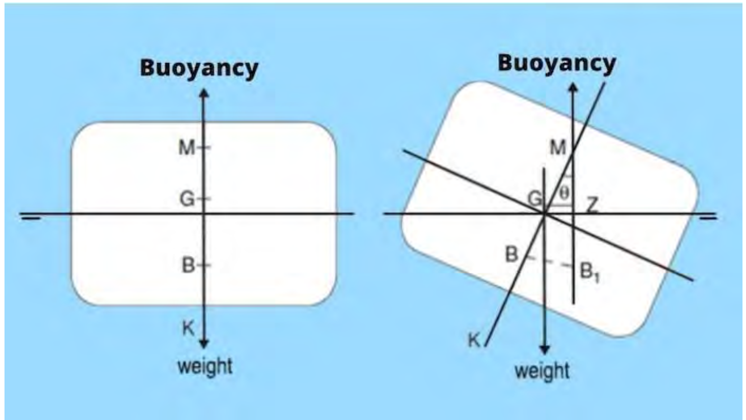

Figure 6.5 Stable equilibrium condition of floating structure

From the simulation results, the following values of the above-mentioned parameters are obtained-

Vertical position of centre of gravity measured from bottom (KG)	1.43 m
Vertical position of centre of buoyancy measured from bottom (KB)	1.18 m
BG = KG – KB	0.25 m
Metacentric height, GM	0.213 m
Restoring moment	97.12 $Nm/^0$

Therefore, positive restoring moment implies that the structure is in stable equilibrium condition.

After obtaining hydrodynamic coefficients using BEM solver (Ansys-AQWA), the next part is to select a suitable mooring configuration for the device.

6.2.2 Mooring system design

To design suitable catenary mooring configurations, at first, all possible environmental loads acting on the buoy need to be evaluated. These forces include:

i. Wind force,
ii. Current force, and

iii. Wave force

Wind force calculation: Wind force acting on the cylindrical buoy can be calculated using the following formula-

$$F_{wind} = \frac{1}{2} C\, A\, \rho\, U^2 \tag{6.8}$$

Here, U = air velocity at the height of the center of the exposed body, which is considered 20 m/s for this study,

ρ = density of air = 1.226 kg/m^3,

A = cross sectional area projected transverse the flow direction = Diameter of buoy (D) x height of the above water surface of the buoy (h_b) = (1.2 x 0.5) m^2 = 0.6 m^2,

C = shape coefficient.

To determine shape coefficient, at first, the value of Reynolds no. is determined.

$$R_e = \frac{UD}{\vartheta_a} = \frac{20 \times 1.2}{1.45 \times 10^{-5}} = 1.7 \times 10^6 \tag{6.9}$$

Here, ϑ_a = kinematic viscosity of air = 1.45×10^{-5} m^2/s.

Considering highly corroded steel plate, the value of surface roughness is obtained from DNV-RP-C205.

$$K = 3 \times 10^{-3}$$

$$\therefore \text{Relative roughness,} \frac{K}{D} = 2.5 \times 10^{-3}$$

Using the value of R_e and $\frac{K}{D}$, the value of shape coefficient is obtained using Figure 6.6.

$$C = 0.92$$

$$\therefore F_{wind} = \frac{1}{2} \times 0.92 \times 0.6 \times 1.2 \times 1.226 \times 20^2 = 0.162 \text{ KN}$$

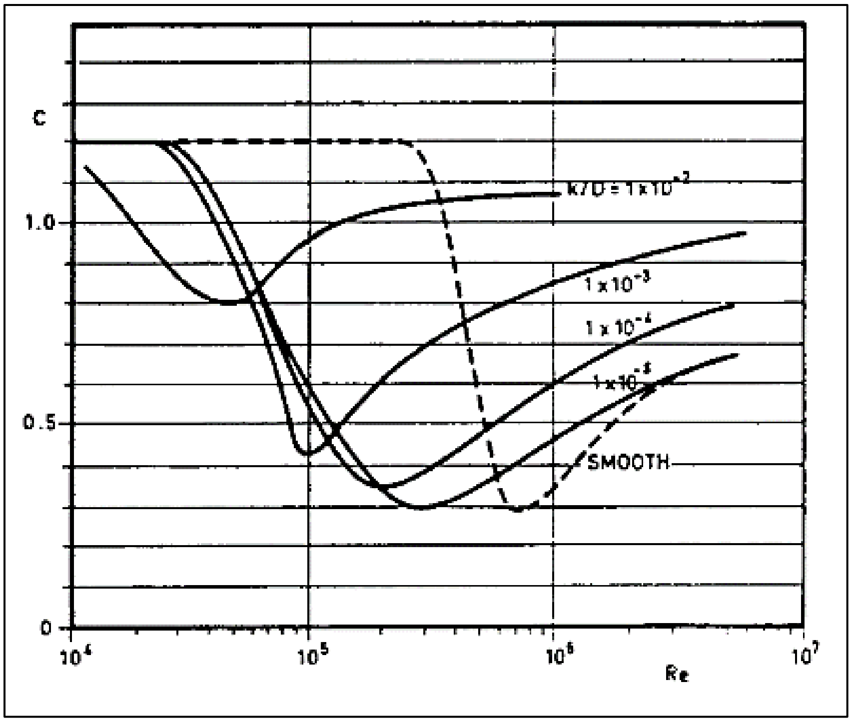

Figure 6.6 Drag coefficient for fixed circular cylinder for steady flow in critical flow regime, for various roughnesses (Source: DNV-RP-C205)

Current force calculation:

Current force is calculated using the following formula-

$$F_{current} = \frac{1}{2} C_d \, A \, \rho_w \, {U_c}^2 \tag{6.10}$$

In the intended energy deployment site, current speed, U_c is considered 4 knots or 2.06 m/s.

To calculate drag coefficient, C_d using Figure (6.6), Reynolds number of water flow and ration of surface roughness and diameter are calculated.

$$R_e = \frac{U_c D}{\vartheta_w} = \frac{2.06 \times 1.2}{0.95 \times 10^{-6}} = 2.6 \times 10^6$$

Again, the value of drag coefficient, C_d is found 0.92 for a relative roughness of 2.5×10^{-3}.

$$\therefore F_{current} = \frac{1}{2} \times 0.92 \times 0.6 \times 1.2 \times 1025 \times 2.06^2 = 1.441 \text{ KN}$$

Wave drift force: In comparison to global wave energy resources, the sea states in the operational region consist of shorter wavelengths and smaller wave heights (average wavelength = 27.5 m and average wave height = 1.164 m). Thus, the value of wave drift force will be very small compared to the wind and current forces and is neglected in this preliminary design stage.

Therefore, considering 50% safety factor, the value of total environmental load will be-

Total environmental load = $1.5 \times (0.162 + 1.441)$ KN $= 2.405$ KN = 0.25 tonnesf

Total load = Weight of the buoy + Total environmental load = (2.70 + 0.25) = 2.95 tonnesf

Catenary mooring line shape design:

There will be two catenaries on the two sides of the buoy. In the present calculation, the following values of input parameters are considered-

- water depth plus the distance between sea-level and the fairlead, d = 8.6 m (considering high tide condition),
- force applied to the mooring line at the fairlead, F = 1.475 tonnes,
- normalized thread diameter, d_T = 25 mm, and
- submerged density of steel material, ρ = 7.85 tonnes/m^3
- no. of nodes = 10

Therefore, using equation (4.1) - (4.5), the following values of catenary shape parameters are estimated-

Horizontal distance between the fairlead and the touchdown point of the mooring line on the seabed, X	80.07 m
Weight of the suspended chain, v	0.3 tonnes
Cross sectional area of the thread, A	4.9x10^{-4} m^2
Unit weight of the mooring line in water, w	3.85x10^{-3} tonnes/m
Normalized horizontal tension component, T_0	1.04 tonnes
Catenary shape parameter, b	0.03638
Length of the suspended mooring line, S	80.68 m

The coordinates (x, y) of each node are listed in Table 6.5 and the shape of the catenary mooring line is shown in Figure 6.7.

Table 6.5 Horizontal and vertical coordinates of different nodes

Node no.	Horizontal (x) value	Vertical (y) value
0	0	0
1	8.007	0.086
2	16.014	0.344
3	24.021	0.774
4	32.029	1.376
5	40.036	2.15
6	48.043	3.096
7	56.05	4.214
8	64.057	5.504
9	72.064	6.966
10	80.071	8.6

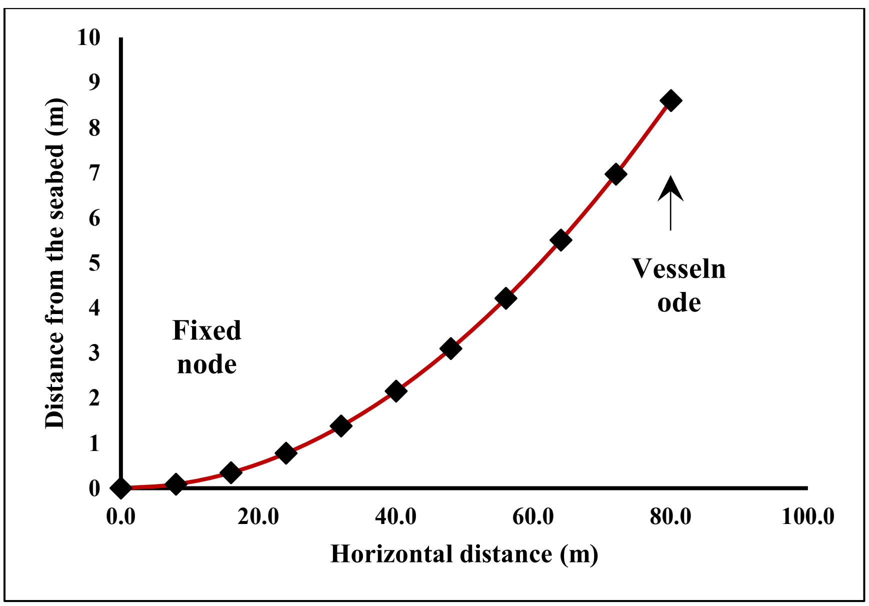

Figure 6.7 Catenary mooring line shape

6.2.3 Pre-processing of hydrodynamic data in WEC-Sim

After calculating hydrodynamic coefficients using Ansys-AQWA and mooring line shape parameters, the next step is to generate a HDF5 file that will store all nondimensionalized hydrodynamic coefficients. To do so, a 'Boundary Element Method Input/Output (BEMIO)′ code is run to convert hydrodynamic coefficient data (stored in files with .AH1 and .LIS extensions) into the HDF5 (.h5) file format. After running BEMIO code the following curves are generated-

1. **Radiation wave damping coefficient:** Figure 6.8 illustrates the nondimensionalized radiation wave damping coefficient values, $\overline{B_{33}}(\omega)$ for different wave frequencies. The values of normalized radiation damping coefficient, $\overline{B_{33}}(\omega)$ are determined by using the following equation-

   $$\overline{B_{33}}(\omega) = \frac{B_{33}(\omega)}{\rho\omega} \tag{6.11}$$

   where, ρ is the density of sea water, ω is the wave frequency in rad/s, and $B_{33}(\omega)$ is the radiation damping coefficient obtained from BEM solver.

   In general, for any floating body, the value of radiation damping coefficient becomes zero at $\omega = 0,$ and $\omega = \infty$. As shown in Figure (6.8), the value of $\overline{B_{33}}(\omega)$ decreases with increasing wave frequency (i.e., decreasing wave energy period) and becomes zero at $\omega \geq 4$ rad/s. At resonance period, T_e = 4 s, the value of $\overline{B_{33}}(\omega) = 0.04$.

2. **Added mass coefficient:** The values of normalized added mass coefficient for different wave frequencies are illustrated in Figure 6.9. WEC-Sim code scales added mass coefficient, $A_{33}(\omega)$ using the following formula-

   $$\overline{A_{33}}(\omega) = \frac{A_{33}(\omega)}{\rho} \tag{6.12}$$

   As shown in Fig. (6.9), within the specified frequency range ($0.52 \leq \omega \leq 6.3$), the value of normalized added mass coefficient decreases with increasing frequency, becomes minimum at ω = 2.3 rad/s, and then gradually increases with increasing frequency. At resonance period, T_e = 4 s, the value of $\overline{A_{33}}(\omega)$, is 0.43.

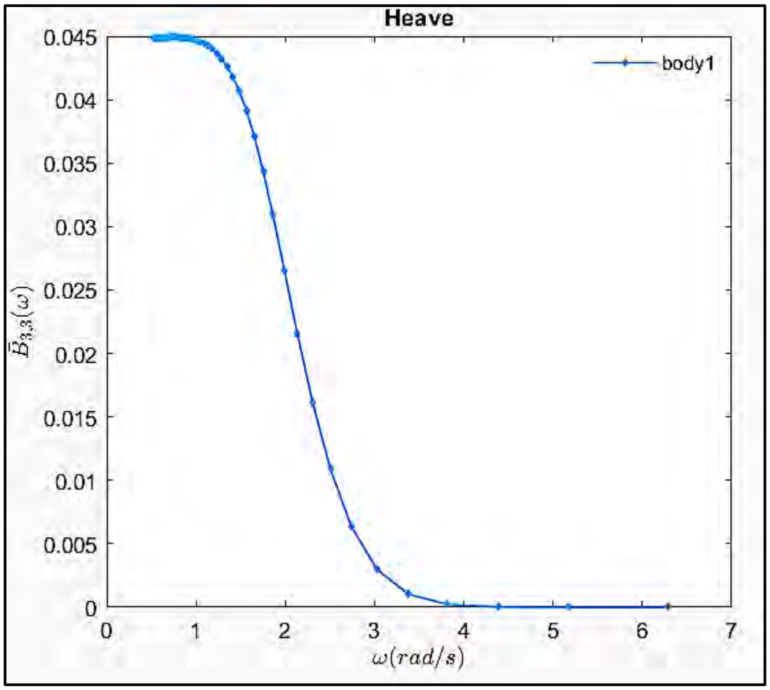

Figure 6.8 Normalized radiation damping coefficient for heave motion

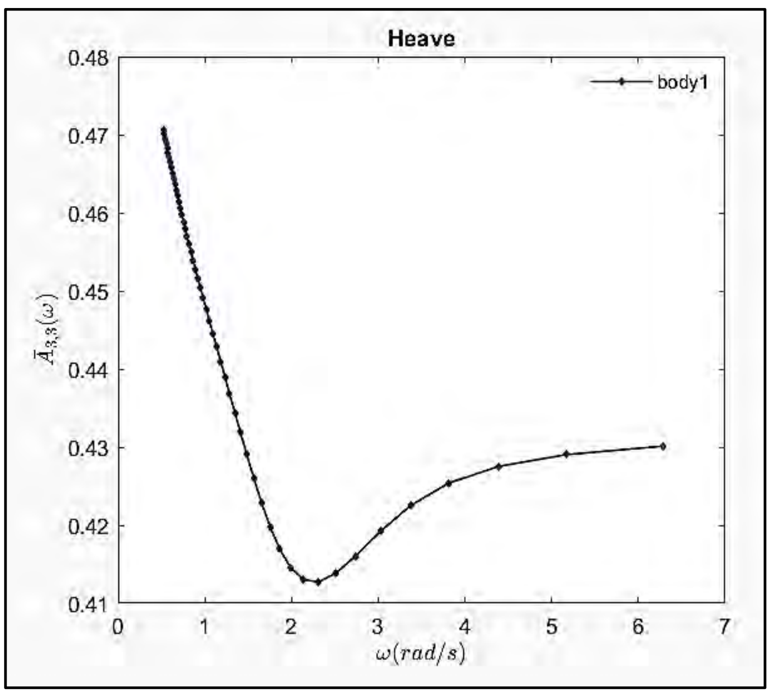

Figure 6.9 Normalized added mass coefficient for heave motion

3. **Wave-excitation force:** Magnitudes of normalized excitation force, $\overline{X_3}(\omega, \beta)$ for head sea condition ($\beta = 180°$) are shown in Figure 6.10. Here,

$$\overline{X_3}(\omega,\beta) = \frac{X_3(\omega,\beta)}{\rho g} \quad (6.13)$$

where, $X_3(\omega,\beta)$ is the magnitude of excitation force for heave motion obtained from BEM solver. $\overline{X_3}(\omega,\beta)$ decrease with increasing frequency and becomes zero for $\omega \geq 4.39\ \mathrm{rad/s}$. At resonance period, the magnitude of normalized excitation force is 0.58.

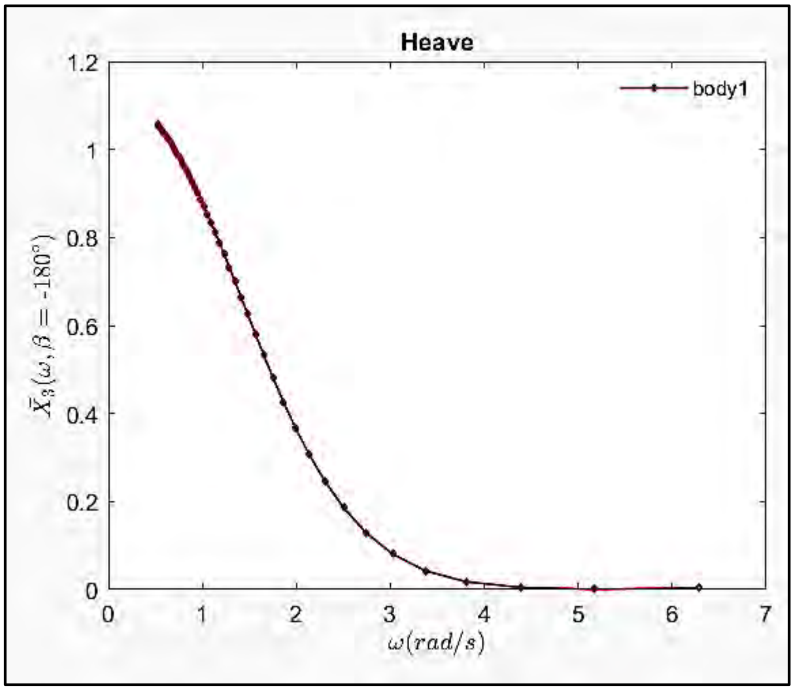

Figure 6.10 Wave excitation force

4. **Normalized IRF of radiation and excitation forces:** Values of normalized radiation impulse response function, $\overline{K_{33}}\ (t)$ and normalized excitation impulse response function, $\overline{K_3}\ (t,\beta)$ for heave motion are shown in Figure 6.11 and Figure 6.12.

   Here,

$$\overline{K_{33}}\ (t) = \frac{2}{\pi}\int_0^{\infty}\frac{B_{33}(\omega)}{\rho}cos(\omega t)d\omega, and \quad (6.14)$$

$$\overline{K_3}\ (t,\beta) = \frac{1}{2\pi}\int_{-\infty}^{+\infty}\frac{X_3(\omega,\beta)e^{i\omega t}}{\rho g}d\omega \quad (6.15)$$

   For solution convergence, both $\overline{K_{33}}\ (t)$ and $\overline{K_3}\ (t,\beta)$ should tend to zero within specified time range.

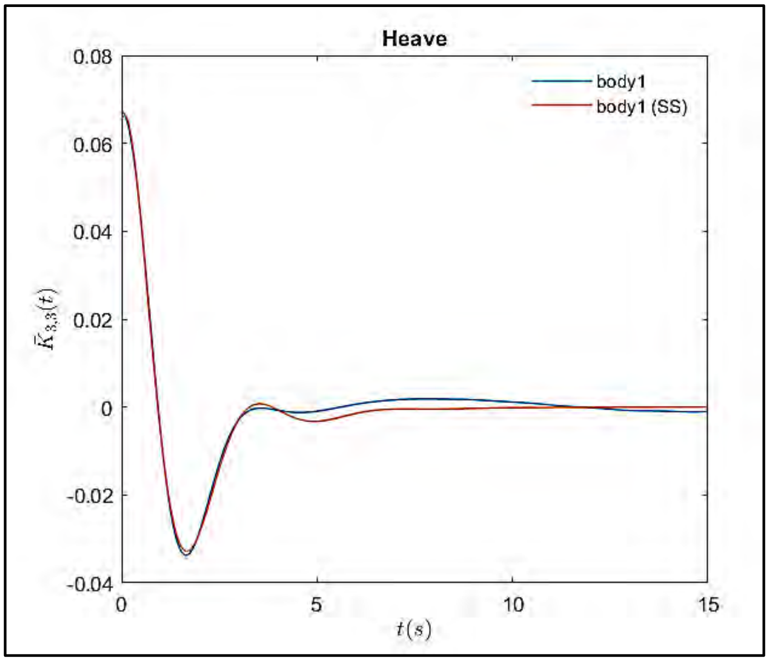

Figure 6.11 Radiation IRF

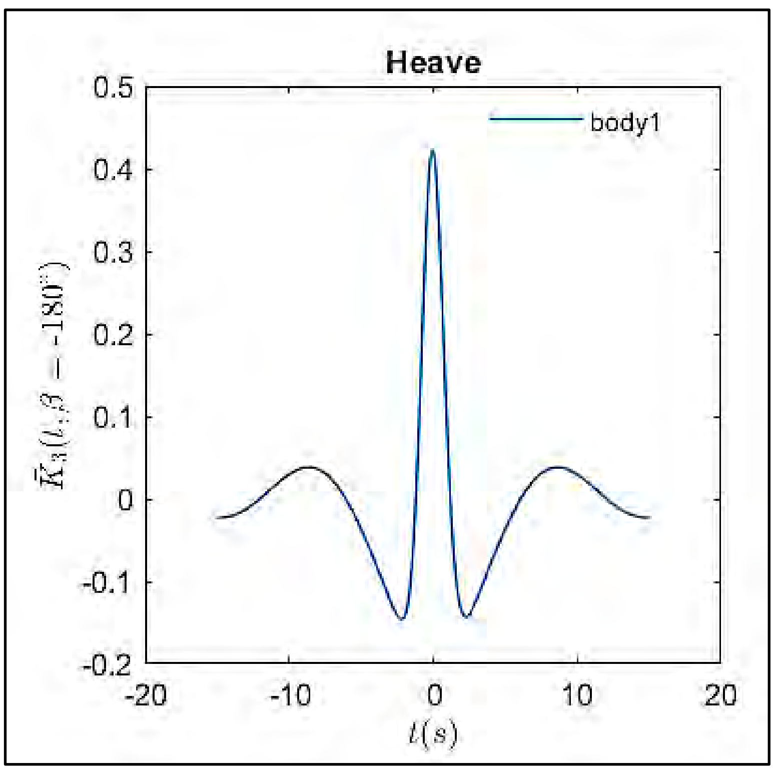

Figure 6.12 Excitation IRF

6.2.4 Wave spectrum of different months

To better assess the average power production by the designed WEC, the time-domain simulations are executed separately for different months. For that, wave energy spectrum input files are generated for different months based on the results of coupled flow-wave simulations (Chapter 2). The energy spectrums for different months are illustrated in Figure 6.13.

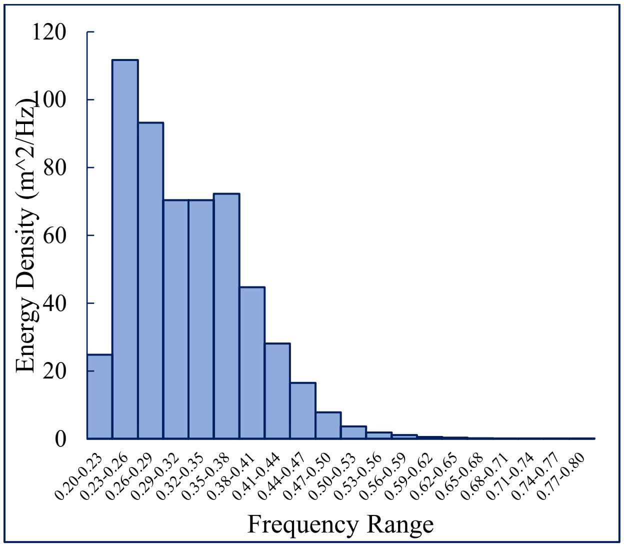

(a) January

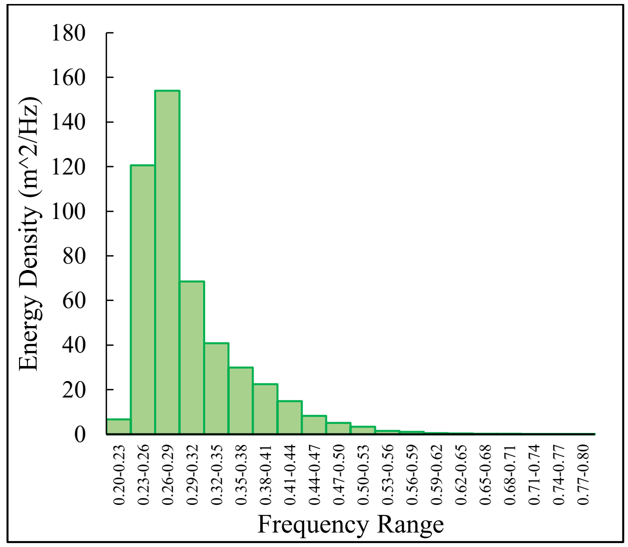

(b) February

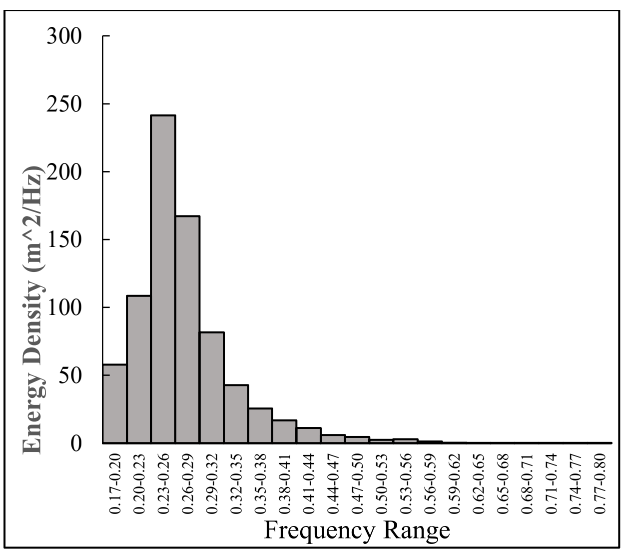

(c) March

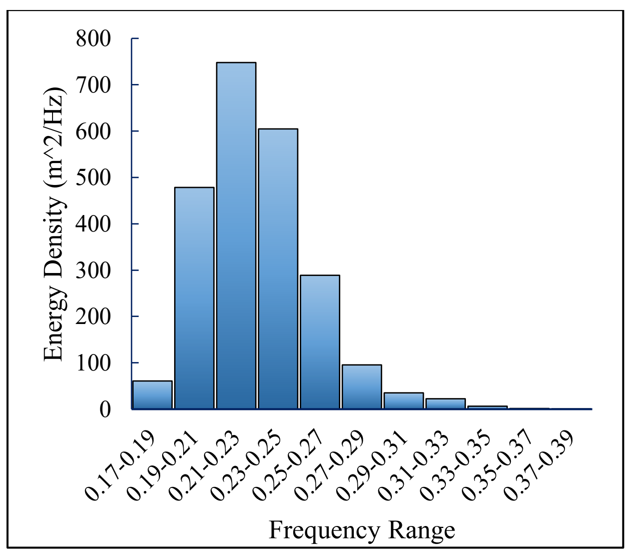

(d) April

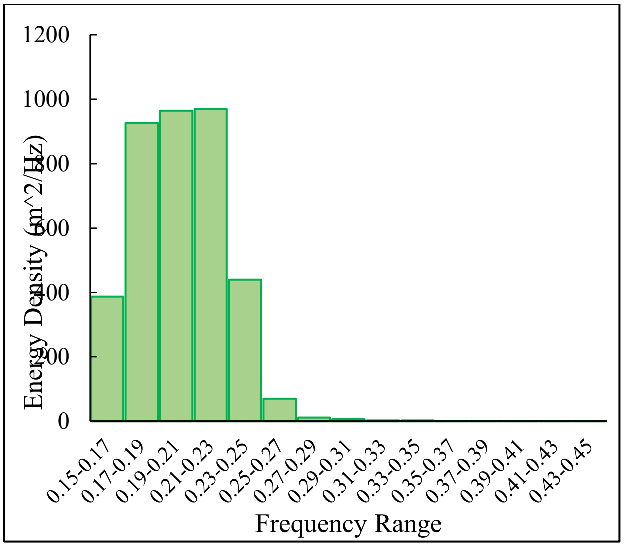

(e) May

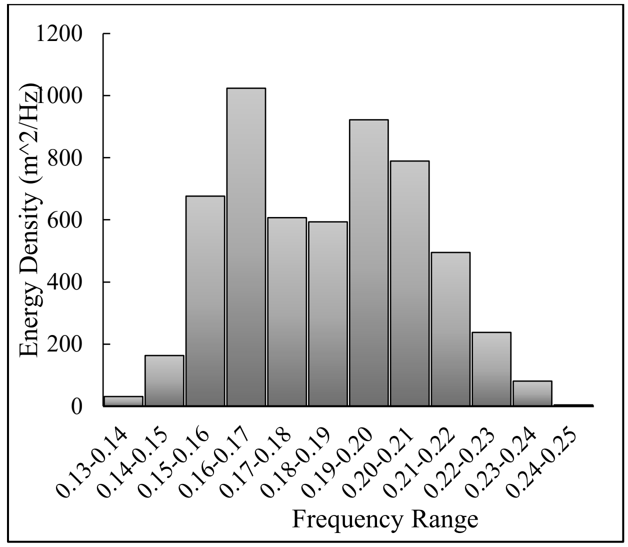

(f) June

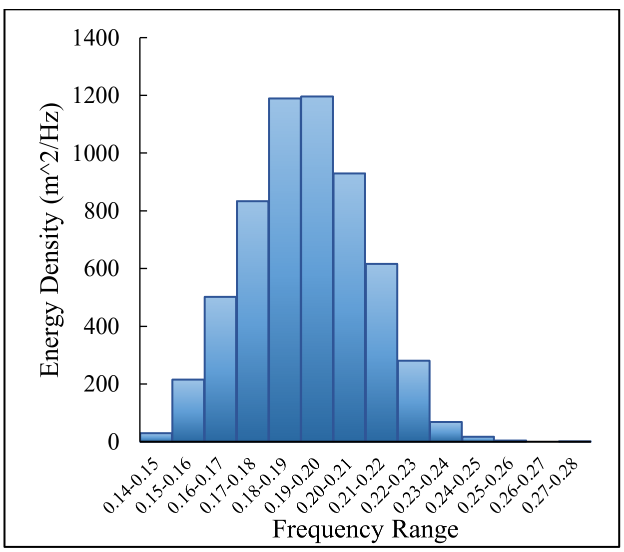

(g) July

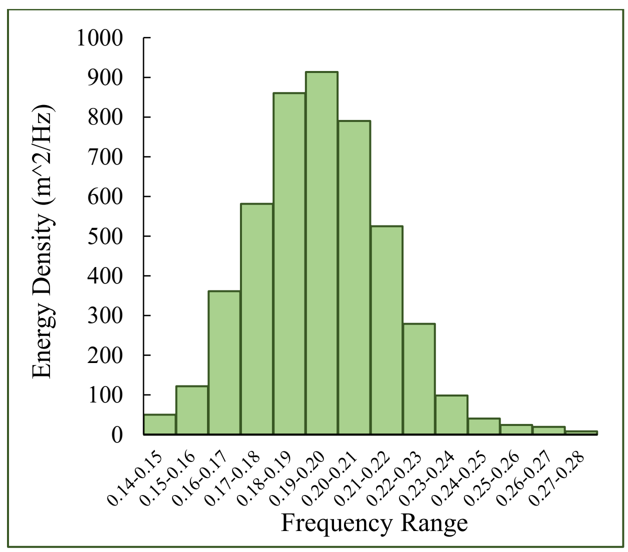

(h) August

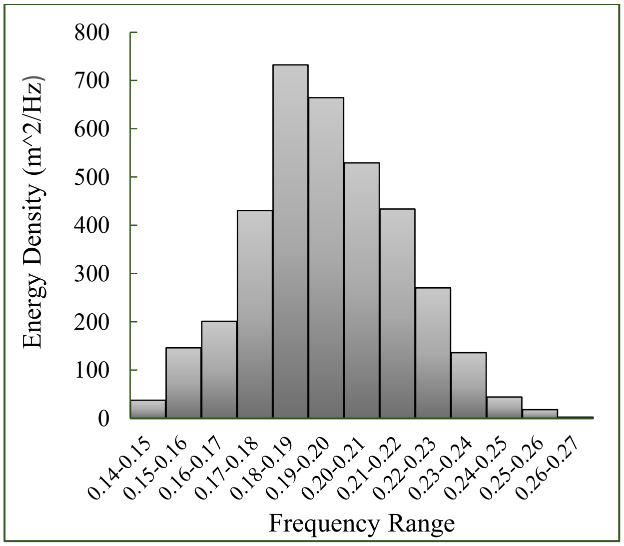

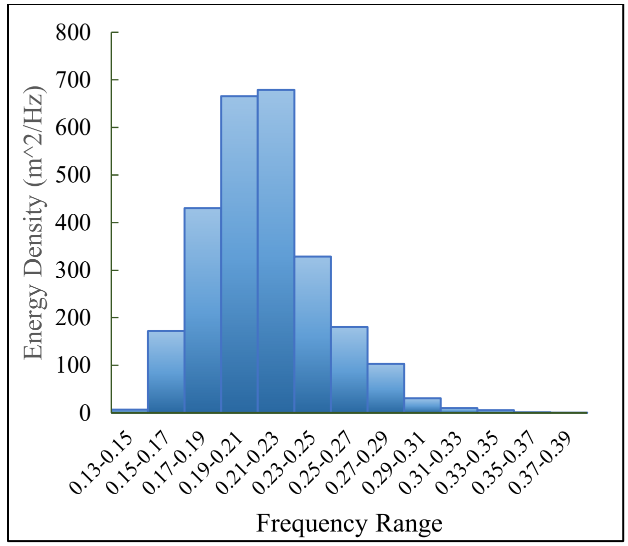

(i) September

(j) October

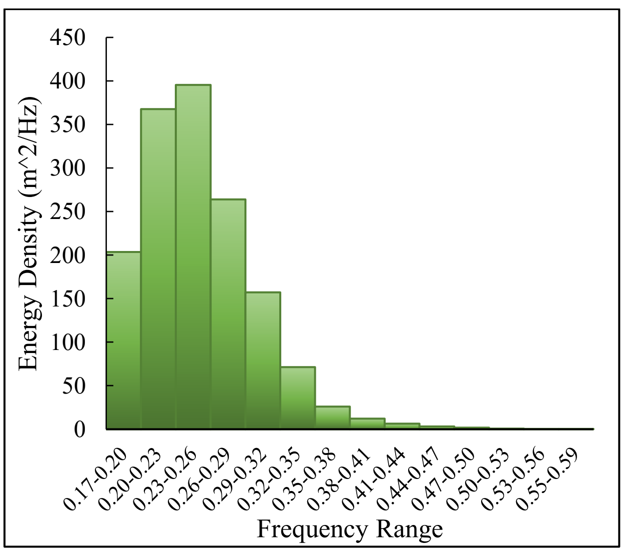

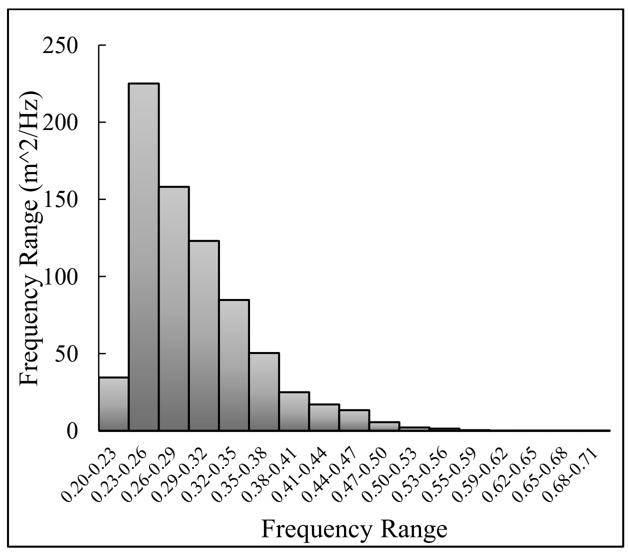

(k) November

(l) December

Figure 6.13 Wave spectrum of different months

6.2.5 Viscous damping coefficient calculation

As mentioned earlier, the hydrodynamic coefficients obtained from the linear potential flow boundary element solver based on the assumptions that the flow is inviscid, incompressible, and irrotational. However, to accurately predict the device performance, viscosity effects need to be included as all real fluids are viscous. In WEC-Sim code, the effect of viscous drag force can be included by specifying the value of quadratic drag coefficient, C_D. The quadratic viscous damping force is calculated by using the following formula-

$$F_v = -\frac{C_D \rho A_d}{2} \dot{X}|\dot{X}| \tag{6.16}$$

where, A_d = characteristic area for drag calculation, $\dot{X}$ = relative velocity between the body and the flow around it. To obtain the value of drag coefficient for smooth cylinder using the following figure, at first, the average value of Reynold′s number of the fluid flow have been calculated.

For mean velocity, $v = 6.37\ \text{m/s}$, Reynold′s number, $R_e = 8.6 \times 10^6$

$$\therefore C_D = 0.82\ [\text{Figure (6.13)}]$$

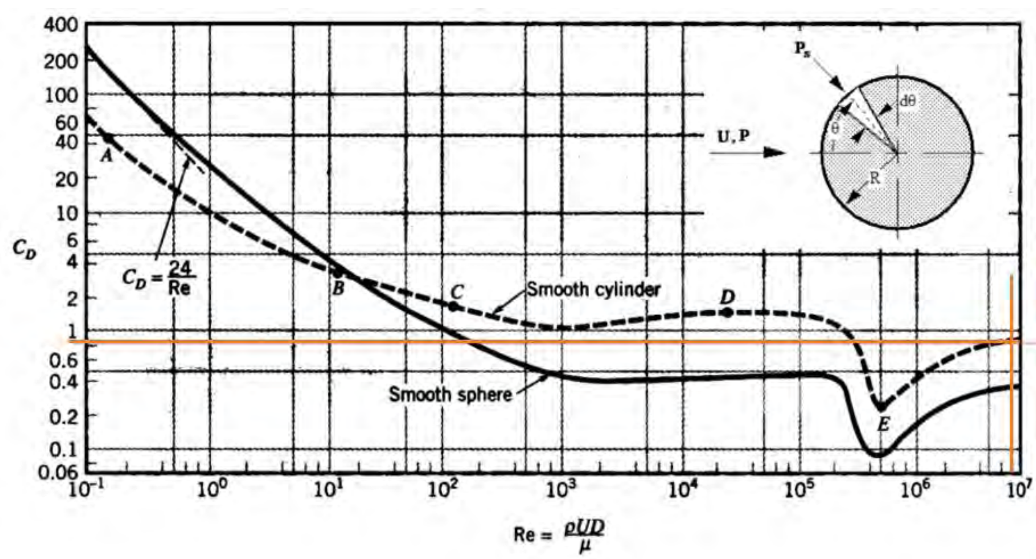

Figure 6.14 Drag coefficient as a function of Reynolds no. (Source: Gao, 2018)

6.2.6 PTO Specifications

In the present study, linear power take-off system has been used, in which the PTO mechanism is represented by a linear spring-damper system. Shadman et al. (2017) mentioned that for maximum energy capture from the waves, the damping of the PTO must be equal to the radiation damping of the point absorber. Thus, in the following formula of reaction force due to linear PTO system, the value of damping of the PTO, C_{PTO} is considered equal to the radiation damping coefficient at resonance period for all geometries of the WECs. Also, stiffness of the PTO is considered zero as the average contribution of the spring to the total power is zero over a wave energy period because it refers to the energy that flows back and forth between the captor (kinetic energy) and the PTO spring (elastic potential energy) (Folley, 2016).

$$F_{PTO} = -K_{PTO} X_{rel} - C_{PTO} V_{rel} \quad (6.17)$$

where, X_{rel} and V_{rel} *ar*e the relative displacement and velocity between the buoy and PTO body.

After finalizing all input parameters (i.e., frequency-dependent hydrodynamic coefficients, device geometry and mass properties, wave information, and information regarding the PTO system), WEC-Sim code is used to model the whole system. Afterward, simulation has been run by using user-specified wave spectrum for different months. In the next section, the power output of the model has been presented and discussed.

CHAPTER 7

RESULTS AND DISCUSSION

After finalizing all input parameters such as wave spectrum, all dimensions and mass properties of the buoy, hydrodynamic data, specifications of mooring, and power take-off systems, a Simulink model is built using the WEC-Sim library. The model is shown in Figure 7.1. Rigid body block indicates the float, which is connected to the Translational PTO system- this constrains the float to move only in the vertical direction. Global reference frame acts as seabed. Afterward, simulation parameters, body properties, wave properties, PTO parameters, and mooring are defined in the WEC-Sim input file.

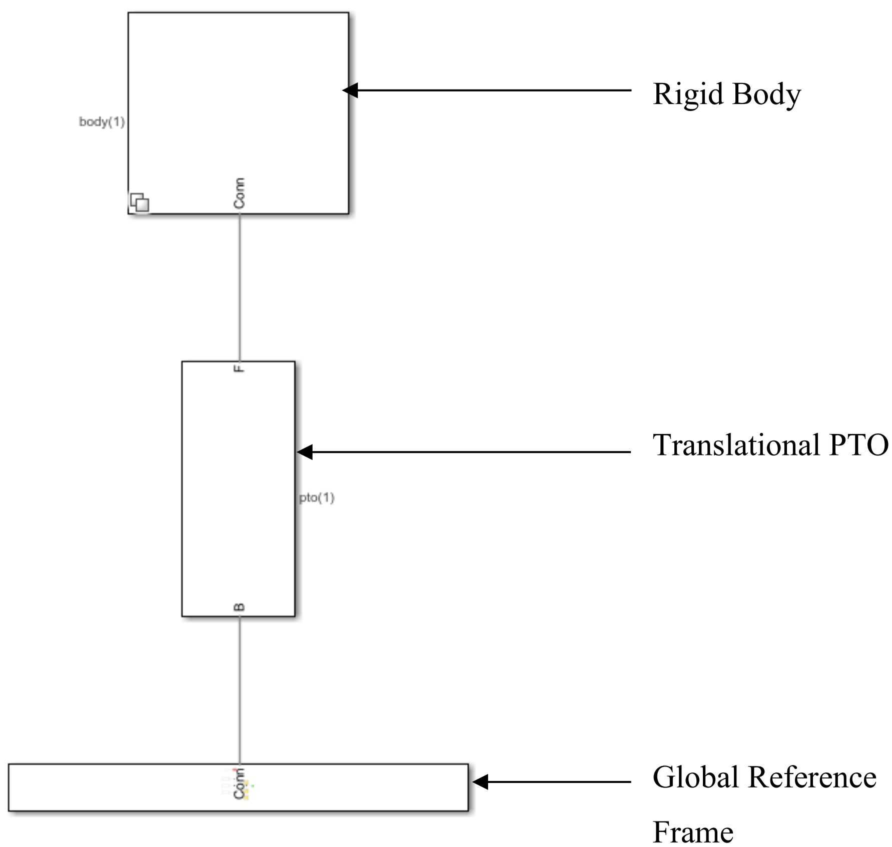

Figure 7.1 Simulink model of WEC

WEC-Sim simulations have been performed for different months with a ramp time of 100 s and a time step size of 0.05 s. The duration of the simulation was 86,400 s. After completing simulation, using the post-processing module of WEC-Sim, necessary plots of wave elevation, buoy response, and power have been obtained. In addition, from the output file, necessary data regarding the response and power output of the system have been extracted. Figure 7.2 – Figure 7.4 illustrate sample output curves of wave surface elevation, heave response of the buoy, and power output from the system.

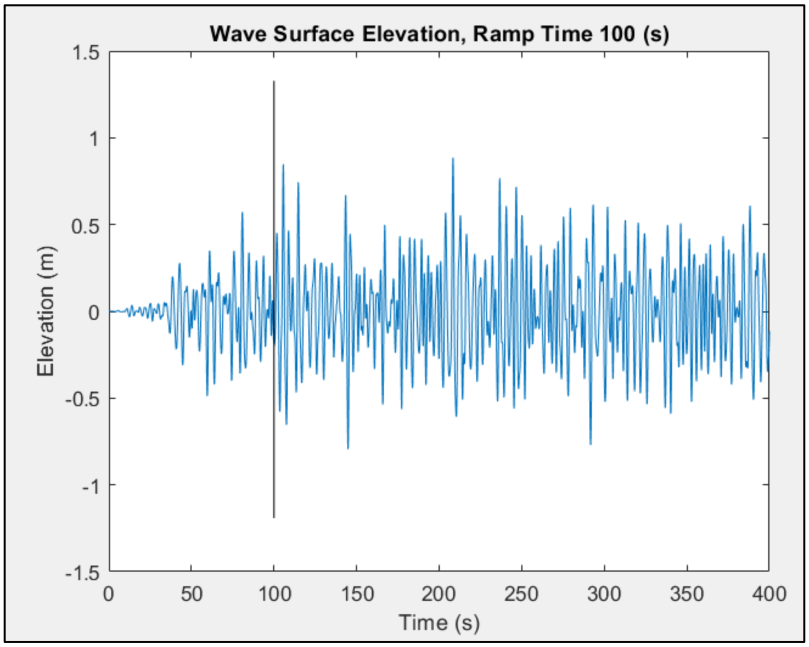

Figure 7.2 Change of wave surface elevation with time

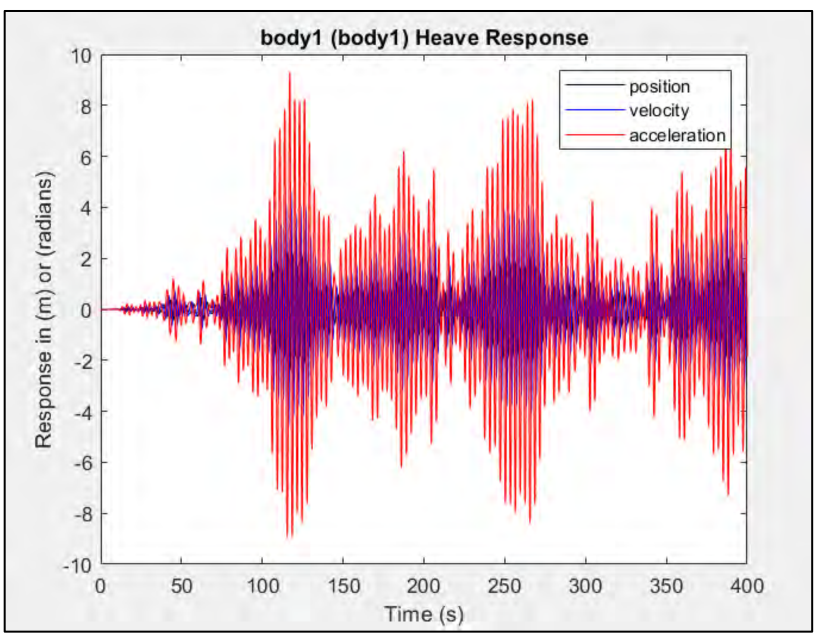

Figure 7.3 Change of position, velocity, and acceleration of the buoy with time

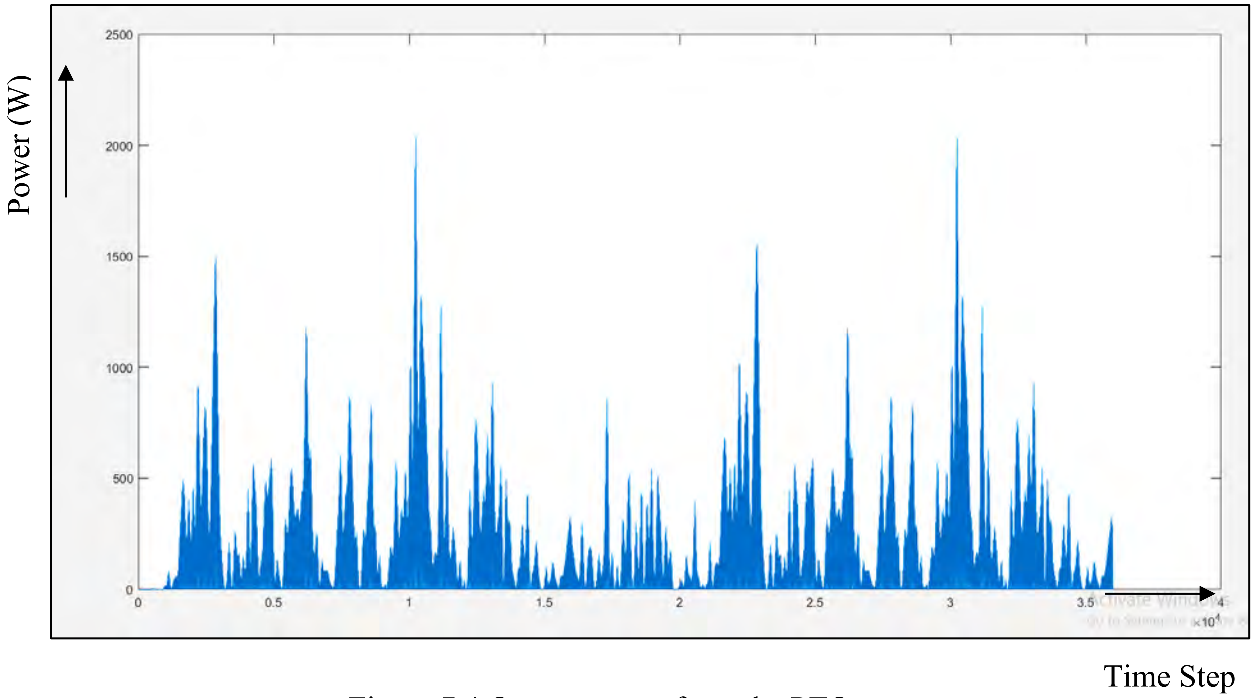

Figure 7.4 Output power from the PTO system

Based on the simulation results, the average power output of the cylindrical buoy with diameter of 1.2 m and draft of 2.4 m has been calculated and presented in Figure 7.5. As shown in the figure, the highest value of average wave power is obtained in October, which is 91.34 W. Notably, wave power outputs are comparatively higher in the months when the maximum percentage of irregular wave frequencies is close to buoy natural frequency (i.e., 0.25 Hz).

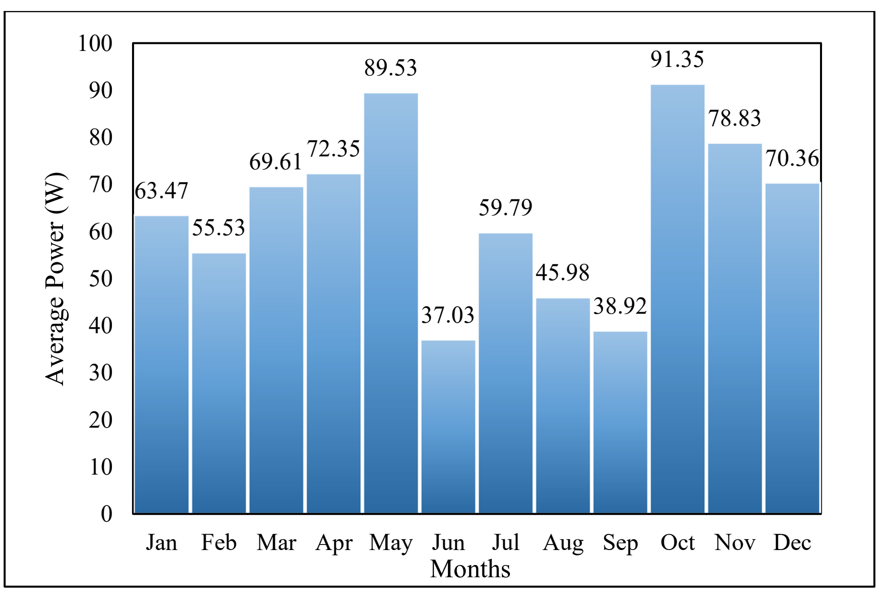

Figure 7.5 Average value of power production for different months

Finally, considering water depth of the intended energy deployment site and the size of the buoys, the following combinations of draft-diameter are considered for final simulations using WEC-Sim.

Table 7.1 Specifications of different cylindrical geometries

Geometry	G01	G02	G03	G04	G05	G06	G07	G08
Diameter	2.00	2.40	2.50	2.60	2.70	2.80	2.70	2.70
Draft	2.19	2.10	2.08	2.06	2.04	2.02	2.42	2.92

After 3-D diffraction and radiation analysis of these eight buoys in Ansys-AQWA, from hydrostatic results, the values of buoy stability parameters are extracted and listed in Table 7.2. Positive value of metacentric heights as well as restoring moments indicate stable equilibrium of all the eight buoys.

Table 7.2 Buoy stability calculation

	Diameter	Draft	Total Height	Vertical position of centre of gravity measured from bottom (KG)	Vertical position of centre of buoyancy measured from bottom (KB)	Metacentric height, GM	Restoring moment (N.m/^{o})	Comment
G01	2.0	2.2	2.7	1.345	1.095	0.136	163.91	Stable
G02	2.4	2.1	2.6	1.3	1.05	0.08	131.24	Stable
G03	2.5	2.08	2.58	1.29	1.04	0.063	111.82	Stable
G04	2.6	2.06	2.56	1.28	1.03	0.045	86.72	Stable
G05	2.7	2.04	2.54	1.27	1.02	0.027	55.26	Stable
G06	2.8	2.02	2.52	1.26	1.01	0.010	17.03	Stable
G07	2.7	2.42	2.92	1.46	1.21	0.062	150.6	Stable
G08	2.7	2.92	3.42	1.71	1.46	0.095	275.98	Stable

Other output curves of non-dimensionalized hydrodynamic coefficients (i.e., normalized radiation damping coefficient, normalized added mass coefficient), normalized excitation force, normalized IRF of radiation, and excitation forces are obtained using the BEMIO pre-processor. Sample curves are presented in Appendix (C).

The values of catenary shape parameters of these eight buoys are calculated and shown in Table 7.3. The shapes of the catenary mooring lines are presented in Appendix (B).

Table 7.3 Catenary mooring line shape parameter

	Force applied to the mooring line at the fairlead, F (tonnes)	Normalized thread diameter, d (mm)	No. of nodes	Horizontal distance between the fairlead and the touchdown point of the mooring line on the seabed, x (m)	Weight of the suspended chain, V (tonnes)	Cross sectional area of the thread, A (m^2)	Unit weight of the mooring line in water, w (tonnes/m)	Normalized horizontal tension component, T_0 (tonnes)	Catenary shape parameter, b	Length of the suspended mooring line, S (m)
G01	3.696	25	10	127.780	0.494	$4.9x10^{-4}$	$3.85x10^{-3}$	2.600	0.014	128.160
G02	5.073	25	10	149.911	0.579	$4.9x10^{-4}$	$3.85x10^{-3}$	3.600	0.011	150.239
G03	5.445	25	10	155.350	0.600	$4.9x10^{-4}$	$3.85x10^{-3}$	3.800	0.010	155.667
G04	5.827	25	10	160.738	0.621	$4.9x10^{-4}$	$3.85x10^{-3}$	4.100	0.009	161.044
G05	6.216	25	10	166.106	0.641	$4.9x10^{-4}$	$3.85x10^{-3}$	4.400	0.009	166.403
G06	6.613	25	10	171.305	0.661	$4.9x10^{-4}$	$3.85x10^{-3}$	4.672	0.008	171.593
G07	7.331	25	10	180.417	0.696	$4.9x10^{-4}$	$3.85x10^{-3}$	5.180	0.007	180.690
G08	8.798	25	10	197.756	0.763	$4.9x10^{-4}$	$3.85x10^{-3}$	6.219	0.006	198.005

Time-domain simulations of these eight buoys are performed using WEC-Sim, and values of mean absorbed power by the PTO system are extracted from the simulation results. The variations of mean absorbed power with buoy configurations are presented by bar charts in Figure 7.6. The values are also listed in Table 7.4.

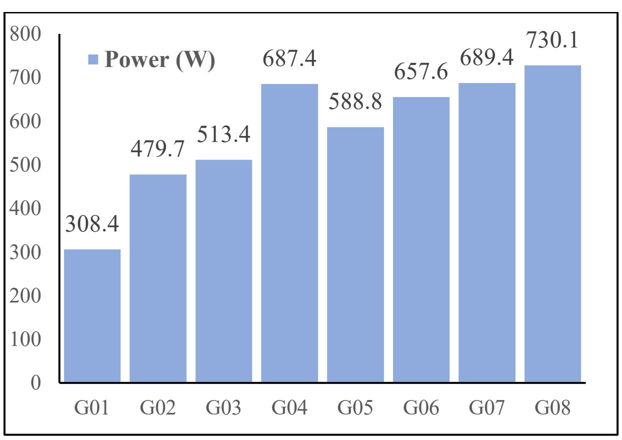

(a) January

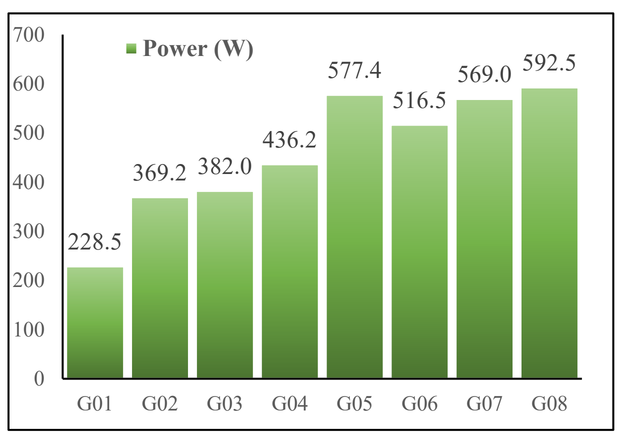

(b) February

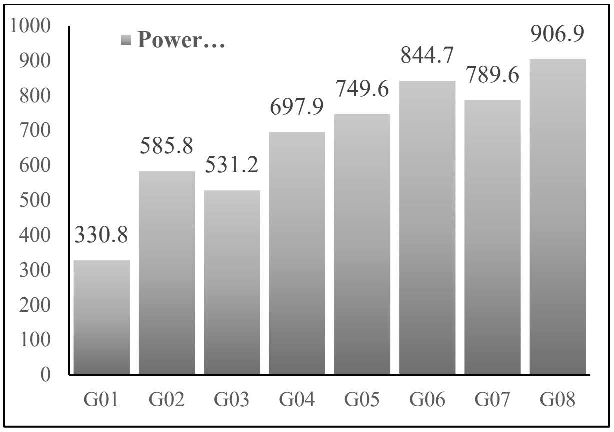

(c) March

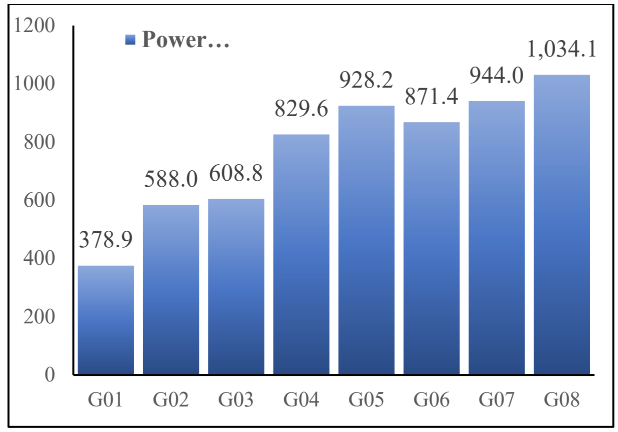

(d) April

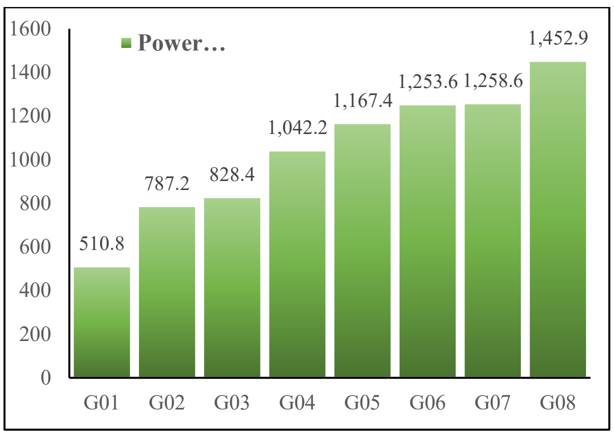

(e) May

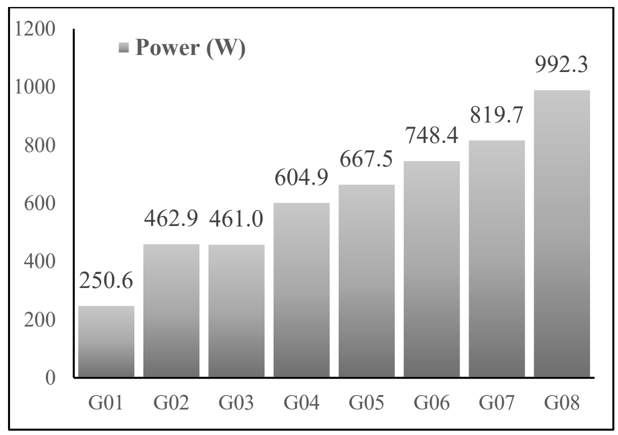

(f) June

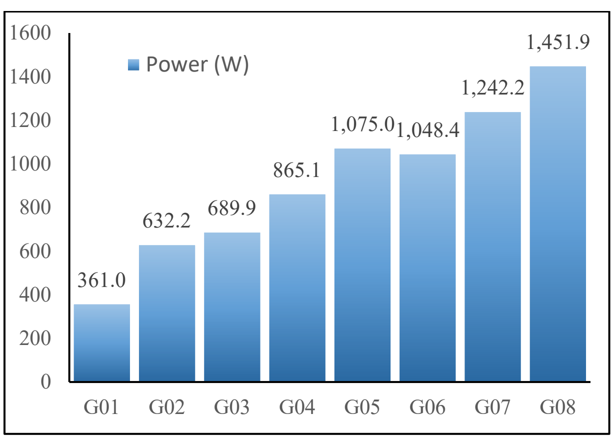

(g) July

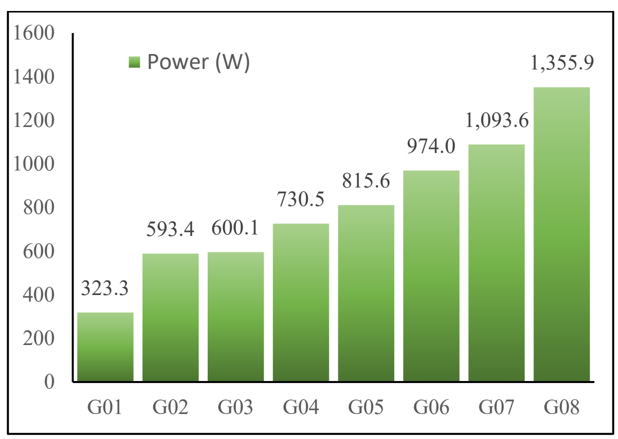

(h) August

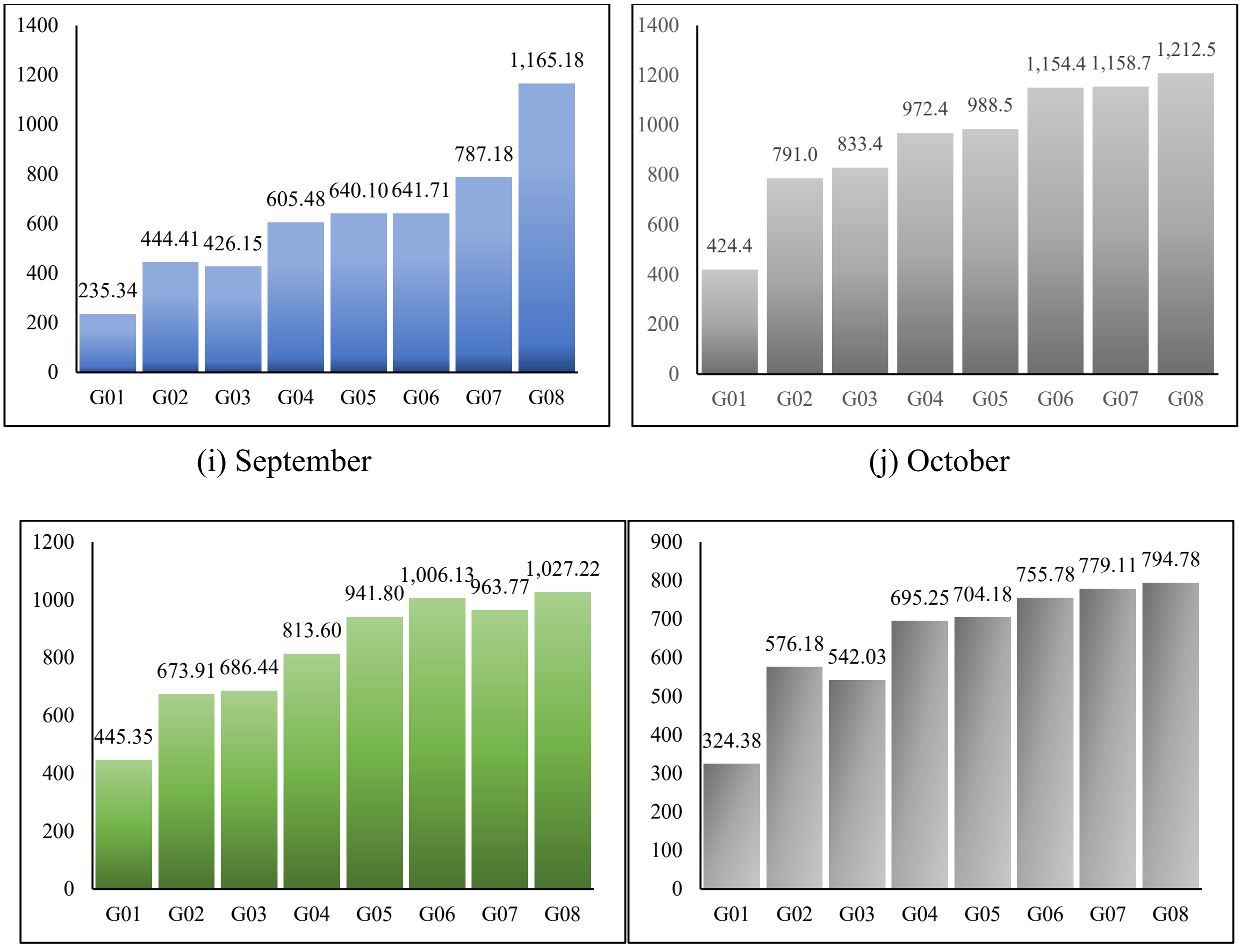

(i) September

(j) October

(k) November

(l) December

Figure 7.6 Average absorbed power of different buoy geometries of different months

Table 7.4 Average absorbed power for different months

Geometry	G01	G02	G03	G04	G05	G06	G07	G08
Months	**Power (W)**							
Jan	308.41	479.68	513.42	687.36	588.76	657.56	689.40	730.14
Feb	228.51	369.24	382.02	436.20	577.41	516.54	569.03	592.51
Mar	330.78	585.85	531.20	697.86	749.58	844.72	789.60	906.95
Apr	378.88	588.04	608.76	829.55	928.20	871.43	944.05	1034.11
May	510.78	787.22	828.44	1042.20	1167.43	1253.59	1258.59	1452.89
Jun	250.59	462.91	461.04	604.91	667.52	748.38	819.68	992.32
Jul	361.04	632.23	689.88	865.13	1074.98	1048.38	1242.17	1451.92
Aug	323.33	593.41	600.11	730.53	815.64	974.00	1093.63	1355.93
Sep	235.34	444.41	426.15	605.48	640.10	641.71	787.18	1165.18
Oct	424.44	791.03	833.38	972.37	988.54	1154.4	1158.66	1212.50
Nov	445.35	673.91	686.44	813.60	941.80	1006.13	963.77	1027.22
Dec	324.38	576.18	542.03	695.25	704.18	755.78	779.11	794.78

As can be seen from Figure 7.6 and Table 7.4, all the results show a trend of achieving maximum average power for geometry G08. The diameter of this geometry is 2.70 m, and the draft is 2.92 m. Geometry G05 and G06 are of the same diameter as G08 but with less draft in order. For these geometries, it can be seen from Table 7.4 that power generation increases with drafts at fixed diameter. However, such elevated power comes at the cost of increased weight (as larger draft increases mass and thus, weight) and hence manufacturing expense, which cannot be an optimal decision. To make it more realistic, consequently, average power per unit of buoy weight has been considered and shown in the following figure (Figure 7.7). This figure shows that using G06 will be optimal instead of G08. Thus, cylindrical buoy shape with the diameter of 2.70 m and draft of 2.02 m will capture wave power more efficiently from all existing sea states of the energy harnessing site.

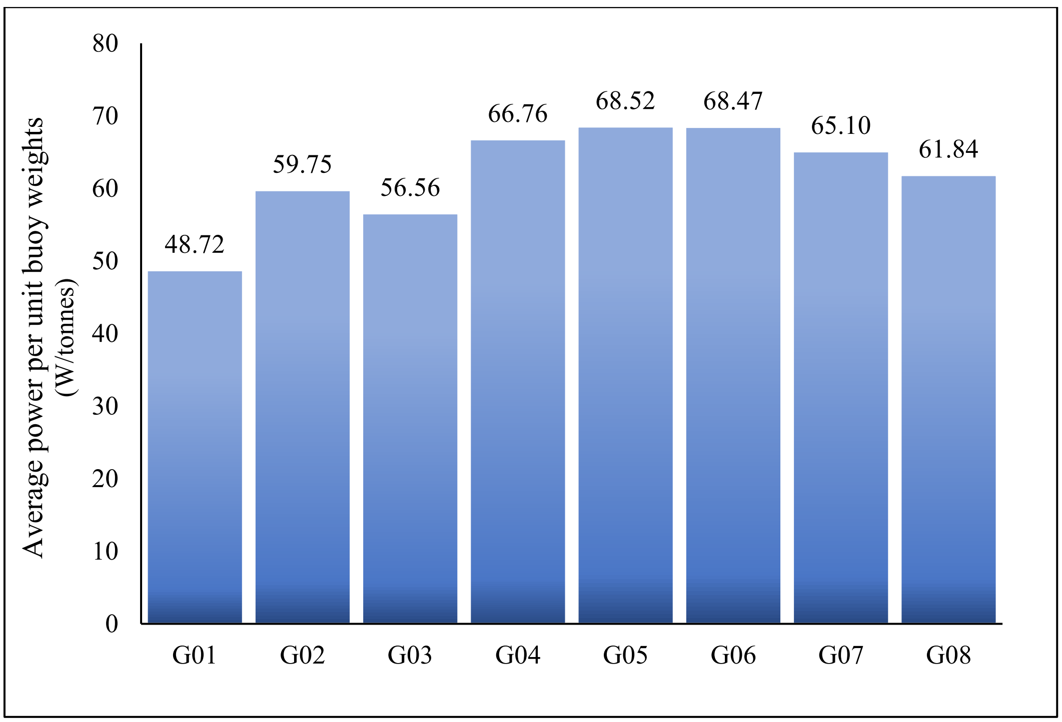

Figure 7.7 Power output per unit buoy weights for different cylindrical buoy

Examining Other Configurations:

In the previous section, all the experiments have been performed with cylindrical geometry. Final analysis provides us corresponding optimal dimensions such as diameter, draft, surface area, thickness, and underwater volume. In this section, we experiment with other configurations, particularly spherical and hexagonal shape buoys. Note that hexagonal type buoy has not yet been considered in the literature for evaluating power generation characteristics. To the best of our knowledge, this work will be the first one to do such analysis with th3 hexagonal shaped buoy. Hexagonal shape has been inspired by honeycomb structures found in nature.

Considering the resource limitations, we have not gone through the raw profile generation for spherical and hexagonal structures as done with the cylindrical buoy. Instead, we have used surface area and volume obtained from optimal cylindrical configurations to generate spherical and hexagonal profiles. The dimensions of spherical and hexagonal buoys are listed in the following table.

Table 7.5 Properties of spherical and hexagonal buoys

Spherical buoy		Hexagonal buoy	
Draft	2.5 m	Draft	2.04 m
Diameter	3.24 m	Side length	1.485 m
Surface area	32.996 m^2	Surface area	32.996 m^2
Total mass	11.972 tonnes	Total mass	11.972 tonnes
Thickness	46.22 mm	Total height and thickness	2.43 m, 46 mm

For analyzing the power generation performance of spherical and hexagonal buoys, the same procedures outlined for cylindrical buoy shapes have been followed. The representations of the geometries of the spherical and cylindrical buoys in the form of solid models are shown in Figure 7.8. Different colors represent the underwater portion and above-water portion of the buoys in calm sea condition.

Considering maximum element size and defeaturing tolerance of 0.05 m and 0.01 m, respectively, surface mesh of the buoys has been generated. Figure 7.9 illustrates the 3D mesh geometries of spherical and hexagonal buoys.

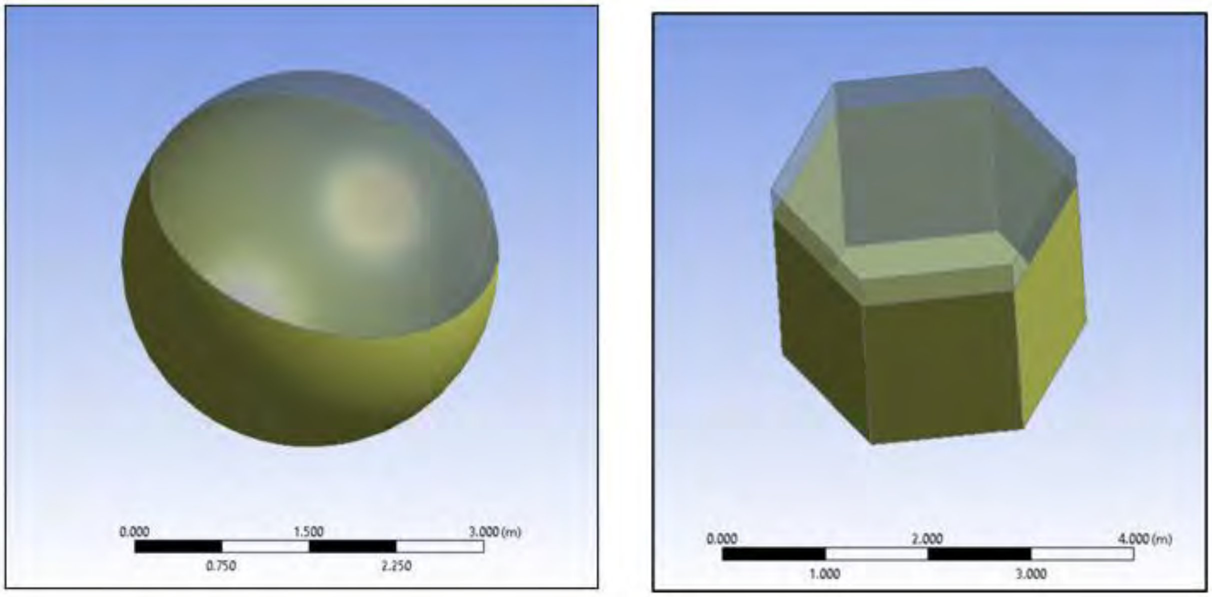

(a) (b)

Figure 7.8 AQWA model of (a) Spherical buoy, (b) hexagonal buoy

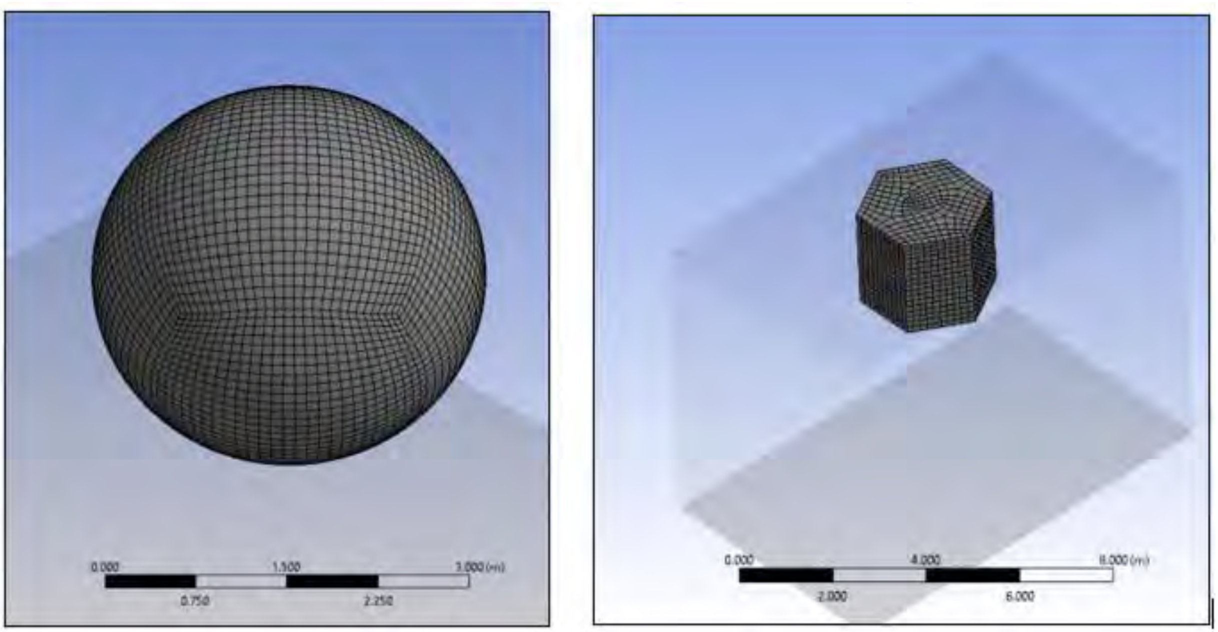

Figure 7.9 3D mesh geometry of spherical and hexagonal buoy

After performing 3D diffraction and radiation analysis using the hydrodynamic package, Ansys-AQWA, the wave force, structural response as well as hydrostatic data have been obtained. From the hydrostatic results, the stability criteria have been checked for both geometries, and satisfactory results have been found with positive restoring moments values. The non-dimensionalized value of hydrodynamic parameters such as radiation damping coefficients, added mass coefficients, impulse response function of radiation and excitation forces have been obtained after pre-processing hydrodynamic data using the BEMIO code of WEC-Sim. The results are presented graphically in Figures 7.10 - Figure 7.17. Noticeably, when comparing hydrodynamic diffraction analysis results of spherical and hexagonal buoys, spherical buoy slightly outperforms than hexagonal buoy. For example, at the resonce period, which is 4.0 s for both geometries, the value of normalized radiation damping coefficient is 1.75 for the spherical buoy, whereas the value is 0.88 for the hexagonal buoy. Similarly, at time period 4.0 s, the values of the normalized added mass coefficient are 4.72 and 4.51, respectively, for the spherical and hexagonal buoys.

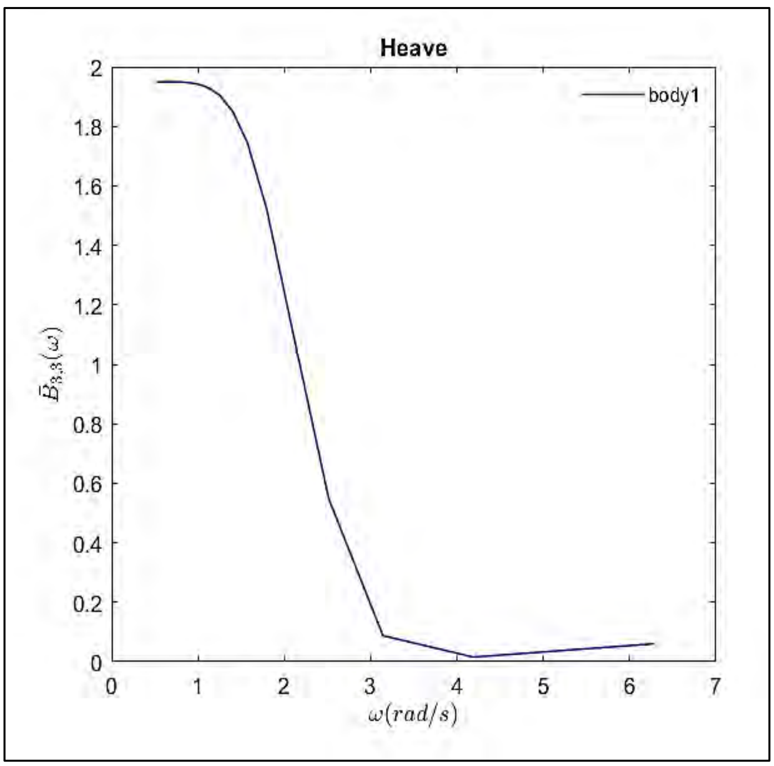

Figure 7.10 Normalized radiation damping coefficient (spherical buoy)

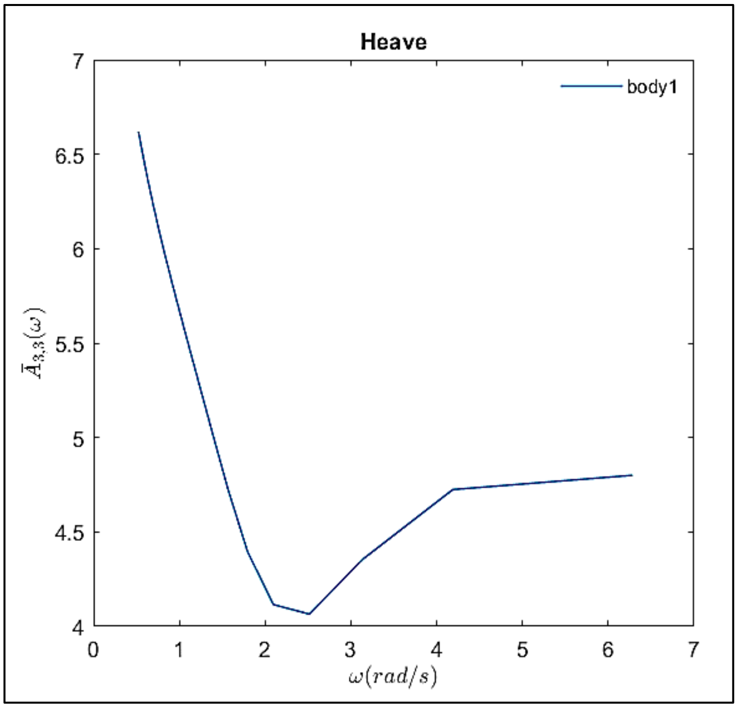

Figure 7.11 Normalized added mass coefficient (spherical buoy)

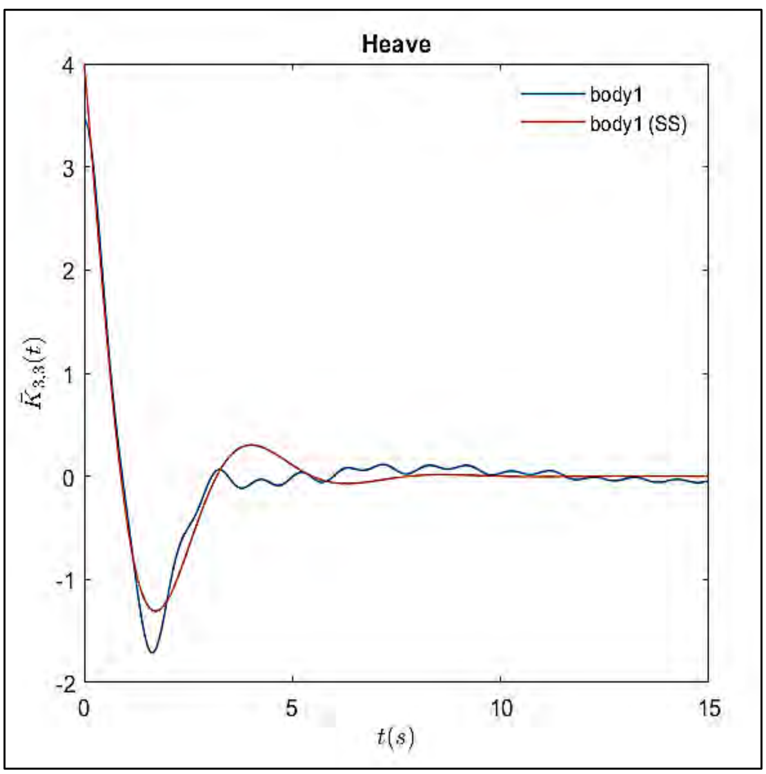

Figure 7.12 Normalized radiation IRF (spherical buoy)

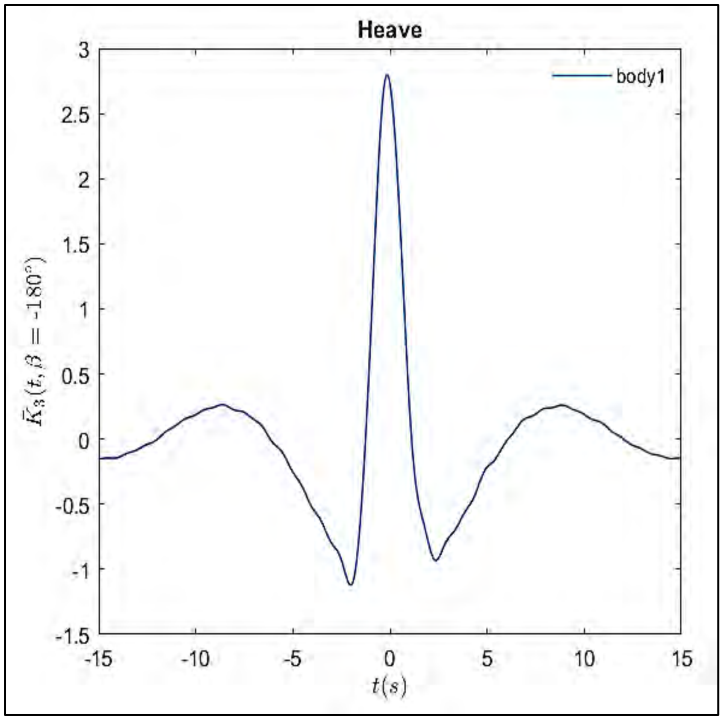

Figure 7.13 Normalized excitation IRF (spherical buoy)

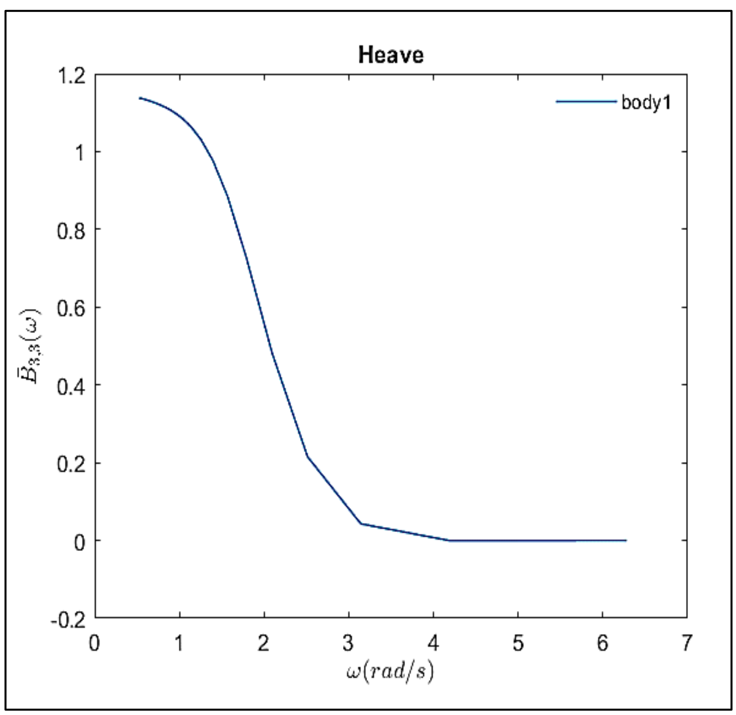

Figure 7.14 Normalized radiation damping coefficient (hexagonal buoy)

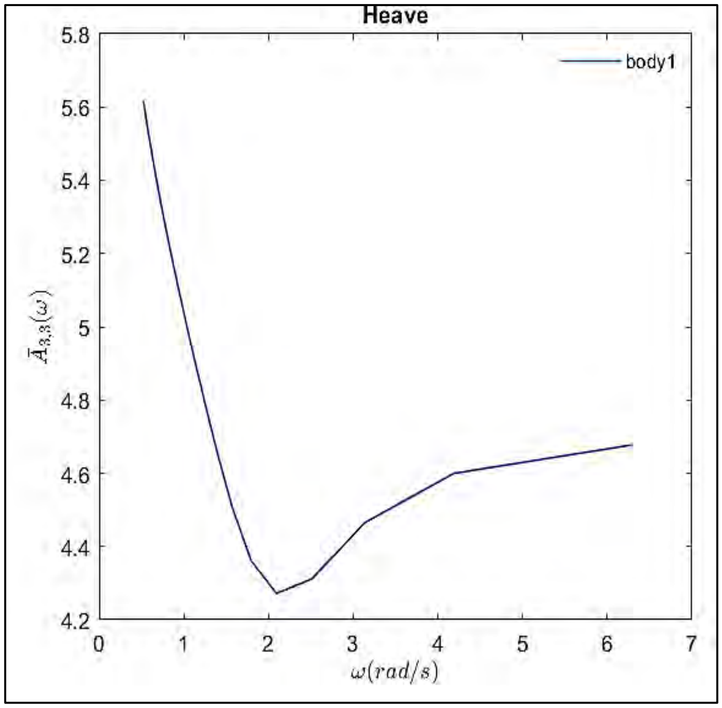

Figure 7.15 Normalized added mass coefficient (hexagonal buoy)

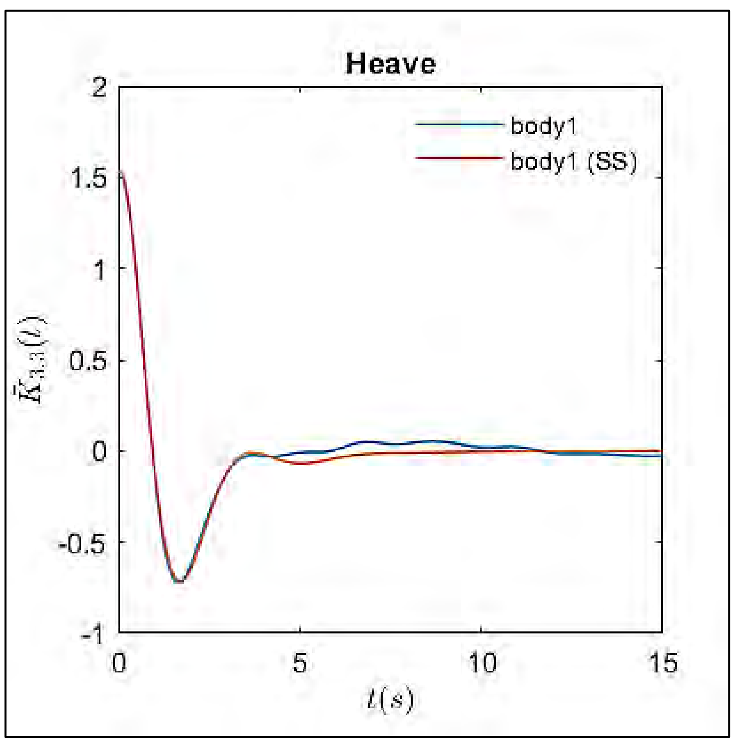

Figure 7.16 Normalized radiation IRF (hexagonal buoy)

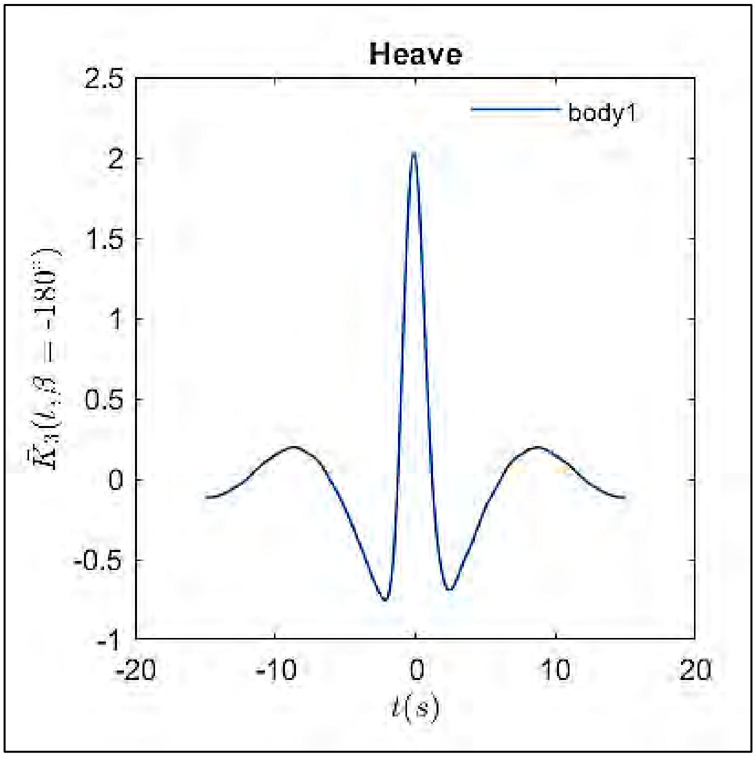

Figure 7.17 Normalized excitation IRF (spherical buoy)

The value of viscous drag coefficient for smooth spherical buoy is obtained using Figure 6.14. For smooth sphere, $C_D = 0.20$. For hexagonal buoy, the drag coefficient is considered 0.70.

At first, the power generation performance of the spherical and hexagonal buoy geometries in irregular seas has been determined and compared with optimized cylindrical geometry. WEC-Sim was used to model the hydrodynamic response of the selected designs. For each design, the damping coefficient of the PTO system has been chosen equal to the radiation damping coefficient at the resonance period. The simulation was performed for each month, and corresponding power output has been extracted from the simulation results. The average value of power production of the selected buoys has been determined and shown graphically in Figure 7.18. The values are also listed in Table 7.6.

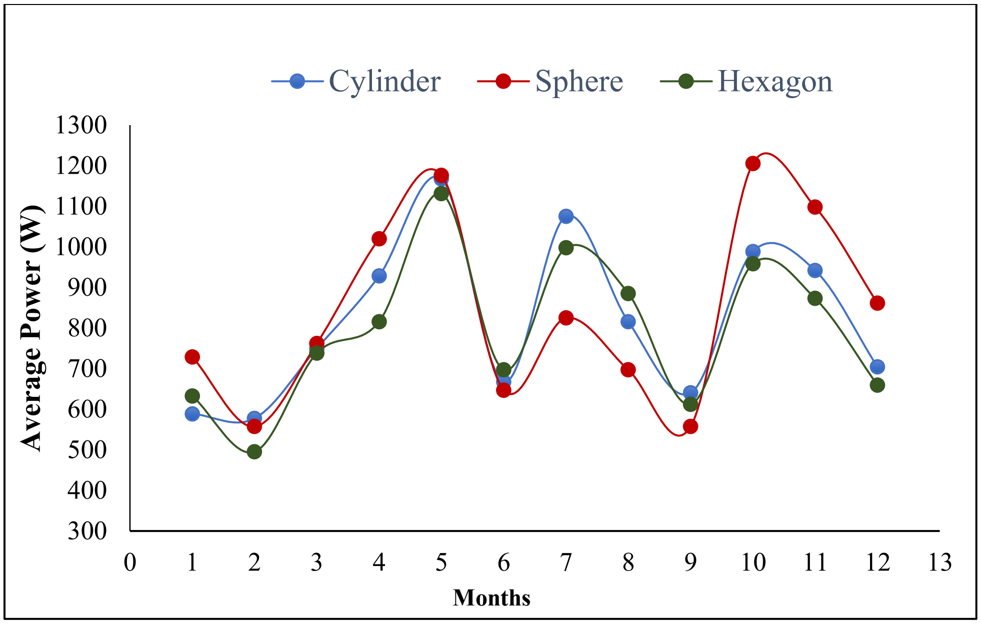

Figure 7.18 Monthly average value of power production of different buoy shapes considering irregular waves

Table 7.6 Comparison of the average power production of the selected designs

Month	Cylinder	Sphere	Hexagon
Jan	588.76	729.16	632.87
Feb	577.41	557.43	495.19
Mar	749.58	762.33	738.15
Apr	928.20	1019.87	815.87
May	1167.43	1176.54	1131.03
Jun	667.52	646.80	697.18
Jul	1074.98	824.74	997.60
Aug	815.64	697.04	885.07
Sep	640.10	557.29	612.12
Oct	988.54	1205.18	958.43
Nov	941.80	1097.75	872.85
Dec	704.18	861.19	659.44
Average	820.34	844.61	791.32

If we carefully observe the findings with irregular sea states, there is no regular trend. In particular, in the months February, July, and September, the power production performance of the cylindrical buoy shape is better than the other ones. Similarly, hexagonal buoy outperforms cylindrical and spherical buoys in the months June and August. For the rest of the months, spherical buoy produces the best results. However, if we consider the overall average power production of one year, then the power output from the spherical buoy, which is 844.61 W, is slightly higher than cylindrical (820.34 W) and hexagonal (791.32 W) designs.

If we consider the power performance of the selected design during peak season of tourists (October-February), except for February, for the other four months, the performance of the spherical buoy is significantly better.

The performance of the selected buoy shapes has also been checked considering regular wave conditions. The comparative results are shown graphically in Figure 7.19.

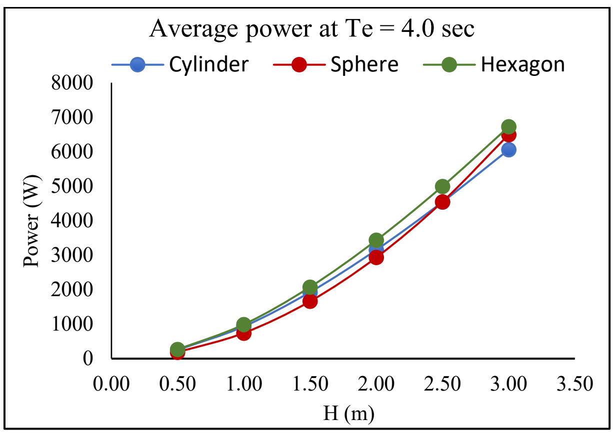

(a)

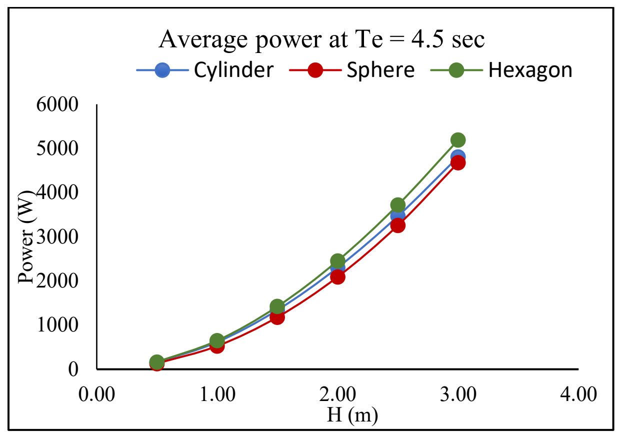

(b)

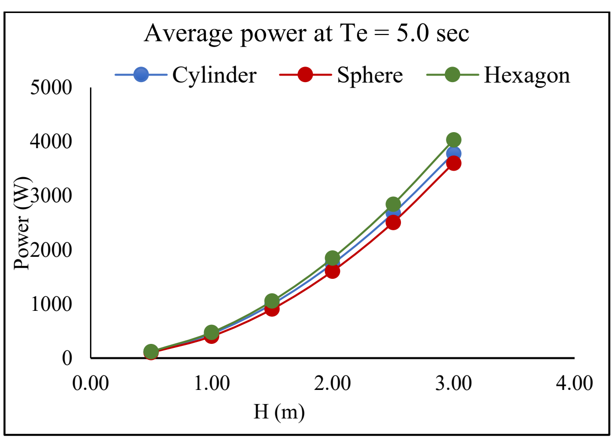

(c)

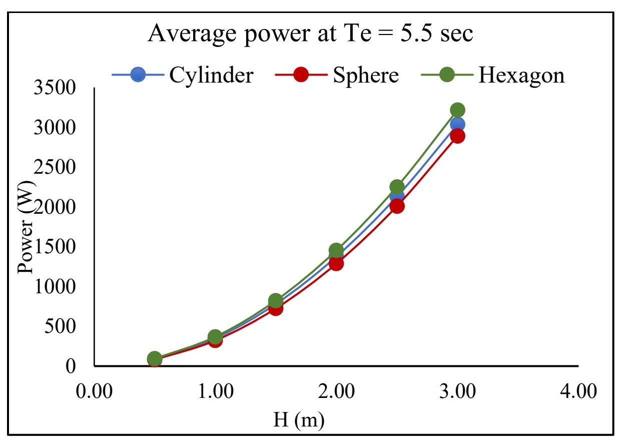

(d)

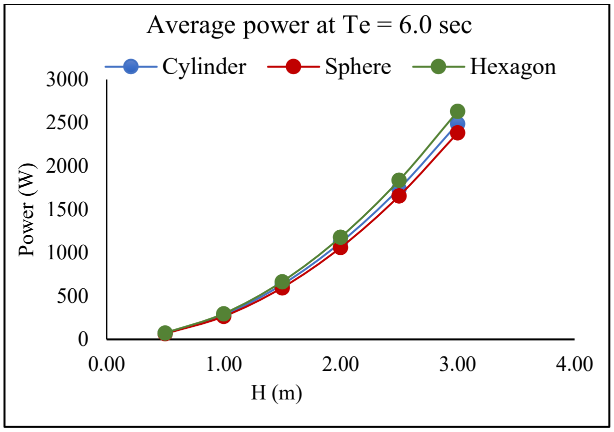

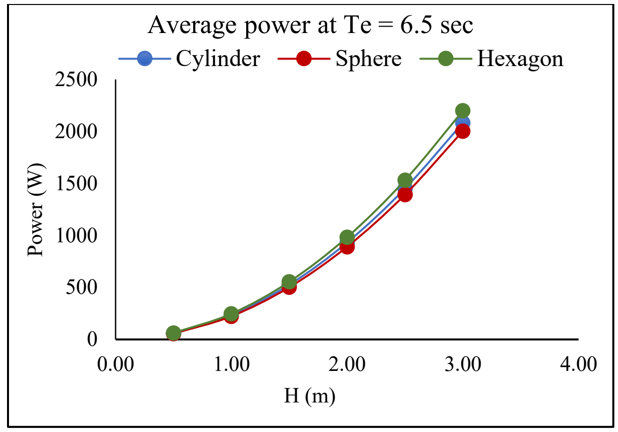

(e) (f)

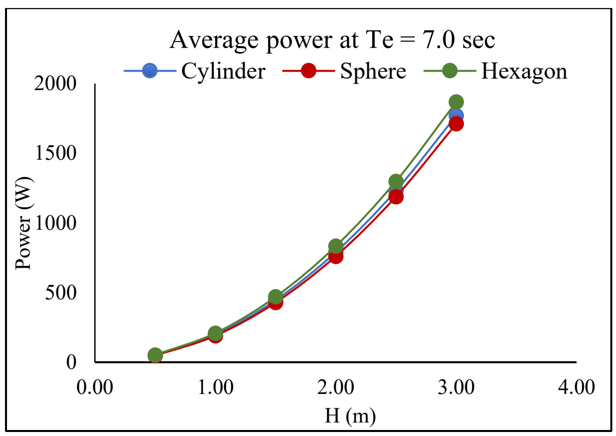

(g)

Figure 7.19 Monthly average value of power production of different buoy shapes considering regular waves

Figure 7.19 (a) shows the average power output of the selected designs for wave period 4.0 s and wave height values in the range of 0.5 m to 3.0 m. It can be seen that at constant wave period, power generation increases with increasing wave height values. Similar trends have also been found for other wave periods (Figure 7.19 (b) – Figure 7.19 (f)). In regular seas, hexagonal buoy shape shows better outcome than the cylindrical and spherical shapes buoy.

Comparative Study

For comparative purposes, a two-body point absorber model (RM3) has been utilized. Reference Model 3 or RM3 model is a validated model which was designed under Sandia national laboratories for a reference site located off the shore of Eureka in Humboldt County, California. The model consists of a float and a reaction plate (Figure 7.20). Mass properties of the RM3 WEC are listed in Table 7.7. The device converts wave energy into electrical power predominately from the device′s heave oscillation induced by incident waves.

The input files of the RM3 model are available on the developers′ website (https://wec-sim.github.io/WEC-Sim/dev/user/tutorials.html#two-body-point-absorber-rm3). Using the input files, the model has been simulated for regular waves with PTO damping equal to 1200 KNs/m. For different sea state values, the average value of wave power density per unit buoy diameter obtained from the RM3 model and optimized cylindrical buoy configuration are shown graphically against wave heights in Figure 7.21 and Figure 7.22, respectively. The values are also presented in Table 7.8. Two different wave energy periods (T_e = 4.0 sec and T_e = 7.0 sec) and wave height values in the range of 0.5 m to 3.0 m are considered during simulations.

As shown in Figure 7.21, for wave energy period, T_e = 4.0 sec, it is clear that power generation from the waves using optimized cylindrical buoy agrees very well with the RM3 model output. In fact, the results (power output per unit diameter) are almost equal for small waves with wave heights, H = 0.5 m, and 1.0 m. The difference in the results for other wave heights, i.e., 1.5 m, 2.0 m, 2.5 m, 3.0 m, is not significant. Moreover, the results follow the same trend, power generation increases with wave heights for the same wave energy period. Thus, we can conclude that power performance of the optimized cylindrical buoy shows satisfactory consistency with the RM3 model results for wave period 4.0 sec.

However, notable discrepancy of the results is observed for larger waves, i.e., regular waves with wave energy period of 7.0 sec. As the diameter of our optimized cylindrical buoy is very small (($\emptyset = 2.8\,m$) compared to the diameter of the float of the RM3 model ($\emptyset = 20\,m$), it can′t properly capture larger waves and extract available energy from waves.

Table 7.7 Mass properties and dimensions for the RM3 WEC

Body	CG	Mass (tonne)	Moment of Inertia Tensor (kg m^2)		
Float	0	727.01	20,907,301	0	0
	0		0	21,306,091	0
	-0.72		0	0	37,085,481
Plate	0	878.3	37,085,481	0	0
	0		0	94,407,091	0
	-21.29		0	0	28,542,225

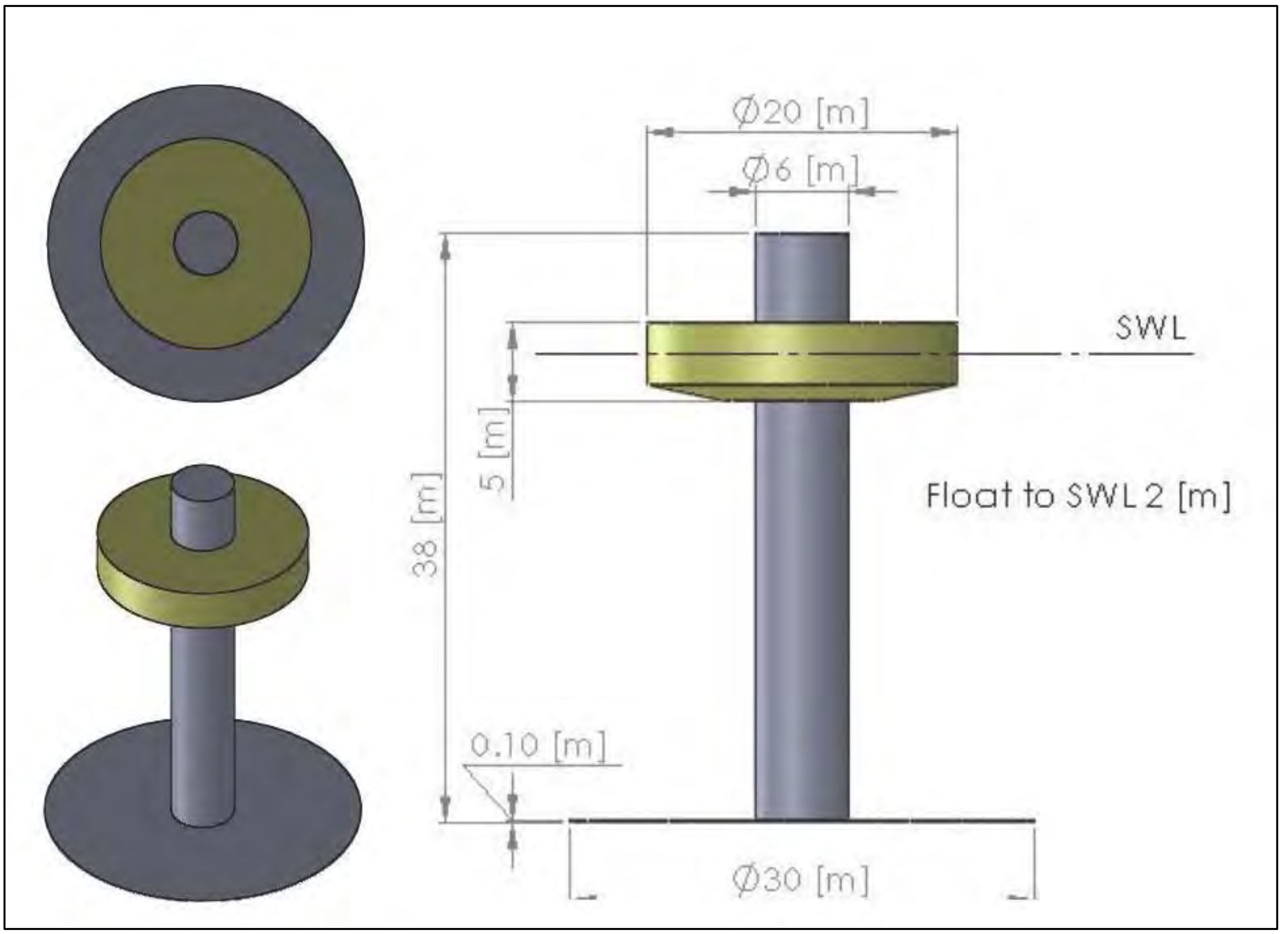

Figure 7.20 RM3 Model

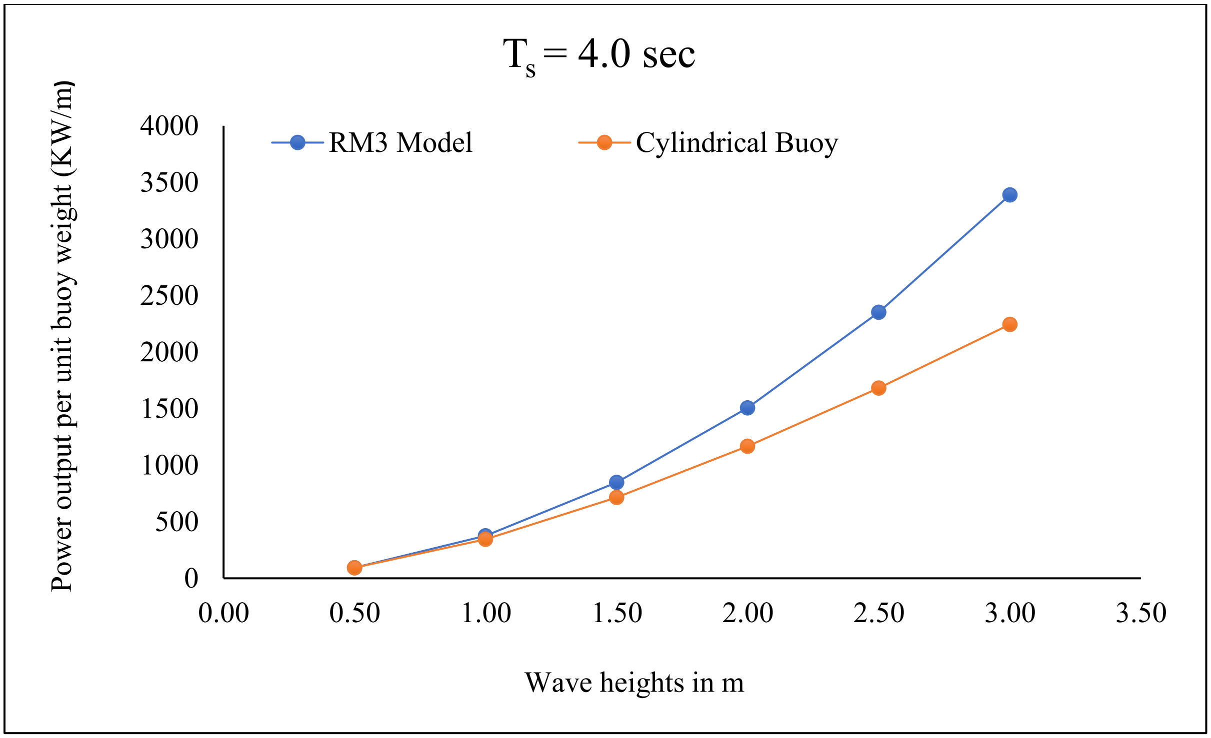

Figure 7.21 Power output per unit buoy diameter for different wave heights with T_s = 4.0 sec

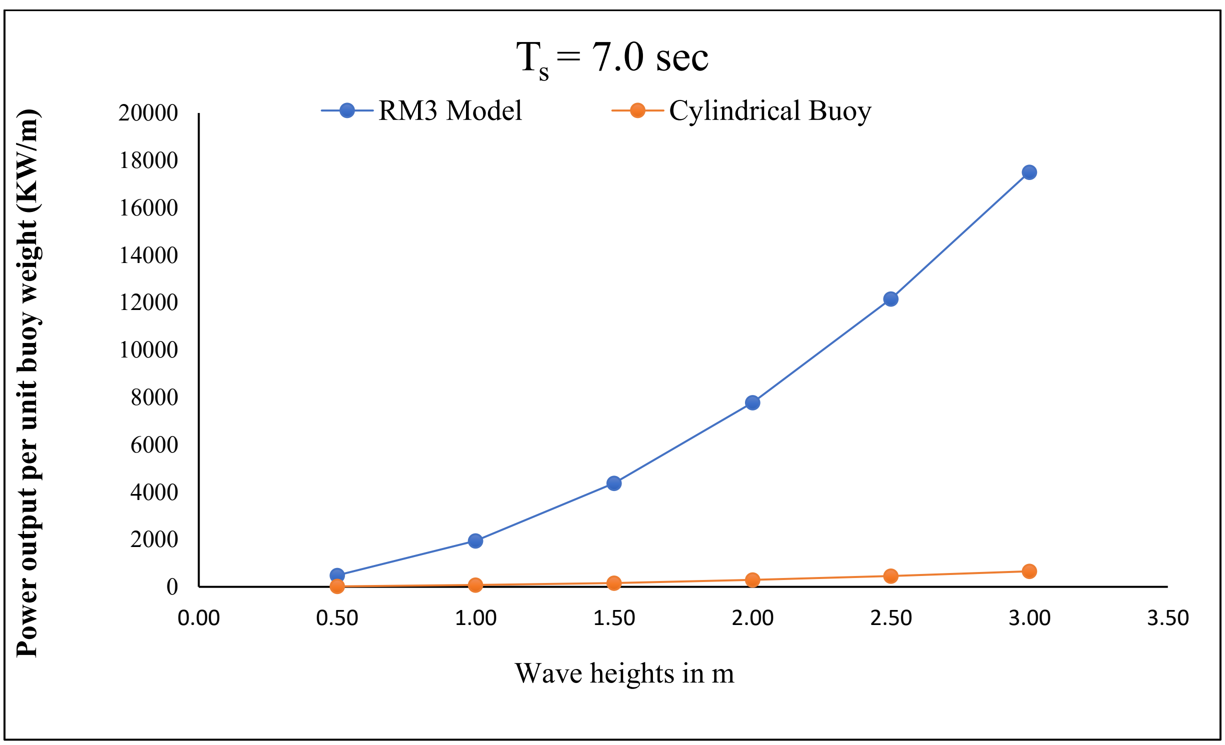

Figure 7.22 Power output per unit buoy diameter for different wave heights with T_s = 7.0 sec

Table 7.8 Comparison chart of power generation per unit buoy diameter from RM3 model and optimized cylindrical buoy

Te = 4.0 sec			Te = 7.0 sec		
	Power output per unit buoy diameter (KW/m)				
H (m)	RM3 Model	Optimized Cylindrical buoy	H (m)	RM3 Model	Optimized Cylindrical buoy
0.50	94.12	93.93	0.50	486.16	18.409
1.00	376.47	345.95	1.00	1944.69	73.410
1.50	847.05	714.52	1.50	4375.71	164.845
2.00	1505.86	1167.54	2.00	7779.45	292.502
2.50	2352.91	1682.45	2.50	12156.24	456.137
3.00	3388.19	2243.92	3.00	17506.49	655.461

Buoy Efficiency Calculation

To calculate efficiency of our designed cylindrical buoy, at first theoretically avaiable wave power density per meter wavefront is calculated using Equation 2.1.

For regular waves -

Equation 2.1 $\Rightarrow P_W \; = \frac{\rho g H^2}{16} \times \frac{g T_e}{2\pi} tanh(kh) \times \frac{1}{2} \times \left(1 + \frac{2kh}{sinh(2kh)}\right)\left(\frac{kW}{m}\right)$

Moreover, wavelength is calculated using Equation 6.4-

Equation 6.4 $\Rightarrow L \; = \frac{g}{2\pi} {T_e}^2 tanh(\frac{2\pi h}{L})$

For waves with wave height, H = 0.5 m, wave energy period, T_e = 4.0 sec, and water depth, h = 7.1 m, using equation 6.4, we get, wavelength, L = 23.83 m

∴ Wave power density per unit wavefront, P_W = 743.92 W/m

The diameter of the optimized cylindrical buoy is 2.8 m, hence, total power avaiable within the characteristic dimension i.e., diameter of the buoy is P_t = 2082.99 W

From simulation output, total power captured by the cylindrical buoy from waves with H = 0.5 m and T_e = 4.0 sec is 253.61 W.

Therefore, the efficiency of the buoy to capture waves with H = 0.5 m and T_e = 4.0 sec is 12.17%. Buoy efficiencies for the regular waves with wave energy period of 4.0 sec and wave heights in the range of 0.5 m to 3.0 m are listed in Table 7.9. As shown in Table 7.9, average buoy efficiency of the optimized cylindrical buoy is almost 10%. Notably, buoy efficiency decreases with increasing wave heights for the same wave energy period. The efficiency of other buoy shapes, i.e., spherical and hexagonal, is also nearly equal to the cylindrical shape.

Chandrasekaran and Harender (2012) worked on harnessing the heave motion of floating buoys to generate power using mechanical wave energy converter (MWEC). They found that the efficiency of their designed system was about 21% for regular waves with wave height and wave period of 2.5 m and 7.41 sec, respectively. Compared with the results obtained by Chandrasekaran and Harender (2012), the efficiency of our designed buoy is low. Instead of using regular geometries (i.e., cylindrical, spherical, hexagonal), modifications of the buoy geometry can improve buoy performance. Moreover, optimization of the PTO system and using mechanical, hydraulic, or pneumatic PTO systems can increase system efficiency.

Table 7.9 Buoy efficiency calculation

$T_e = 4.0\ sec$			
Wave height, H (m)	Total power avaiable, P_t (W)	Power absorbed by the buoy, P_b (W)	Buoy Efficiency η (%)
0.5	2082.99	253.61	12.17
1.0	8331.91	934.05	11.21
1.5	18746.91	1929.20	10.29
2.0	33327.83	3152.36	9.46
2.5	52074.74	4542.63	8.72
3.0	74987.63	6058.58	8.08

CHAPTER 8

CONCLUSIONS AND FUTURE SCOPES

Renewable energy has lot to do to save the planet from environmental change due to the usage of fossil fuels. Our country′s great resource of renewable energy has remained unutilized due to lack of research; Saint Martin is one of them. This research is an extension of a preceding work (Das et al., 2021) which reported that Saint Martin has enormous potential for renewable wave energy. In particular, this research is the first formal analysis of the actual electrical power production capacity using the prevailing wave energy spectrum around Saint Martin′s Island.

In this research, we attempt to select a suitable configuration for a heaving-point-absorber-wave-energy-converter to capture wave energy most efficiently. Using time-domain analysis of the designed WEC, the power generation performance was thoroughly evaluated. Also, the effects of design parameters such as diameter, draft, shape, etc., on buoy response, and thus, power output have been assessed. Through manual parametric study, several conclusions have been drawn for design optimization of a heave point absorber, which are as follows-

- With the increasing size of a cylindrical buoy shape, the hydrodynamic parameters, such as excitation force, radiation damping, added mass, etc., also increase. In addition, the power generation increases with buoy size. Considering the restrictions, such as available space, water depth, manufacturing, and maintenance cost, the optimized geometry of the cylindrical buoy has been chosen with diameter of 2.70 m and draft of 2.04 m.
- Comparing the performance of cylindrical, spherical, and conical buoys with constant surface area and underwater volume, it was found that, under regular sea conditions, hexagonal buoy slightly outperforms the other ones for a wide range of frequencies and wave heights.
- Under regular wave conditions, the response, as well as power output of each buoy, are maximum at 4.0 s wave energy period, which is the natural period of each buoy. Power output of each buoy reduces with decreasing frequencies.
- Under irregular wave conditions, the performance of the cylindrical buoy is slightly better during the months February, July, and September. Hexagonal buoy outperforms in the

months June and August. During the peak tourist season, spherical buoy performs better. Thus, which one should be finally used to generate electricity from wave energy is put as an open question to the designer.

- The efficiency of the optimized cylindrical buoy to capture available wave energy is found to be nearly 10%. The efficiency of the other buoy geometries, i.e., spherical and hexagonal, is also nearly equal to the cylindrical shape.
- If multiple buoys are arranged in an array, mass production is possible. However, analysis of the performance of WECs in an array should be done to evaluate the effects of the interaction between the devices on the overall performance, cost, and maintenance. Successful implementation of WEC to generate electricity will not only contribute to fulfilling the total electricity demand to some extent but also help to protect the coastal zone from storm waves.

Limitations:

- The primary limitation of this study stems from the underlying analysis method. Time-domain modelling and analysis use hydrodynamic coefficients and forces typically derived from linear potential flow models. However, first-order linear wave theory isn′t applicable for nearshore regions. From the site characteristics, it was found that Stokes 3rd-order theory is applicable to the location of interest.
- The wave spectrum used in the simulation of WEC in irregular seas were generated using the results of numerical wave-flow modelling through Delft-3D. However, to obtain more realistic results, measured wave characteristics data of the site is required.
- The most important part of any numerical modelling is model validation. Unfortunately, without wave-tank testing or full-scale model deployment, it is not possible to validate the results of numerical models.

Future recommendations:

- The limitations of the present study can be incorporated as research work for future examinations. Modelling of WECs as well as WEC arrays using nonlinear wave models with actual wave characteristic data is recommended.

- Although Saint Martin will be considered in this research, using the same methodology, preliminary analysis of the performance of wave energy converters can be evaluated for different water depths in the sea area of Bangladesh.
- Instead of the manual parametric study, evolutionary optimization techniques, such as genetic algorithm and swarm intelligence algorithm are recommended for future research on geometry optimization of WEC.
- Optimization of the PTO system, as well as modifications of the buoy shape, is necessary to increase the efficiency, i.e., to increase the power absorption capacity of the buoy from the available wave power.

REFERENCES

Aderinto, T. and Li, H., 2018. Ocean wave energy converters: Status and challenges. Energies, 11(5), p.1250.

Akpınar, A. and Kömürcü, M.İ., 2013. Assessment of wave energy resource of the Black Sea based on 15-year numerical hindcast data. Applied Energy, 101, pp.502-512.

Amiri, A., Panahi, R. and Radfar, S., 2016. Parametric study of two-body floating-point wave absorber. *Journal of marine science and application*, *15*(1), pp.41-49.

Beirao, P.J.B.F.N. and dos Santos Pereira Malça, C.M., 2014. Design and analysis of buoy geometries for a wave energy converter. International Journal of Energy and Environmental Engineering, 5(2), pp.1-11

Bhinder, M.A., Babarit, A., Gentaz, L. and Ferrant, P., 2015. Potential time domain model with viscous correction and CFD analysis of a generic surging floating wave energy converter. International Journal of Marine Energy, 10, pp.70-96.

Blanco, M., Santos-Herran, M., Navarro, G., Torres, J., Najera, J., Villaba, I., Lafoz, M. and Ramírez, D., 2021. Meta-heuristic optimisation approach for wave energy converter design by means of a stochastic hydrodynamic model. IET Renewable Power Generation, 15(3), pp.548-561.

Bouhrim, H., Citation: Hafsa Bouhrim, Abdellatif El Marjani. Wave Energy Assessment Along the Moroccan Atlantic Coast [J]. Journal of Marine Science and Application, 2019,(2): 142-152.[doi: 10.1007/s11804-018-00060-8].

Budal, K. and Falnes, J., 1982. Wave power conversion by point absorbers: A Norwegian project. International Journal of Ambient Energy, 3(2), pp.59-67.

Chandrasekaran, S. and Harender, 2012. Power generation using Mechanical wave energy converter. *The International Journal of Ocean and Climate Systems*, *3*(1), pp.57-70.

Charlier, R.H. and Justus, J.R., 1993. Ocean energies: environmental, economic and technological aspects of alternative power sources.

Cruz, J., 2007. Ocean wave energy: current status and future prespectives. Springer Science & Business Media.

Czech, B. and Bauer, P., 2012. Wave energy converter concepts: Design challenges and classification. *IEEE Industrial Electronics Magazine*, *6*(2), pp.4-16.

Das, M., Islam, M.R. and Shazeeb, T.I., 2021. Analysis of Wave Energy Resources Around the Saint Martin Island in Bangladesh. Journal of Marine Science and Application, 20(2), pp.248-267.

Das, M., Shazeeb, T.I. and Islam, M.R., 2018. Numerical investigation of wave energy of Saint Martin region of Bangladesh. In Proceedings of the 11th International Conference on Marine Technology (MARTEC), UTM, Kuala Lumpur (pp. 39-44).

De Andrés, A.D., Guanche, R., Armesto, J.A., Del Jesus, F., Vidal, C. and Losada, I.J., 2013. Time domain model for a two-body heave converter: Model and applications. Ocean Engineering, 72, pp.116-123.

Espindola, R.L. and Araújo, A.M., 2017. Wave energy resource of Brazil: An analysis from 35 years of ERA-Interim reanalysis data. PLoS One, 12(8), p.e0183501.

Falnes, J. and Lillebekken, P.M., 2003. Budal's latching-controlled-buoy type wave-power plant.

Folley, M. ed., 2016. Numerical modelling of wave energy converters: state-of-the-art techniques for single devices and arrays. Academic Press.

Gao, W., 2018. *Modelling of windage and churning losses in high speed rolling element bearings* (Doctoral dissertation, Lyon).

Hossain, M.S., Kamal, M., Adan, J., Chakrabartty, A., ShataddruTahsin, S., Arafat, Y. and Rahman, E., Generation of Electricity using Point Absorber Wave Energy Converter and its Prospect in Bangladesh. In 2019 IEEE International Conference on Power, Electrical, and Electronics and Industrial Applications (PEEIACON) (pp. 27-30). IEEE.

Hughes, M.G. and Heap, A.D., 2010. National-scale wave energy resource assessment for Australia. Renewable Energy, 35(8), pp.1783-1791.

Iglesias, G. and Carballo, R., 2010. Wave energy and nearshore hot spots: The case of the SE Bay of Biscay. Renewable Energy, 35(11), pp.2490-2500.

Islam, M.T., Uddin, M.G., Chakma, T.B. and Chowdhury, M.Z.R., 2014. Feasibility study of ocean wave of the Bay of Bengal to generate electricity as a renewable energy with a proposed design of energy conversion system. International Journal of Renewable Energy Research (IJRER), 4(2), pp.445-452.

Islam, S. and Khan, M.Z.R., 2017. A review of energy sector of Bangladesh. Energy Procedia, 110, pp.611-618.

Kumar, V.S. and Anoop, T.R., 2015. Wave energy resource assessment for the Indian shelf seas. Renewable Energy, 76, pp.212-219.

Kumar, V.S., Dubhashi, K.K., Nair, T.B. and Singh, J., 2013. Wave power potential at a few shallow-water locations around Indian coast. Current science, pp.1219-1224.

Li, Y. and Yu, Y.H., 2012. A synthesis of numerical methods for modeling wave energy converter-point absorbers. Renewable and Sustainable Energy Reviews, 16(6), pp.4352-4364.

Monteforte, M., Re, C.L. and Ferreri, G.B., 2015. Wave energy assessment in Sicily (Italy). Renewable Energy, 78, pp.276-287.

Monteiro, W.M.L., Sarmento, A.J., Fernandes, A.J. and Fernandes, J.M., 2016. Statistical analysis of wave energy resources available for conversion at natural caves of cape-Verde Islands. Ocean Science Discussions, pp.1-23.

Ricci, P., Saulnier, J.B., Falca˜ o, A.N.F.D.O. and Pontes, M.T., 2008, January. Time-domain models and wave energy converters performance assessment. In International Conference on Offshore Mechanics and Arctic Engineering (Vol. 48234, pp. 699-708).

Sergiienko, N.Y., Neshat, M., da Silva, L.S., Alexander, B. and Wagner, M., 2020, August. Design optimisation of a multi-mode wave energy converter. In International Conference on Offshore Mechanics and Arctic Engineering (Vol. 84416, p. V009T09A039). American Society of Mechanical Engineers.

Veritas, N., 2000. Environmental conditions and environmental loads. Oslo, Norway: Det Norske Veritas.

Wan, Y., Fan, C., Dai, Y., Li, L., Sun, W., Zhou, P. and Qu, X., 2018. Assessment of the joint development potential of wave and wind energy in the South China Sea. Energies, 11(2), p.398.

Wan, Y., Fan, C., Zhang, J., Meng, J., Dai, Y., Li, L., Sun, W., Zhou, P., Wang, J. and Zhang, X., 2017. Wave energy resource assessment off the coast of China around the Zhoushan Islands. Energies, 10(9), p.1320.

Xie, J. and Zuo, L., 2013. Dynamics and control of ocean wave energy converters. *International Journal of Dynamics and Control*, *1*(3), pp.262-276.

Yaakob, O., Hashim, F.E., Omar, K.M., Din, A.H.M. and Koh, K.K., 2016. Satellite-based wave data and wave energy resource assessment for South China Sea. Renewable energy, 88, pp.359-371.

Yu, Y.H., Li, Y., Hallett, K. and Hotimsky, C., 2014, June. Design and analysis for a floating oscillating surge wave energy converter. In International Conference on Offshore Mechanics and Arctic Engineering (Vol. 45547, p. V09BT09A048). American Society of Mechanical Engineers.

Zheng, C.W., Pan, J. and Li, J.X., 2013. Assessing the China Sea wind energy and wave energy resources from 1988 to 2009. Ocean engineering, 65, pp.39-48.

Zheng, C., Shao, L., Shi, W., Su, Q., Lin, G., Li, X. and Chen, X., 2014. An assessment of global ocean wave energy resources over the last 45 a. Acta Oceanologica Sinica, 33(1), pp.92-101.

Zheng, C., Zhuang, H., Li, X. and Li, X., 2012. Wind energy and wave energy resources assessment in the East China Sea and South China Sea. Science China Technological Sciences, 55(1), pp.163-173.

APPENDIX A

Sample output file obtained from hydrodynamic diffraction analysis using Ansys-AQWA

1. .AH1 File

```
GENERAL
  1           7.100    1025.000       9.810     0     0
COG
  1           0.000       0.000      -0.622
DRAFT
  1           2.020
COB
  1           0.000       0.000      -1.010
DISPLACEMENT
  1        1.5860E+00


ADDEDMASS
  1  1   1   1.4138E+03  2.9125E-02  4.1267E-03  7.6076E-03 -4.4056E+02  6.7515E-07
            -2.8523E-02  1.4138E+03  8.9970E-03  4.4055E+02  7.4752E-03 -6.9872E-06
            -5.0030E-03 -1.1926E-02  2.7813E+02 -1.7297E-02  8.0140E-03 -8.0418E-03
            -6.5154E-03  4.4029E+02  7.4690E-03  4.4298E+02  3.6367E-03 -1.6742E-06
            -4.4029E+02 -6.9823E-03 -3.0176E-03 -4.2418E-03  4.4299E+02 -5.0503E-07
             8.9552E-07 -6.4350E-06 -7.9339E-03 -7.3902E-07 -9.1069E-07  1.9121E-06


DAMPING
  1  1   1   3.8323E-01  2.1307E-05 -1.2083E-05  7.3257E-06 -1.2656E-01 -1.3082E-09
            -2.2830E-05  3.8323E-01  2.7044E-06  1.2655E-01  7.4618E-06 -1.8653E-09
            -4.0948E-04 -9.5361E-04  1.1871E+01 -1.4034E-03  6.1581E-04 -1.6759E-03
            -6.4333E-06  1.2636E-01  1.9365E-05  4.1723E-02  2.5338E-06 -2.8439E-09
            -1.2636E-01 -6.5921E-06  3.1077E-05 -1.9445E-06  4.1725E-02 -3.4665E-09
             5.7277E-08  1.3125E-07 -1.6594E-03  1.9554E-07 -8.6090E-08  2.3426E-07
```

```
FORCERAO
  1  1   1   1.8876E+03  1.6342E-02  7.4646E+03  1.3610E-02  6.2239E+02  1.0434E+00
                  90.01       85.50       -0.05       42.98      -89.98      179.95
  1  1   2   1.9718E+03  1.7764E-02  7.4262E+03  1.4761E-02  6.4882E+02  1.0408E+00
                  90.02      106.32       -0.05       39.99      -89.98      179.95
  1  1   3   2.0638E+03  1.8270E-02  7.3825E+03  1.4334E-02  6.7756E+02  1.0377E+00
                  90.02      104.33       -0.06       43.08      -89.98      179.94
  1  1   4   2.1651E+03  1.8397E-02  7.3326E+03  1.5354E-02  7.0893E+02  1.0343E+00
                  90.02       87.13       -0.06       43.24      -89.98      179.94
  1  1   5   2.2770E+03  1.9600E-02  7.2752E+03  1.4678E-02  7.4329E+02  1.0303E+00
                  90.02      100.26       -0.07       47.66      -89.98      179.93
  1  1   6   2.4014E+03  2.1070E-02  7.2088E+03  1.5702E-02  7.8108E+02  1.0257E+00
                  90.02      102.25       -0.08       47.33      -89.97      179.92
```

2. .LIS file

```
   INPUT    STRUCTURE    NODE
 SEQUENCE       NO.       NO.         X           Y           Z
 ----------------------------------------------------------------

     1          1          1       0.0000      0.5000      0.0000
     2          1          2       0.0000      0.5000     -0.0297
     3          1          3      -0.0291      0.4992      0.0000
     4          1          4      -0.0291      0.4992     -0.0297
     5          1          5       0.0000      0.5000     -0.0594
     6          1          6      -0.0291      0.4992     -0.0594
     7          1          7       0.0000      0.5000     -0.0891
     8          1          8      -0.0291      0.4992     -0.0891
     9          1          9       0.0000      0.5000     -0.1189
    10          1         10      -0.0291      0.4992     -0.1189
    11          1         11       0.0000      0.5000     -0.1486
    12          1         12      -0.0291      0.4992     -0.1486
    13          1         13       0.0000      0.5000     -0.1783
```

```
FORCES    FREQUENCY    DIRECTION (DEGREES)
------    ---------    -------------------
DUE TO (RADIANS/SEC)-180.0     -135.0      -90.0      -45.0        0.0       45.0       90.0      135.0      180.0
------ ------------- -----------------------------------------------------------------------------------------
DRIFT
-----
SWAY(Y)
                0.524  -1.62E-03 -5.51E-04 -9.95E-04 -4.11E-04 -1.48E-03 -7.40E-04 -9.88E-04 -5.14E-04 -1.77E-03
                0.546  -2.08E-03 -4.05E-03 -2.23E-03 -2.67E-03 -2.46E-03 -4.32E-03 -2.58E-03 -2.99E-03 -1.89E-03
                0.571  -1.27E-03 -1.19E-03 -2.22E-03 -1.01E-03 -1.18E-03 -1.43E-03 -1.95E-03 -1.56E-03 -1.43E-03
                0.598  -1.95E-03 -3.25E-03 -2.69E-03 -1.65E-03 -2.13E-03 -3.09E-03 -2.81E-03 -1.84E-03 -2.03E-03
                0.628  -3.84E-03 -1.59E-03 -2.53E-03 -1.97E-03 -3.90E-03 -8.56E-04 -2.30E-03 -1.74E-03 -3.91E-03
                0.661  -3.56E-03 -1.19E-03 -2.88E-03  5.08E-04 -3.53E-03 -1.73E-03 -2.51E-03  1.96E-04 -3.54E-03
                0.698  -4.30E-03 -1.56E-03 -4.84E-03 -4.00E-03 -4.21E-03 -2.16E-03 -4.74E-03 -3.96E-03 -4.13E-03
                0.739  -2.17E-03 -3.53E-03 -5.29E-03 -2.91E-03 -2.18E-03 -4.22E-03 -4.84E-03 -3.23E-03 -2.06E-03
                0.785  -2.95E-03 -5.61E-03 -6.91E-03 -3.83E-03 -3.09E-03 -5.07E-03 -6.93E-03 -4.15E-03 -2.98E-03
                0.838  -5.70E-03 -4.33E-03 -6.02E-03 -4.13E-03 -5.95E-03 -5.65E-03 -5.73E-03 -3.87E-03 -5.73E-03
```

ELEMENT NUMBER	NODE NUMBERS 1	2	3	4	FACET RADIUS	FACET AREA	POSITION OF CENTROID X	Y	Z	CORRECTION FACTOR	OUTWARD NORMALS X	Y	Z	ASPECT RATIO	SHAPE FACTOR	MIN. RAD.	AREA RATIO
691	701	702	771	770	0.02	0.8652E-03	-0.29	0.41	-0.31	0.994	-0.574	0.819	0.000	0.980	1.00	1.75	1.00
692	702	703	772	771	0.02	0.8652E-03	-0.29	0.41	-0.34	0.994	-0.574	0.819	0.000	0.980	1.00	1.75	1.00
693	703	704	773	772	0.02	0.8652E-03	-0.29	0.41	-0.37	0.994	-0.574	0.819	0.000	0.980	1.00	1.75	1.00
694	704	705	774	773	0.02	0.8652E-03	-0.29	0.41	-0.40	0.994	-0.574	0.819	0.000	0.980	1.00	1.75	1.00
695	705	706	775	774	0.02	0.8652E-03	-0.29	0.41	-0.43	0.994	-0.574	0.819	0.000	0.980	1.00	1.75	1.00
696	706	707	776	775	0.02	0.8652E-03	-0.29	0.41	-0.46	0.994	-0.574	0.819	0.000	0.980	1.00	1.75	1.00
697	707	708	777	776	0.02	0.8652E-03	-0.29	0.41	-0.49	0.994	-0.574	0.819	0.000	0.980	1.00	1.75	1.00
698	708	709	778	777	0.02	0.8652E-03	-0.29	0.41	-0.52	0.994	-0.574	0.819	0.000	0.980	1.00	1.75	1.00
699	709	710	779	778	0.02	0.8652E-03	-0.29	0.41	-0.55	0.994	-0.574	0.819	0.000	0.980	1.00	1.75	1.00
700	710	711	780	779	0.02	0.8652E-03	-0.29	0.41	-0.58	0.994	-0.574	0.819	0.000	0.980	1.00	1.75	1.00

DUE TO	(RADIANS/SEC)	-180.0	-135.0	-90.0	-45.0	0.0	45.0	90.0	135.0	180.0
DRIFT										
ROLL(RX)										
	0.524	-1.08E-03	-2.16E-03	-2.33E-03	-9.10E-04	-1.28E-03	-2.19E-03	-2.32E-03	-1.01E-03	-1.14E-03
	0.546	-1.48E-03	-1.69E-03	-1.65E-03	-2.08E-03	-1.44E-03	-1.95E-03	-1.76E-03	-2.44E-03	-1.27E-03
	0.571	-1.11E-03	-1.05E-03	-2.65E-03	-2.00E-03	-1.03E-03	-1.05E-03	-2.67E-03	-2.15E-03	-1.17E-03
	0.598	-1.93E-03	-1.72E-03	-2.72E-03	-1.46E-03	-1.72E-03	-1.68E-03	-2.69E-03	-1.60E-03	-1.81E-03
	0.628	-2.09E-03	-2.65E-03	-3.18E-03	-1.96E-03	-1.98E-03	-2.48E-03	-3.01E-03	-1.88E-03	-2.10E-03
	0.661	-2.61E-03	-2.07E-03	-2.96E-03	-1.74E-03	-2.68E-03	-2.01E-03	-3.12E-03	-1.69E-03	-2.63E-03
	0.698	-2.97E-03	-2.78E-03	-3.59E-03	-3.11E-03	-2.72E-03	-3.11E-03	-3.98E-03	-3.38E-03	-2.89E-03
	0.739	-3.85E-03	-4.28E-03	-4.47E-03	-3.86E-03	-3.63E-03	-4.60E-03	-4.52E-03	-4.25E-03	-3.93E-03
	0.785	-3.75E-03	-5.37E-03	-5.15E-03	-4.63E-03	-3.92E-03	-5.88E-03	-5.88E-03	-4.84E-03	-3.71E-03
	0.838	-5.68E-03	-5.47E-03	-6.84E-03	-5.67E-03	-5.56E-03	-6.05E-03	-7.70E-03	-6.25E-03	-5.75E-03
	0.898	-6.87E-03	-7.66E-03	-8.28E-03	-6.31E-03	-7.03E-03	-8.75E-03	-1.03E-02	-7.61E-03	-6.95E-03

DUE TO	(RADIANS/SEC)	-180.0	-135.0	-90.0	-45.0	0.0	45.0	90.0	135.0	180.0
DRIFT										
PITCH(RY)										
	0.524	1.87E-03	3.64E-04	1.67E-03	3.57E-03	2.16E-03	2.94E-05	1.53E-03	3.18E-03	1.99E-03
	0.546	2.37E-03	2.03E-03	1.37E-03	2.02E-03	2.18E-03	2.30E-03	1.38E-03	2.20E-03	2.19E-03
	0.571	-3.00E-04	2.06E-03	7.03E-04	2.50E-03	-1.55E-04	2.33E-03	6.27E-04	2.49E-03	-2.50E-04
	0.598	2.65E-03	7.37E-04	2.56E-03	2.85E-03	2.94E-03	5.87E-04	2.72E-03	2.97E-03	2.67E-03
	0.628	2.18E-03	-8.67E-04	4.54E-03	2.26E-03	2.17E-03	-9.06E-04	4.67E-03	1.95E-03	2.10E-03
	0.661	1.94E-03	-2.25E-04	1.05E-03	4.00E-03	1.71E-03	2.76E-04	1.52E-03	4.31E-03	1.92E-03
	0.698	2.94E-03	1.43E-03	2.64E-03	9.41E-04	3.19E-03	1.64E-03	2.53E-03	1.12E-03	2.76E-03
	0.739	3.50E-03	4.58E-03	3.50E-03	2.62E-03	4.05E-03	5.26E-03	3.43E-03	2.21E-03	3.60E-03
	0.785	2.02E-03	4.28E-03	2.69E-03	2.71E-03	2.74E-03	4.55E-03	2.75E-03	1.88E-03	2.11E-03
	0.838	2.53E-03	1.56E-03	3.06E-03	3.56E-03	3.61E-03	2.40E-03	2.78E-03	3.60E-03	2.40E-03
	0.898	6.64E-03	6.14E-03	3.43E-03	4.01E-03	8.45E-03	7.86E-03	2.64E-03	3.79E-03	6.60E-03

DUE TO	(RADIANS/SEC)	-180.0	-135.0	-90.0	-45.0	0.0	45.0	90.0	135.0	180.0
DRIFT										
YAW(RZ)										
	0.524	-4.57E-02	-4.57E-02	-4.57E-02	-4.57E-02	-4.57E-02	-4.57E-02	-4.57E-02	-4.57E-02	-4.57E-02
	0.546	-4.64E-02	-4.64E-02	-4.64E-02	-4.64E-02	-4.64E-02	-4.64E-02	-4.64E-02	-4.64E-02	-4.64E-02
	0.571	-4.72E-02	-4.72E-02	-4.72E-02	-4.72E-02	-4.72E-02	-4.72E-02	-4.72E-02	-4.72E-02	-4.72E-02
	0.598	-4.80E-02	-4.80E-02	-4.80E-02	-4.80E-02	-4.80E-02	-4.80E-02	-4.80E-02	-4.80E-02	-4.80E-02
	0.628	-4.90E-02	-4.90E-02	-4.90E-02	-4.90E-02	-4.90E-02	-4.90E-02	-4.90E-02	-4.90E-02	-4.90E-02
	0.661	-5.01E-02	-5.01E-02	-5.01E-02	-5.01E-02	-5.01E-02	-5.01E-02	-5.01E-02	-5.01E-02	-5.01E-02
	0.698	-5.14E-02	-5.14E-02	-5.14E-02	-5.14E-02	-5.14E-02	-5.14E-02	-5.14E-02	-5.14E-02	-5.14E-02
	0.739	-5.29E-02	-5.29E-02	-5.30E-02	-5.29E-02	-5.29E-02	-5.29E-02	-5.30E-02	-5.29E-02	-5.29E-02
	0.785	-5.47E-02	-5.47E-02	-5.47E-02	-5.47E-02	-5.47E-02	-5.47E-02	-5.47E-02	-5.47E-02	-5.47E-02
	0.838	-5.68E-02	-5.68E-02	-5.68E-02	-5.68E-02	-5.68E-02	-5.68E-02	-5.68E-02	-5.68E-02	-5.68E-02
	0.898	-5.92E-02	-5.93E-02	-5.93E-02	-5.93E-02	-5.92E-02	-5.93E-02	-5.93E-02	-5.93E-02	-5.92E-02

APPENDIX B

Catenary mooring line shapes

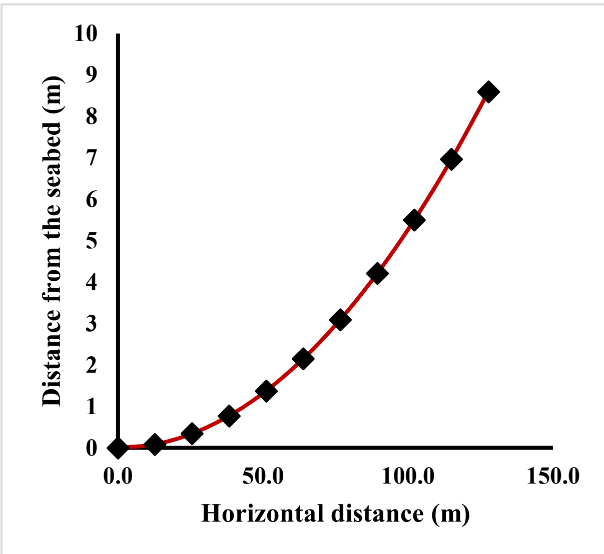

Geometry 02

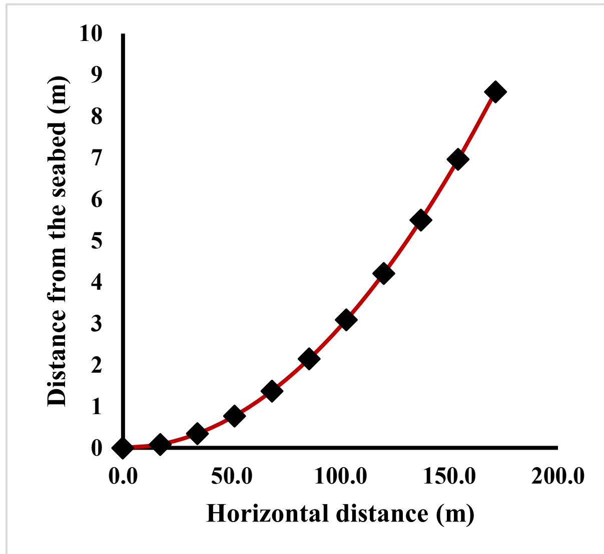

Geometry 03

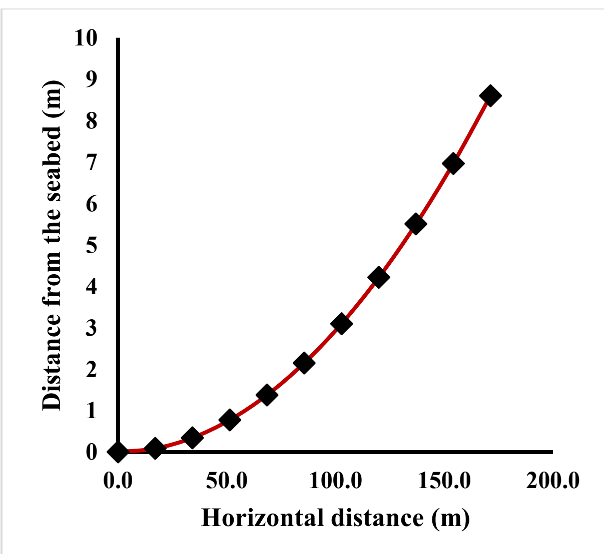

Geometry 04

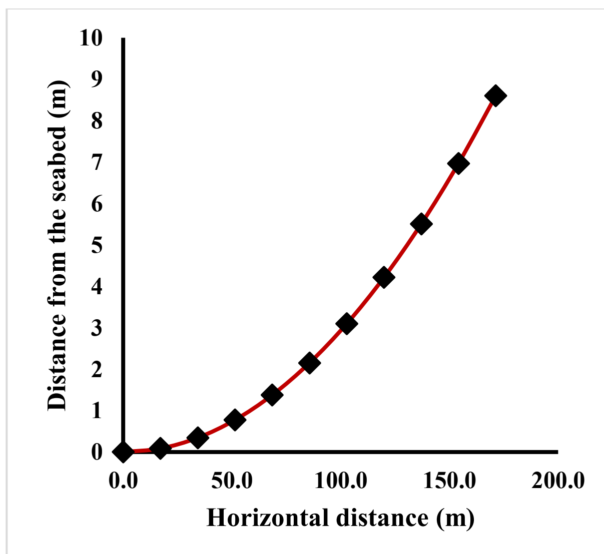

Geometry 05

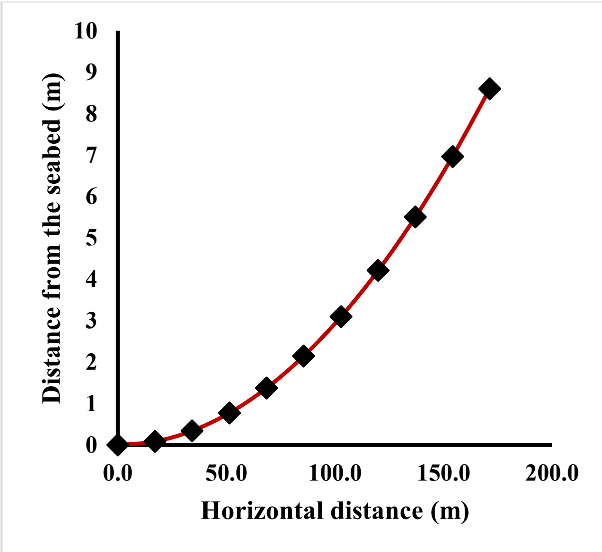

Geometry 06

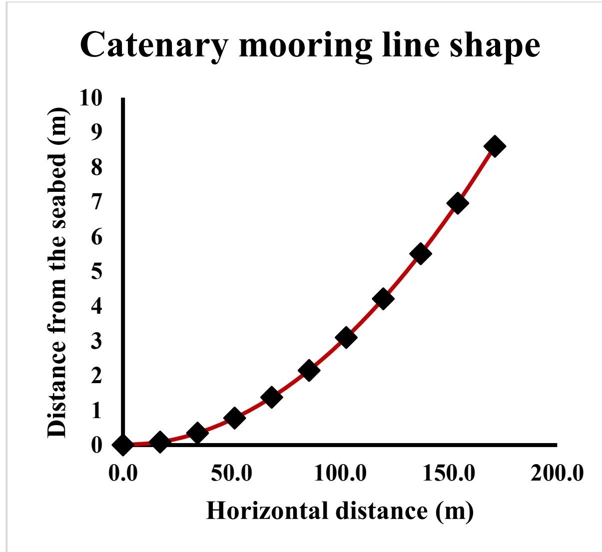

Geometry 07

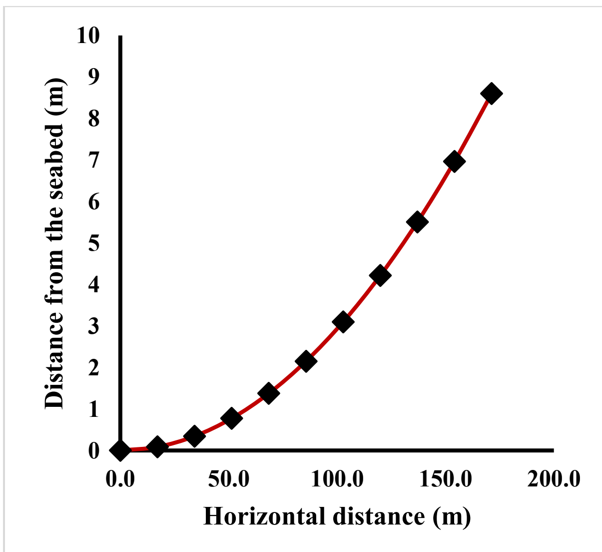

Geometry 08

APPENDIX C

Sample curves of normalized value of radiation damping coefficient, added mass coefficient, impulse response function of excitation and radiation forces –

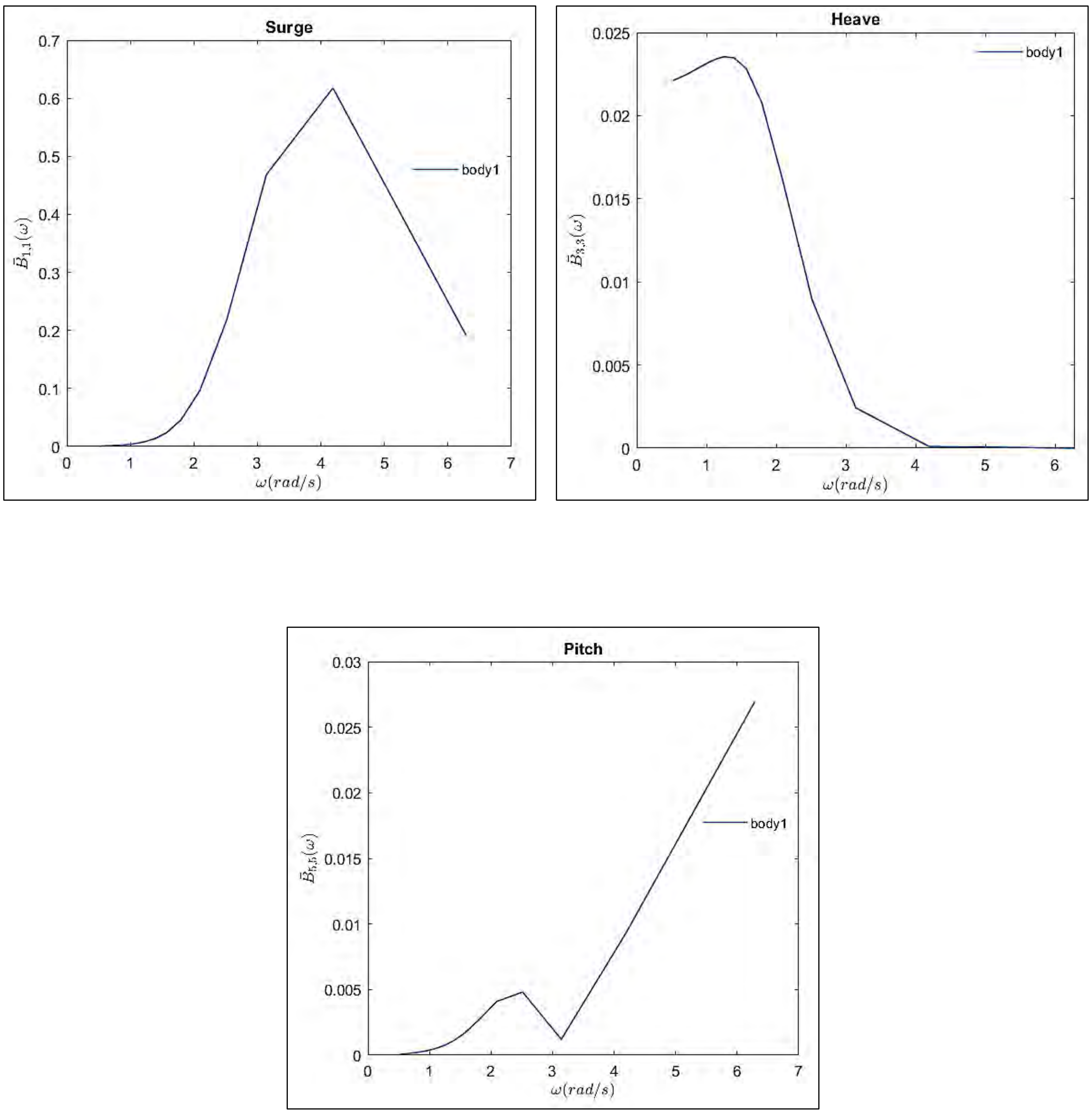

Figure C1 Normalized radiation damping

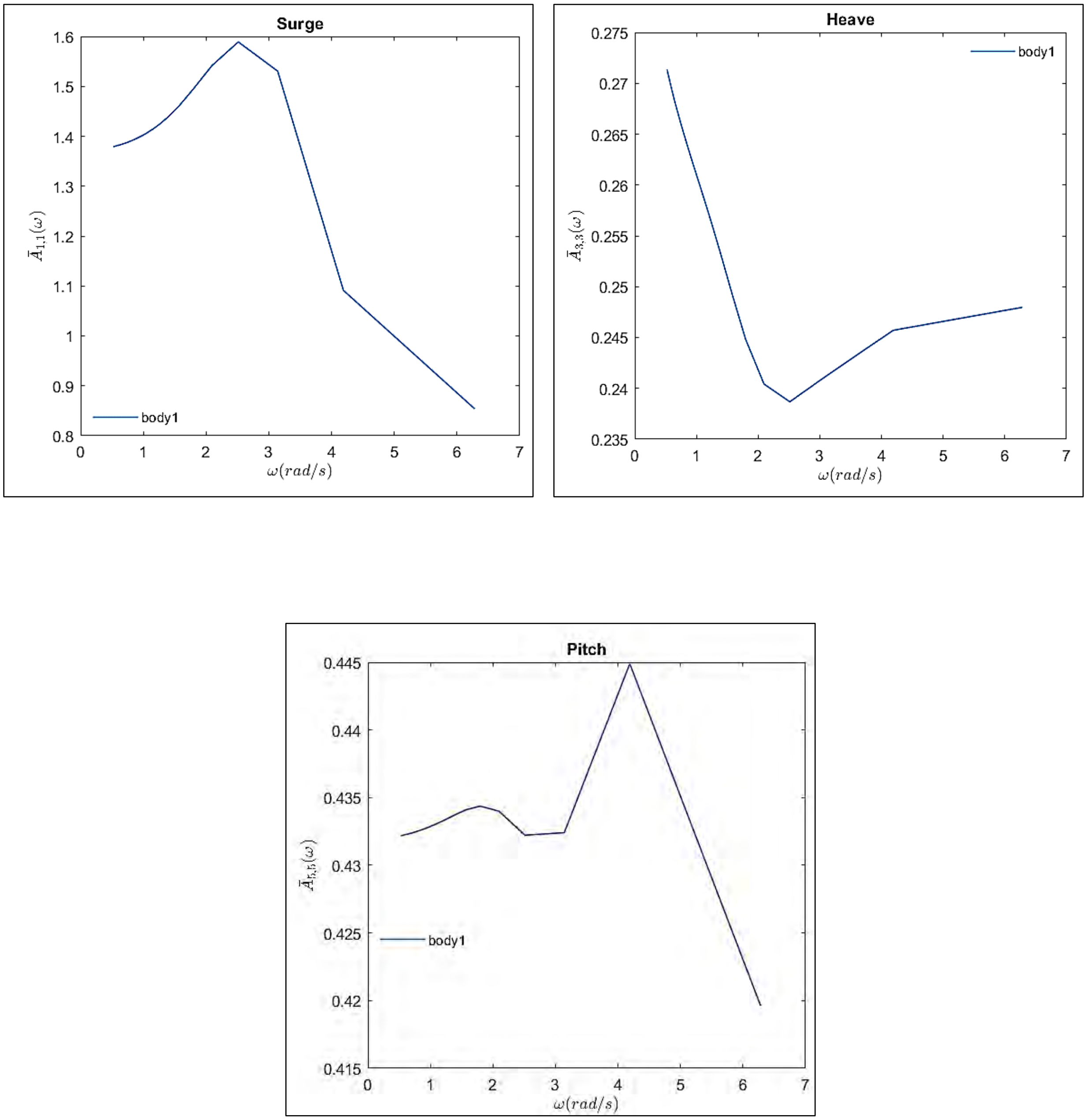

Figure C2 Normalized added mass

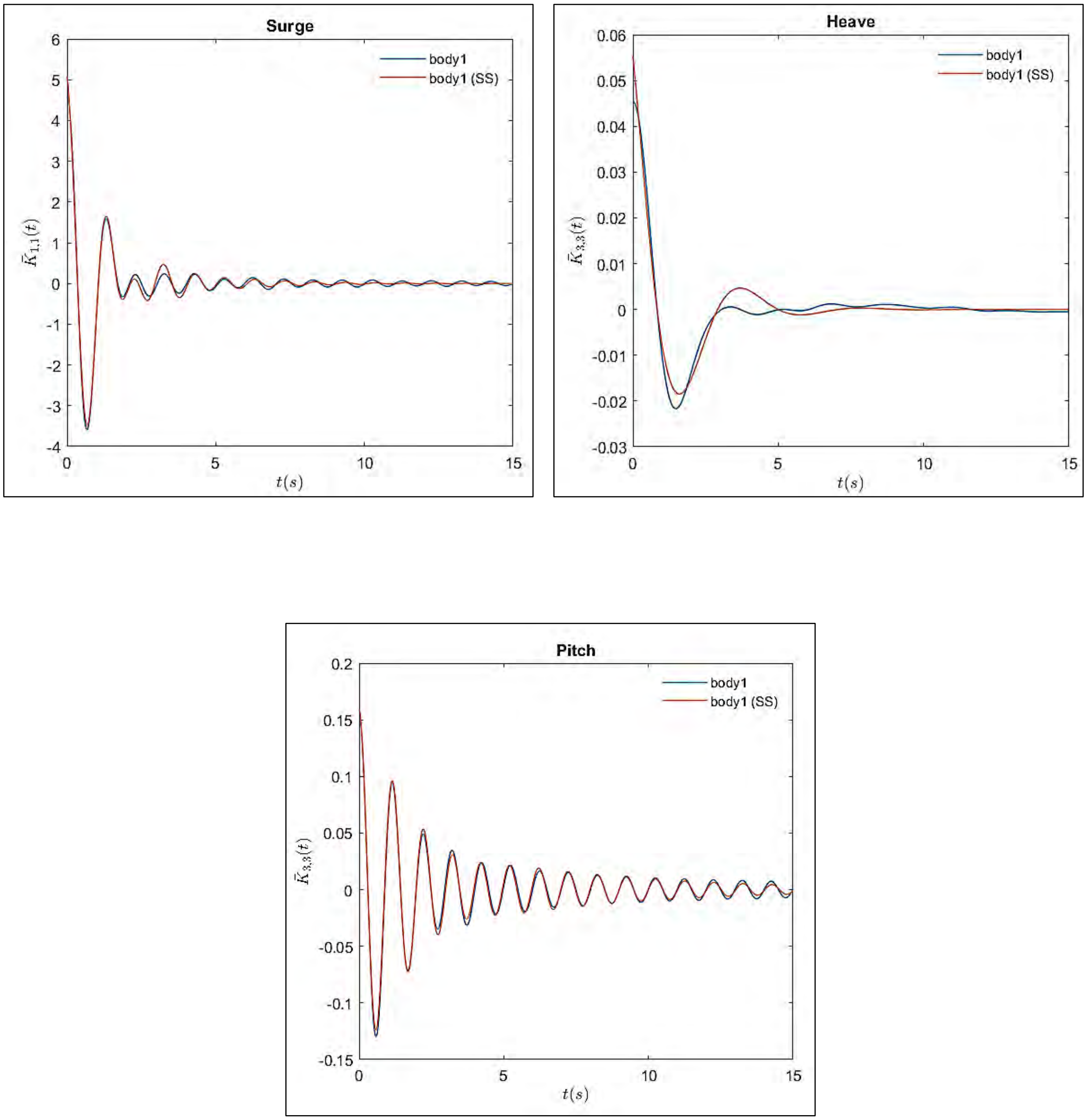

Figure C3 Normalized radiation impulse response function

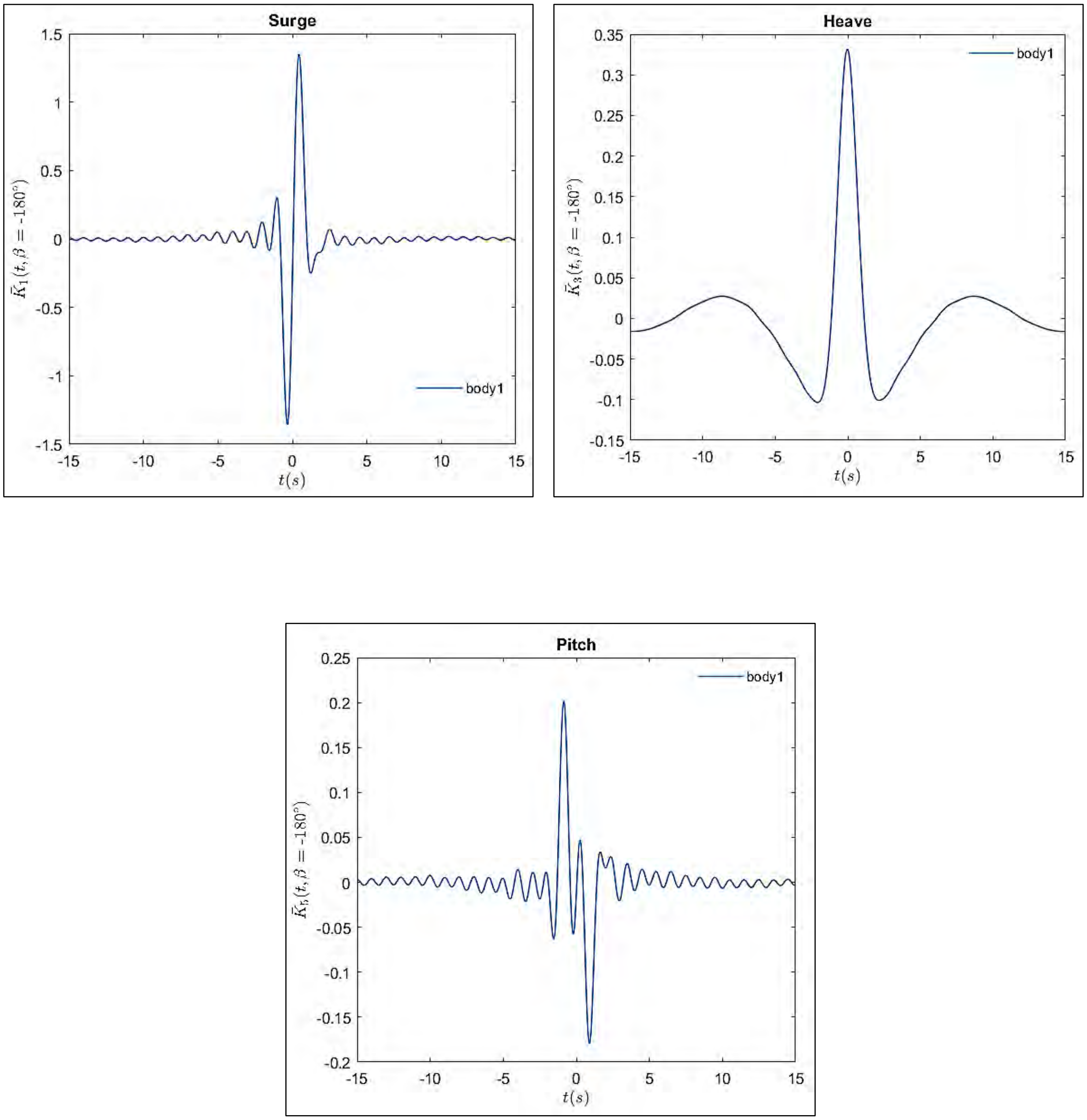

Figure C5 Normalized excitation impulse response function

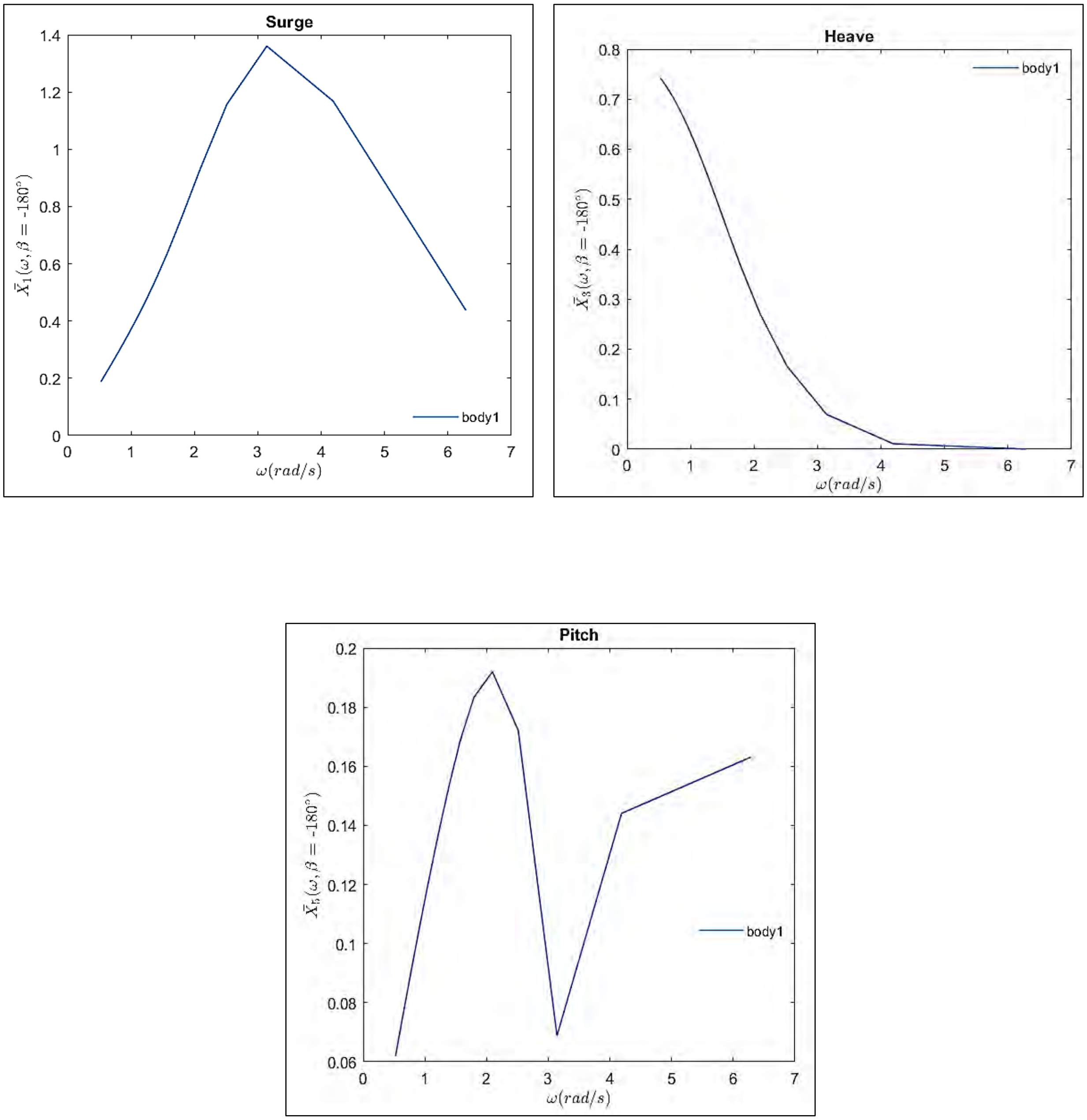

Figure C4 Normalized excitation force magnitude